

INSTITUTE FOR ASTRONOMY, ETH ZURICH

MASTER THESIS

**VLT/NACO Direct Detection and
Characterization of Six Companion Candidates
in the Circumstellar Disks of Young Stars**

Gabriele Cugno

Supervisors:

Prof. Dr. Hans Martin Schmid
Dr. Sascha P. Quanz

May 10, 2017

Abstract

I present high contrast imaging VLT/NACO data of six Herbig Ae/Be stars and one T Tauri star in the L' band ($\lambda \sim 3.8\mu m$) from the NACO-ISPY survey. Among the seven datasets, six companion candidates have been found. They have been detected at a projected angular separation in the range $0.143'' - 0.563''$ and have apparent magnitudes between 9.2 mag and 14.4 mag. Large uncertainties in the star distance and orbit orientation make difficult to properly characterize the COND masses and the physical de-projected distances of the candidates, which lay in the range $7.8 - 820 M_J$ and $23.6 - 257$ AU respectively.

For one of them, proper motion study with a second observation could be performed, and the stellar companion scenario seems to best match with the available astrometric and photometric data. For all the objects, follow-up observations are suggested and encouraged.

I discuss the importance of sampling the population of gas giant planets to infer empirical constraints to the formation models. Furthermore, I argue that most of the light might be due to an accreting circumplanetary disk, implying lower planetary masses. If confirmed to be orbiting planets, the presented sources could double the number of candidate forming planets, leading in the next few years, thanks to multiwavelength observations, to new insights in the gas giant formation mechanism.

Contents

| | | |
|----------|---|-----------|
| 1 | Introduction | 1 |
| 1.1 | State of the field | 1 |
| 1.1.1 | Models for Planet Formation | 2 |
| 1.1.2 | Known Forming Planets and Circumplanetary Disks | 3 |
| 1.2 | Goal of the project | 4 |
| 2 | Data | 5 |
| 2.1 | Datasets | 5 |
| 2.2 | Data files | 5 |
| 2.3 | Individual objects | 6 |
| 2.3.1 | HD259431 | 6 |
| 2.3.2 | HD34282 | 6 |
| 2.3.3 | HD101412 | 7 |
| 2.3.4 | HD179218 | 9 |
| 2.3.5 | TW Hydrae | 9 |
| 2.3.6 | HD97048 | 10 |
| 2.3.7 | HD141569 | 10 |
| 3 | Methods | 12 |
| 3.1 | Pipeline and data reduction | 12 |
| 3.2 | Angular Differential Imaging and PynPoint | 13 |
| 3.3 | Detection | 14 |
| 3.4 | Signal characterization | 14 |
| 3.5 | Contrast curves | 16 |
| 3.6 | Optimization and choice of the analysis variables | 17 |
| 3.6.1 | Background subtraction mode, <i>stack</i> parameter and aperture size | 17 |
| 3.6.2 | Statistics on the images | 18 |
| 3.6.3 | Comparison of Characterization Methods | 20 |
| 4 | Results | 22 |
| 4.1 | HD259431 | 22 |
| 4.1.1 | Presence of a planet | 22 |
| 4.1.2 | Detection limits | 24 |
| 4.2 | HD34282 | 25 |
| 4.2.1 | Presence of a planet | 25 |
| 4.2.2 | Detection limits | 27 |
| 4.3 | HD101412 | 27 |
| 4.3.1 | Presence of a planet | 27 |
| 4.3.2 | Detection limits | 30 |
| 4.4 | HD179218 | 31 |
| 4.4.1 | Planet detection | 31 |
| 4.4.2 | Detection Limits | 34 |
| 4.5 | TW Hydrae | 34 |
| 4.5.1 | Detection limits | 34 |
| 4.6 | HD97048 | 36 |
| 4.6.1 | Detection Limits | 36 |
| 4.7 | HD141569 | 37 |
| 4.7.1 | Detection Limits | 37 |
| 5 | Discussion | 38 |
| 5.1 | Individual objects | 38 |
| 5.1.1 | HD259431 | 38 |
| 5.1.2 | HD34282 | 39 |
| 5.1.3 | HD101412 | 40 |
| 5.1.4 | HD179218 | 41 |
| 5.1.5 | TW Hydrae, HD97048 and HD141569 | 41 |
| 5.2 | Comparison between protoplanetary candidates | 42 |

| | | |
|----------|--|-----------|
| 5.3 | Mass estimation from evolutionary models | 43 |
| 6 | Conclusions | 45 |
| 7 | Acknowledgments | 45 |

1 Introduction

Exoplanets are planets orbiting a star beyond the solar system. Planets can be classified as close-in object (separation < 100 AU) with inferred masses of $\leq 13 M_J$, because for higher masses they are expected to start burning deuterium in the cores. The first detection of an exoplanet dates back to 1995, when Michel Mayor and Didier Queloz published the discovery of a gas giant planet around the star 51 Pegasi (Mayor and Queloz, 1995) detected with the Radial Velocity (RV) method. They measured the radial motion of the star and found out that it was oscillating back and forth with a period of 4 days. They explained this motion through the gravitational attraction induced from a Jupiter-mass planet. Today, according to the Exoplanet Orbit Database (EOD) we know more than 700 planets, which were first detected with the RV method.

Since then, many other detection methods were developed and improved, and many other planets were found. In particular, the majority of extrasolar planets was discovered with the transit method, in which the periodic dimming of the brightness of the star attributable to eclipses from orbiting planets is measured. The transit detection technique allowed the discovery of more than 2700 transiting planets (EOD) and more than 9000 Kepler’s Object of Interest (KOI), which are candidate planets detected by Kepler.

Another method for the search of exoplanets is astrometry, in which the motion of the star in the sky plane, due to gravitational attraction to the planet, is measured. Only one planet until now has been discovered using astrometry, but it is thought that this method has a great potential which can be exploited in the future, especially with the very precise GAIA data. There are also other methods, for example gravitational microlensing and timing variation, but only a few planets have been found using them and therefore they will not be explained in details.

All these methods are called ‘indirect’, since the planet is detected observing the characteristics of the star. Every method is appropriate for the discovery of different planets. For example, RV is particularly suitable for heavy close by planets with a small inclination angle, transit has an important bias towards edge-on systems, since the object must orbit in the observer’s line of sight, with planets at small radii, and astrometry prefers face-on systems with planets at large distances.

For a direct detection of a planetary mass companion, one had to wait until 2004, when Chauvin et al. (2004) reported the observation of a $\sim 5 M_J$ object orbiting a brown dwarf, not a star. Later, in 2008, Lafrenière et al. (2008) imaged a candidate planet near a young (~ 5 Myr) star of the Upper Scorpius association. The same year, Marois et al. (2008) took a first picture of three planets orbiting HR 8799. These discoveries got the new research field of direct imaging of exoplanets started.

This method has multiple advantages with respect to the indirect ones listed above. First of all, the images of exoplanets allow a photometric and spectroscopic study for the characterization of atmospheres, including their temperature, chemical composition and other parameters. Furthermore, after the analysis, one can give independent constraints to the orbital parameter and to the planet properties. Nevertheless, like the astrometry technique, direct imaging focuses on planets orbiting at large separations from their host stars, where transit and RV are weaker. It also has some disadvantages, in particular its increasing demand for instrumentation and analysis techniques to detect weaker planets nearer to their host stars. More specifically, an Adaptive Optics (AO) system is needed, with a coronagraph and a large mirror, to reach small angular separations. Furthermore, one needs analysis techniques as Angular Differential Imaging (ADI) and Differential Polarimetric Imaging (DPI) to subtract the Point Spread Function (PSF) of the star and to reach the requested contrast.

At the moment, only 8 objects with the characteristics to be classified as planets have been directly observed (Bowler, 2016). Since, in the past few years, a lot of resources and energies have been invested to develop instruments and techniques and to push them to their limits, in the near future the number of imaged planets is expected to considerably increase, and, with that, the knowledge about them.

1.1 State of the field

Due to their high resolution, the powerful direct imaging facilities (as NACO and SPHERE at VLT, GPI at Gemini South and NIRC2 at Keck) are not only used to detect and to observe planets, but also to spatially resolve the circumstellar disks and look for substructures in the disks emission, in order to constrain their properties, like density profile, temperature and composition.

In this project, I will use the NACO capability in detecting point sources to look for young planets still embedded in the disks of Herbig Ae/Be and T Tauri stars, which are particularly interesting objects

for the search of forming planets. Indeed, they are pre-main sequence intermediate-mass and low mass objects, respectively, still in the gravitational contraction phase. They are radiating an infrared excess due to the dust re-emission from the circumstellar disk, which is thought to be a favourable environment for the formation of planets due to the large amount of gas and dust available.

Briceño et al. (2001) studied the lifetime of circumstellar disks in the Orion OB1 association and calculated their lifetime to be a few million years. A similar research conducted by Bally et al. (1998) concluded that most disks have much shorter lifetimes, of order 10^5 yr or even less, possibly 10^4 yr. Consequently the detection of companions in the disk puts an upper limit to its age, since it could only be younger than the central star and its disk.

There is a further advantage in looking for young objects, since they are still contracting. The shrinkage releases a lot of energy making them appear more luminous at infrared wavelengths. Consequently, the contrast with the host star is much higher and they can be observed more easily. During their evolution, they keep releasing energy over time, cooling down. The cooling is initially rapid, then it slows down with the decreasing effective temperature. For these reasons, looking for the thermal emission from young gaseous giant planets in the near- and mid-infrared ($1\text{--}5\ \mu\text{m}$) increases the chance of a detection and should be preferred to the observation of old systems at optical/UV, where the contrast is much lower.

1.1.1 Models for Planet Formation

There are two major theories about the planet formation process: core accretion theory and gravitational instability theory.

Core accretion theory states that the formation of giant planet cores occur via a complicated process which includes different phases. In the dust settling phase, mm-cm sized dust particles move towards the mid-plane of the disk, while μm sized particles can not settle during the disk lifetime, and m-sized rocks do not couple to disk gas, and continue to oscillate around the mid-plane. If the particle density is high enough, grains may stick together by coagulation to form larger bodies, as rocks. This process is even faster if the bodies are immersed in a flow of material full of icy particles, which may condensate, building up ice balls. Finally, through collisional growth, bodies can reach planetesimal dimensions (1-1000 km) and then form terrestrial planets through gravitational focussing, in which the terrestrial core attracts via gravitational forces a lot of gas holding a bound atmosphere, mainly hydrogen and helium (Pollack et al., 1996). Simulations have shown that at large separations, several tens to hundreds of AU, the time needed for a planet to form exceeds the lifetime of the disk. Therefore, either a further theory to explain planet formation in the outer parts of the circumstellar disks, or a process able to make the planet migrate outwards, is required.

Gravitational instability theory assumes that the planet formation process is very similar to the one of stars: a region of circumstellar disk, having higher density because of inhomogeneities and irregularities in the matter distribution, produces a stronger gravitational force with respect to other surrounding regions. The material starts to be attracted, the region to get denser, the exerted gravitational force to increase and even more material to be attracted. A counteracting process, the dissipation of denser regions, also takes place. The birth of a planet therefore requires the gravitational force to be stronger than the pulling out force, or the collapse time to be shorter than the time needed for a particle to escape the instability. Current models indicate that the formation process should happen in a massive disk at large separations (> 30 AU), where the material is cold enough to collapse, while warmer matter and gas nearer to the star are too energetic to shrink into a collapsed object. This model could explain the formation of Jupiter in thousand years or less (Boss, 1997).

These theories present two major differences: the time needed for the formation of the object and the bulk metallicity. The timescale needed to explain core accretion might be of several to tens millions of years, as suggested by Pollack et al. (1996), as the process strongly depends on the surface density of the protoplanetary disk, which determines the availability of accreting material. On the contrary, gravitational instability occurs much faster and is able to produce a planet similar to Jupiter in thousand years or less (Boss, 1997). Bulk metallicity is also different depending on the theory used, being higher in core accretion, and implying smaller planet radii and higher atmospheric opacities, resulting in a slower cooling of the object (Burrows et al., 2007).

A third important parameter, which differs between the two models, is the heat of formation retained by the fully formed object. Objects that underwent gravitational instability are believed to have higher entropies, higher effective temperatures and larger radii with respect to object formed by core accretion.

Marley et al. (2007) stated that planets created through the core accretion mechanism lose their internal entropy through accretion shocks. As a consequence, the giant planets are cooler and fainter, up to 100 times less luminous for a $10 M_J$ planet, evolving slower. For this reason the authors identified “hot start objects” to be the result of gravitational instability, since most entropy is retained by the object during formation, and “cold start objects” to be the outcome of the core accretion process, since a lot of heat gets lost during accretion shocks. Furthermore, they showed that more massive planets have “longer memory” of their initial thermal state, while low mass planets forget their initial condition sooner and faster.

Spiegel and Burrows (2012) constructed models to predict the evolution of cold and hot start objects and investigated the possibility that the distributions of properties of the two mechanisms overlap. During their work, they took the entropy as a free parameter, since it could not be constrained so far. They confirmed that objects starting with higher entropy and larger radius (hot start) can be up to 9 magnitudes brighter, depending on mass and spectral band (see Fig. 7 in the paper). The figure also shows how the memory of the initial condition changes as the mass varies. For instance, the emission from 1-2 M_J objects can be distinguished between cold and hot start only in the first 10-30 Myr after formation, while more massive planets (5-10 M_J), starting with two initially different entropy states, maintain their differences for much longer periods (up to 100 Myr in the K band). The models also give predictions for the time evolution of entropy, radius and effective temperature for different planet masses for both cold and hot start objects. An asymptotic convergence of the parameters calculated for the hot and the cold start models is observed for all the planetary masses. As for the brightnesses, the curves representing the parameters of low mass objects (1-2 M_J) converge much earlier, making very difficult to distinguish the initial conditions of the formation process already at an age of 10-30 Myr. For this reason it is crucial to collect empirical data and to observe planets at the very early stages of their lives, in order to be able to constrain the different models and characterize the initial conditions of the many gas giant planets we are observing at later stages.

1.1.2 Known Forming Planets and Circumplanetary Disks

Currently, there are three young forming protoplanet candidates: LkCa15b, HD100546b and HD169142b. LkCa15b was found by Kraus and Ireland (2012) using non redundant aperture masking interferometry, giving the community the first candidate forming protoplanet embedded in the disk. The recovered source is ~ 20 AU from the center and its position corresponds precisely to the center of the disk density gap previously observed (Epaillat et al., 2007). Subsequently, the detection was confirmed by Sallum et al. (2015), who also claimed the detection of a second and maybe a third companion.

Quanz et al. (2013) and Quanz et al. (2015) detected a companion of the Herbig Ae/Be star HD100546 using the *PynPoint* routine on VLT/NACO data. They analyzed the presence of a companion in two different epochs and confirmed the common proper motion. The companion lays at a distance of $\sim 0.42''$ and has a position angle of $\sim 9^\circ$, with a magnitude in the L' band of 13.9 mag and in the M' band of 13.3 mag. The object could not be detected in the K_s band.

Lastly, Reggiani et al. (2014) and Biller et al. (2014) discovered a companion of another Herbig Ae/Be star, HD169142, in the L' band. The planet candidate was located at ~ 21 AU from the central star, at the same distance of the cavity of the transition disk. The apparent magnitude was calculated to be $m_{L'} = 12.2 \pm 0.5$ mag and the COND model assigns to it a mass of 28-32 M_J . The source could not be detected in the J band.

Quanz et al. (2015) confronted the temperature and emitting area derived from the SED modeling with those predicted by the “hot start” model for the empirically measured L' and M' magnitudes. The brightness data were better explained with a 1 Myr old $\sim 10 M_J$ planet, whose emission has been extinction corrected. In that case, the confidence level reached values of $\sim 10\%$ or even less, concluding that there are inconsistencies between the evolutionary atmospheric models and the data. The same discrepancies were retrieved when, starting from the temperature and the emitting area values, they tried to derive the expected brightnesses at $3.8\mu m$ and $4.8\mu m$, according to the model, and compared them with the data. The main differences were that the planet was expected to be detected in the K_s band within a 3σ level and that the L' magnitudes were expected to have lower values than the M' ones. Not only these two expectations were not observed in the data, but also the color of the protoplanet, being redder than expected, was difficult to explain with a gravitationally collapsing object. They also briefly discussed the predictions from “cold start” models, when the initial entropy has low values, indicating that models matched with the data only in a very short time window of ≤ 0.1 Myr and

that it was unlikely that the observation was carried out exactly during that period. Furthermore, the radius estimation is much larger than the one expected from the core accretion models. Similar problems were presented by Reggiani et al. (2014), since the detected signal in the L' band was expected, according to the COND models and the sensitivity in that position, to be observed also in the J band. This was not the case. The brightness in the L' band suggested a 28-32 M_J object, but formation theories were not able to explain this order of masses at that distance from the star. Furthermore, classical gap opening theories predict that such an object should open a gap of $\Delta = 54 - 59$ AU, but the observed cavity in HD169142 disk had a width of ~ 10 AU. It seems therefore that the mass has been overestimated.

Analogous interrogatives may arise when looking at the results from Kraus and Ireland (2012), since the very bright object ($L \sim 2 \times 10^{-3} L_\odot$) and the associated extended emitting area were very difficult to be explained with either a pure gravitational collapse or a core accretion mechanism. The first because the relatively short process was expected to happen when the disk was still massive and material-rich, i.e. when the star was very young. The second because the available time, given by LkCa15 age, has not been sufficient to form a planet that massive.

To explain the differences between model predictions and data, a circumplanetary disk (CPD) was introduced, able to explain many features of the object (Zhu, 2015). The red color, as an example, could be explained by the fact that the CPD consists in a multitude of black bodies at different temperatures instead of a single one, making the SED less steep and motivating the observed color. Modeling the SED at mid- and far-IR bands makes possible to exclude brown dwarfs and simplifies the selection of CPDs (Zhu, 2015).

Because of its predicted extent, the CPD is expected to be unresolved and to appear as a point source (Quanz et al., 2015). The presence of the CPD adds a component to the SED, making different combinations of temperature and emitting surface plausible to explain the data points, in particular the derived emitting area. To constrain the model parameters, several other observations in different bands are required, in order to fit a well defined SED shape and to break degeneracies.

A CPD could also explain the large bolometric luminosities estimated by Quanz et al. (2015) and by Kraus and Ireland (2012). Indeed, accreting flows are able to produce huge amounts of luminosity, as observed in their values. For example, circumplanetary disks around a M_p object with radius R_p and accretion rate \dot{M} are able to emit

$$L_{disk} = \frac{GM_p \dot{M}}{2R_p}. \quad (1)$$

In the case when $M_p = M_J$, $R_p = R_J$ and $\dot{M} = 10^{-8} M_\odot \text{yr}^{-1}$, the accretion luminosity of the disk is $1.5 \times 10^{-3} L_\odot$, which is an amount of light comparable to the emission of a late-M-type/early-L-type brown dwarf (Zhu, 2015).

It is fundamental to bring empirical evidences into the discussion of the formation mechanism of gas giants to help constraining the condition in which Jupiter-like planets may form. This means that more precise information about protoplanetary disk compositions and kinematics, more powerful simulations and a larger sample of young planets at their formation, are required.

1.2 Goal of the project

Goal of this Master Thesis was to reduce VLT/NACO data of seven objects from the ISPY survey and to analyze them. The cosmetic reduction was based on the existing *PynPoint* Python package. Once the data have been calibrated and the background subtracted, I performed a Principal Component Analysis (Shlens, 2014) to reproduce and then to subtract the PSF in the innermost region near to the star (see Section 3.2). If a planet is visible, I characterized it using the *AstroPhoto* routine, which uses the false probability fraction to infer signal properties, and the *HesseMatrix* routine, which optimizes the parameters to reduce the surface curvature (see Section 3.4). The candidate position and its magnitude were directly estimated from the images. Using different studies and models like the COND ones (Baraffe et al., 2003) I then estimated other properties like mass, period and separation, and I described the sources as precisely as possible.

If no planet was visible in the image, the contrast curve of the object were calculated, indicating how bright a hypothetical companion should be not to be detected.

2 Data

In this section, I will describe the data used for the analysis in this work. In Section 2.1 I will present the stellar sample; in Section 2.2 I will explain what the data consist of and some specificities of each type of file; finally, in Section 2.3 I will list the objects I analyzed, giving some properties of the stars themselves and of their circumstellar disks.

2.1 Datasets

In this work, datasets for six Herbig Ae/Be stars and one TTauri star (TW Hya) from the Class II sub-project of the NACO-ISPY Survey have been analyzed (PI: Henning T. K., Segransan D., Quirrenbach A.). The lower part of Tab. 1 lists all the objects considered during the thesis, with some of their physical properties used during the search of companions and the determination of the detection limits.

These objects have been chosen because of their scientific interest: they are either very close to Earth and therefore allow the investigation at the same Inner Working Angles (IWAs) of smaller spatial separations to the star; or some features and substructures in their disks have been observed by previous works in the far IR or sub mm. Examples of these substructures include gaps in the density distribution and in the brightness profile. These could be the signature of ongoing or past planet formation processes, in which the material previously in the disk accretes onto planetesimal, leaving a dust and gas poor region in the disk, which is then observable (e.g. Fouchet et al., 2010).

The values of the L' magnitude reported in Tab. 1 are the linearly interpolated values at $3.8 \mu m$ using the measurements at $3.4 \mu m$ and $4.6 \mu m$. These information can be found in the AllWISE Catalogue (Wright et al., 2010). The same method has been used to calculate the errorbars of the brightness in the L' band.

Because of the uncertainty of the object distance from the Solar System, which still today is not well defined, for each object different values have been considered during the analysis. In particular, the data calculated by the Hipparcos mission (van Leeuwen, 2007) and by the more recent GAIA mission (Lindegren et al., 2016; Arenou et al., 2017) were examined. For some objects (for example HD259431, Section 4.1) that presented a large difference between the two measurements, and whose distribution functions did not overlap, both the cases were considered, keeping in mind that the right value most likely lies in between. Both the distance values and their errors were derived from the parallax measurements using the simple formula

$$D[pc] = \frac{1}{p}, \quad \delta D[pc] = \frac{1}{p^2} \delta p, \quad (2)$$

where p is the parallax value and δp its uncertainty, both given in arcseconds.

The age of the object is the most sensitive parameter on which the companion mass depends. It is the stellar property with the most important uncertainty, since no method exists at the moment to experimentally infer it with high precision. Therefore, in this work, values found in the literature from different sources will be used. These are listed with a more detailed presentation of each object in the individual description below and are reported in Tab. 1.

2.2 Data files

The data consist in SKY frames, SCIENCE frames, DARK frames and photometry frames.

SCIENCE frames are coronagraphic images of the object. The Annular Groove Phase Mask (AGPM) coronagraph (Mawet et al., 2013) is placed exactly on the object, allowing longer exposure times (otherwise the central pixels would saturate) and suppressing the diffraction pattern of the star. Every frame is slightly rotated with respect to the previous one. This technique is called Angular Differential Imaging (ADI, Marois et al., 2006) and allows to subtract in a very efficient way the PSF residuals of the star (see Section 3.2). The images are gathered in datacubes of 101 frames each, whose last is the mean of the previous 100 and therefore is not considered during the analysis.

SKY frames are coronagraphic images where the object is not in the Field of View (FOV). They sample the background luminosity and they are also gathered in 101 images in the same way as the SCIENCE frames. Every 13 SCIENCE datacubes, 1 SKY datacube is interposed. This allows, during the data reduction, to subtract only the temporary nearest background frames, which makes the analysis more robust against weather variations during the observing run. Because the coronagraph is present in both

the SKY and SCIENCE frames at the same position, it is quite hard to distinguish them by eye and one has to check in the header at which category the datacube belongs to.

Photometry frames are non saturated coronagraphic images of the object, taken with exactly the same setup of the SCIENCE frames, except for the exposure time to avoid pixel saturation. The object is shifted with respect to the signal of the coronagraph, so that one can reproduce the PSF of the star on the telescope and perform any kind of photometric study. Usually, six photometry frames are imaged pro run, three before and three after the run, each time in three different positions and on three different detectors of the CCD.

DARK frames take into account the non-data element in each image, in particular the dark current, when an electron in the CCD is thermally excited without being hit from a photon. Darks are only a calibration of the CCD camera, and therefore it does not matter what kind of filter is built on the telescope. The most important parameter is the exposure time: it has to be equal to the exposure of the images one wants to calibrate. In this work for every object I have to deal with two different sets of DARK frames: the one for the SCIENCE and SKY frames and the one for the photometry frames.

2.3 Individual objects

2.3.1 HD259431

HD259431 is a Herbig Ae/Be star in the constellation of the Unicorn of spectral type B6 (Kraus et al., 2008a). According to the Hipparcos mission and the GAIA mission it is respectively 289.9 ± 118.5 pc and 610.5 ± 108.0 pc far away from the solar system, and has a L' magnitude of 4.0 ± 0.2 mag from the archival data of the WISE mission.

Bouret et al. (2003) tried to calculate the spectral age of HD259431 starting from FUSE (Far Ultraviolet Spectroscopic Explorer) spectra, which is, according to the evolutionary tracks of Palla and Stahler (1993), less than 1 Myr. Even stronger constraints were put by Alecian et al. (2013), who studied a large sample of 70 Herbig Ae/Be stars with circular spectropolarimetry and calculated the age of HD259431 to be $0.059^{+0.035}_{-0.041}$ Myr. In their research they also estimated the mass of the star ($7.1^{+0.8}_{-0.8} M_{\odot}$) and its bolometric luminosity ($\log(L/L_{\odot}) = 3.35^{+0.12}_{-0.14}$), assuming a distance of 660^{+100}_{-100} pc from Kharchenko et al. (2005) (the parameters may vary largely when using other distance estimations). Kraus et al. (2008b) used spectrointerferometry in the near-infrared (NIR) K-band and in the mid-infrared (MIR) N-band to constrain the inclination of HD259431 disk to $40\text{--}60^{\circ}$. Ilee et al. (2014) confirmed the estimation of the inclination angle fitting the CO line profile of the disk. Their final result was $i = 52^{+5}_{-3}^{\circ}$. The position angle of the disk was calculated to be 80° from Wheelwright et al. (2011), but large uncertainties have to be taken into account. These parameters are summarized in Tab. 1 for every object in the sample. Thomas et al. (2007) investigated the multiplicity of Herbig Ae/Be stars using the Altair-NIRI adaptive optics system on Gemini North. They found 44 possible binaries, one of which very close to HD259431. The candidate companion was detected at a separation of $\rho = 0.15''$ with a position angle of 55.6° . The K band contrast with respect to the central star was estimated to be 3.8 mag.

HD259431 was observed on the 12th December 2016 in P98 (PI: Henning T. K., Segransan D., Quirrenbach A.; Program ID:198.C-0612(C)). The other information regarding the observing run are listed in the observing log in Tab. 1. The seeing of that night shows low quality, with a mean value of $2.32''$, which means that the FWHM of the signal is spread out to $2.32''$ in the optical frequency range. When compared to other seeing values of different nights, as for example the one of HD179218 ($0.76''$), one gets an idea of the bad conditions. During the observation the total rotation of the CCD has been 38.2° . The investigation of the average values distribution of HD259431 images shows a clear peak around 150 counts and no frames with negative value. I therefore apply the normalization at the beginning of the PSF subtraction in order to have more uniform images. For more information on this step for this and for the other objects see Section 3.2 and Section 3.6.2.

2.3.2 HD34282

HD34282 is a Herbig Ae/Be star of spectral class in the range A0V-A3V (Mora et al., 2001). The GAIA parallax measurement locates it at a distance of 325.1 ± 30.9 pc, while the Hipparcos one at a distance of 163.9 ± 43.8 pc. The values obtained from the two missions differ by a factor 2 and will strongly influence

the properties of every companion candidate. The star has an apparent L' magnitude of 6.6 ± 0.1 mag. Merín et al. (2004) constructed SEDs of two Herbig Ae/Be stars, HD34282 and HD141569, from data which range from ultraviolet to millimetre wavelengths. They then used non-parametric models to infer some of the properties of the disks surrounding the stars. Their work concluded that HD34282 has a bolometric luminosity of $L_* = 13.64^{+1.78}_{-1.53} L_\odot$, a mass of $M_* 1.59^{+0.04}_{-0.05} M_\odot$ and an age of $\tau_* = 6.41^{+0.46}_{-0.41}$ Myr. From the data they estimated the object to be 348^{+22}_{-20} pc away from the Solar System, supporting the GAIA measurements. Errors would be bigger, if taken into account the uncertainties from the gravity calculation. In the same paper, they were also able to extrapolate disk properties from the models of D'Alessio et al. (2001), in which the disk is composed of two parts: the mid-plane disk, with grains reaching cm sizes and emitting at sub-mm and mm wavelengths, and the surface disk, populated by smaller $\sim \mu\text{m}$ sized grains responsible for the mid-IR radiation. More specifically, the recovered disk mass was $0.6\text{--}0.7 M_\odot$, its extension ranged from 0.31 AU up to 705 AU, it had an inclination of 56° and it was accreting at $\dot{M} \sim 8 \times 10^{-9} M_\odot \text{yr}^{-1}$. Finally, they also found HD34282 to be metal-deficient, with $[Fe/H] = -0.8$.

Piétu et al. (2003) identified a keplerian disk around HD34282 fitting CO J=2→1 lines at 1.3 mm. They modeled the data in order to extrapolate parameters to describe the disk, and found out that the disk has an inclination of $56^\circ \pm 3^\circ$ and a position angle of $25^\circ \pm 2^\circ$. The value of the inclination angle strongly agrees with the one obtained from Merín et al. (2004). They also gave an estimate of the distance of the star from the solar system, based on its position on the “distance-independent” evolution diagram (L/M^2 vs. spectral type), which was 400^{+170}_{-100} pc, once again supporting the GAIA measurement. From their model one can also estimate the mass of the disk, which is $0.11^{+0.09}_{-0.05} M_\odot$, much lower than the one estimated from the SED.

Khalafinejad et al. (2016) claimed the presence of a large dust gap in HD34282 disk at a distance of $r_{cav} = 92^{+31}_{-17}$ AU, using mid-IR Q-band images taken with Gemini North/MICHELLE. This value was obtained assuming a star distance of ~ 384 pc and makes the object of particular interest, since gaps are often associated with the presence of a planetary companion. However, Uyama et al. (2017) observed HD34282 in the H band using polarization differential imaging from the Subaru Telescope, without finding any companion.

HD34282 was observed on the 7th November 2016 in P98 (PI: Henning T. K., Segransan D., Quirrenbach A.; Program ID: 198.C-0612(A)). The information concerning the observation are reported in Tab. 1.

HD34282 datacube presented many images with a negative total amount of counts and, once again, the temporal distribution of the mean values indicated that the region of the SKY images, where neither AGPM nor star were present, was much brighter than the one in the SCIENCE images. Therefore the normalization step during the *PymPoint* processing has been removed.

2.3.3 HD101412

HD101412 is a Herbig Ae/Be star, classified as a B9.5V, located at a distance of 440.5 ± 56.3 pc according to the GAIA parallax. No measurements from the Hipparcos mission are available, but different studies located HD101412 at very different distances, ~ 160 pc according to Juhász et al. (2010) and ~ 118 pc according to Maaskant et al. (2015). In this work, I will consider the distances proposed by the GAIA mission and by Maaskant et al. (2015) since they are the extreme values of the distance range. The star has a magnitude in the L' band of 5.8 ± 0.1 mag.

HD101412 presents strong magnetic fields of the order of $2.5 - 3.5$ kG (Hubrig et al., 2010). The study on the magnetic properties of Herbig Ae/Be stars conducted by Folsom et al. (2012) derived many stellar properties for HD101412. Among them, the inferred stellar mass was $3.0 \pm 0.3 M_\odot$, the stellar luminosity yielded $\log(L/L_\odot) = 1.92 \pm 0.14$ and the estimated age was $1.2^{+0.8}_{-0.7}$ Myr. Seok and Li (2017) successively adopted these values for their study on Polycyclic Aromatic Hydrocarbons (PAH) in protoplanetary disk. Fairlamb et al. (2015) calculated various properties of 91 Herbig Ae/Be stars within a large spectroscopic study conducted with the VLT/X-shooter instrument. The main goal was to investigate the accretion rates of the stars, but different other stellar parameters were also calculated. In the specific case of HD101412, they found completely different values with respect to those given above: the star was 301^{+11}_{-10} pc away, it had a luminosity of $L_* = 1.36 \pm 0.23 L_\odot$ and its mass was of $M_* = 2.0 \pm 0.1 M_\odot$. Finally, its age was estimated to be 6.35 ± 1.84 Myr.

Table 1: The upper part of the table reports the observing log of all the objects analyzed in this work. The lower part lists coordinates, distance, apparent magnitude in the L' band and the estimated age of the stars, as well as the inclination and position angles of the disks. All the references are given in the individual section.

| Property | HD259431 | HD34282 | HD101412 | HD179218 | TW Hydrae | HD97048 | HD141569 |
|-------------------------------|------------|------------|------------|------------|------------|------------|------------|
| UT date [yyyy mm dd] | 2016 12 12 | 2016 11 07 | 2017 03 17 | 2016 05 02 | 2016 05 03 | 2016 05 02 | 2016 05 02 |
| UT start time [hh:mm:ss] | 06:23:17 | 04:56:37 | 03:02:18 | 07:03:59 | 23:51:06 | 23:31:51 | 04:22:25 |
| UT end time [hh:mm:ss] | 08:53:48 | 09:00:36 | 06:19:15 | 10:27:18 | 02:54:14 | 03:31:42 | 05:57:41 |
| Detector Integration Time [s] | 0.25 | 0.25 | 0.30 | 0.35 | 0.35 | 0.35 | 0.35 |
| Coads | 100 | 100 | 100 | 100 | 100 | 100 | 100 |
| Number of datacubes | 235 | 325 | 265 | 214 | 181 | 273 | 103 |
| Total integration time [s] | 5875 | 8125 | 7950 | 7490 | 6335 | 9555 | 3605 |
| Pixel scale (mas/pix) | 27.19 | 27.19 | 27.19 | 27.19 | 27.19 | 27.19 | 27.19 |
| Filter | L' | L' | L' | L' | L' | L' | L' |
| Coronagraph | AGPM | AGPM | AGPM | AGPM | AGPM | AGPM | AGPM |
| Parallactic angle start[°] | 166.9 | 237.0 | 324.0 | 217.3 | 301.7 | 333.6 | 222.4 |
| Parallactic angle end[°] | 128.7 | 119.4 | 37.4 | 153.8 | 76.6 | 41.1 | 173.0 |
| Mean seeing [as] | 2.32 | 0.66 | 0.72 | 0.76 | 0.83 | 0.61 | 0.63 |
| Mean airmass | 1.42 | 1.09 | 1.25 | 1.37 | 1.05 | 1.68 | 1.09 |

| | | | | | | | |
|----------------------------|-----------------|-------------------------|-----------------------------------|------------------------|------------------|--------------|--------------|
| RA [hh:mm:ss] | -34:42:14.5 | 05:16:00.4 | 11:39:43.7 | 19:11:11.2 | 11:01:51.3 | 11:08:03.3 | 15:49:57.3 |
| DEC [dd:mm:ss] | 10:19:13.5 | -09:48:35.4 | -60:10:21.7 | 15:47:15.6 | -34:42:14.5 | -77:39:17.4 | -03:55:21.6 |
| Dist GAIA [pc] | 610.5 ± 108 | 325.1 ± 30.9 | 440.5 ± 56.3 | 293.3 ± 30.1 | 59.5 ± 1.0 | 178.9 ± 8.3 | 116.0 ± 8.0 |
| Dist Hipparcos [pc] | 289.9 ± 118.5 | 163.9 ± 43.8 | — | 243.9 ± 77.4 | 56.5 ± 7.0 | 175.4 ± 23.4 | 111.2 ± 5.0 |
| L' magnitude [mag] | 4.0 ± 0.2 | 6.6 ± 0.1 | 5.8 ± 0.1 | 4.4 ± 0.2 | 6.9 ± 0.1 | 4.5 ± 0.1 | 6.1 ± 0.1 |
| Age [Myr] | <1 Myr | 6.41 $^{+0.46}_{-0.41}$ | 6.35 ± 1.84, 1.2 $^{+0.8}_{-0.7}$ | 1.08 $^{+0.48}_{-0.7}$ | 10 $^{+10}_{-7}$ | ~ 2.3 | 5 ± 3, ~ 7.5 |
| Disk inclination angle [°] | 52 $^{+5}_{-3}$ | 56 ± 3 | 30 ± 6, 80 ± 7 | 57 ± 2 | 7 ± 1 | 39.9 ± 1.8 | ~ 56 |
| Disk position angle [°] | ~ 80 | 25 ± 2 | 38 ± 5 | 23 ± 3 | ~ -45 | 2.8 ± 1.6 | -3.7 ± 0.6 |

In their paper, van der Plas et al. (2008) spectrally resolved the 630 nm [OI] emission line and fitted the profile in order to infer physical disk parameters. Their data were best explained by an inclination angle between 24° and 41° , and they used a value of 30° . For this work, I will adopt the value of $(30 \pm 6)^\circ$. They were not able to give any information about the position angle of the disk. Later, van der Plas et al. (2015) adopted values for the disk inclination of $(80 \pm 7)^\circ$ and for the disk position angle of $(38 \pm 5)^\circ$ in order to study the CO distribution within the circumstellar disk. Menu et al. (2015) judged the proposed disk orientation unlikely, since HD101412 is an unobscured star. One can conclude that, in addition to the large distance uncertainty, the inclination of the disk is also not well determined and one has to deal with different possible values.

HD101412 was observed on the 17th March 2017 in P98 (PI: Henning T. K., Segransan D., Quirrenbach A.; Program ID: 198.C-0612(B)). The total field rotation of the CCD has been 73.4° . The information on the star and on the observation are summarized in Tab. 1. The histogram of the mean values per image shows that the distribution peaks around 0 counts, with 41.0% of the frames having a negative sum of counts. As a consequence, the normalization step has been removed from the pipeline.

2.3.4 HD179218

HD179218 is a Herbig Ae/Be star with brightness in the L' band of 4.4 ± 0.2 . The GAIA parallax locates it at a distance of 293.3 ± 30.1 from the Solar System, while the Hipparcos measurement suggests that it is closer to Earth, at 243.9 ± 77.4 pc.

The age of HD179218 was constrained by van Boekel et al. (2005) from a comparison of its position in the HR diagram with evolutionary pre-main sequence tracks. Their work estimated the system to have $\log(\tau/\text{yr}) = 6.1 \pm 0.4$, where τ is the age of the star. Furthermore, they found HD179218 to have the second largest fraction of crystalline dust among the known Herbig Ae/Be stars.

Alecian et al. (2013) were able to infer different stellar properties from their circular spectropolarimetry data, as the luminosity, for which holds $\log(L/L_\odot) = 2.26^{+0.14}_{-0.12}$, the mass, which is $M_* = 3.66^{+0.44}_{-0.34} M_\odot$ and the age, estimated to be $1.08^{+0.48}_{-0.7}$ Myr, confirming the value previously found by van Boekel et al. (2005).

Dent et al. (2005) fitted the $J = 3 - 2$ CO lines of 59 Herbig Ae/Be stars looking at many disk parameters and trying to find correlations between them. They found HD179218 disk to have an inclination of $(40 \pm 10)^\circ$, a dust mass of $\sim 10^{-4} M_\odot$ and an outer radius of 120 ± 20 AU. For their calculations they assumed a distance of 243 pc.

Fedele et al. (2008) compared the gas distribution ([OI] 630 nm emission) with the dust distribution ($10\mu\text{m}$ emission) in three protoplanetary disks surrounding intermediate mass stars. They found that the data best fitted a two component disk inclined by $(57 \pm 2)^\circ$ with a position angle of $(23 \pm 3)^\circ$.

HD179218 was also part of the sample observed by Uyama et al. (2017) in the H band. They did not detect any companion in its neighborhood.

HD179218 was observed on the 2nd May 2016 in P97 (PI: Henning T. K., Segransan D., Quirrenbach A.; Program ID: 097.C-0206(A)). The total rotation of the field of view during the observation was 296.6° , as it can be calculated from Tab. 1. The distribution of the average value per image peaks around 60 counts, and no image has a negative sum of counts. Therefore the normalization was applied and all the images have been leveled out.

2.3.5 TW Hydrae

TW Hydrae is the closest TTauri star to the Solar System, with a mass of $0.8 M_\odot$ (Qi et al., 2013). It is the only TTauri star considered in this work. Its distance from the Sun is 59.5 ± 1.0 pc according to the GAIA mission and 56.5 ± 7.0 pc according to the Hipparcos archival data. It has a L' magnitude of 6.9 ± 0.1 mag. Its age has been calculated to be 10^{+10}_{-7} Myr by Barrado Y Navascués (2006), who used the location on the HR diagram and the equivalent width of the $H\alpha$ and the Li lines to estimate it, and to be 10 Myr by Weinberger et al. (2013).

TW Hya disk is one of the most studied circumstellar disks, because of its vicinity and of its inclination, which appears to be only $(7 \pm 1)^\circ$ (Qi et al., 2004). The same study suggested a disk position angle of $\sim -45^\circ$. Its mass has been calculated to be $< 0.05 M_\odot$ by Bergin et al. (2013); it is therefore massive enough to host a planet.

Andrews et al. (2016) observed the $870\mu\text{m}$ continuum emission from the disk with the Atacama Large Millimeter/submillimeter Array (ALMA), tracing millimeter-sized particles. Their results showed important substructures and ring-shaped gaps at 2.4, 22, 37 and 43 AU. Different explanations for these features have been proposed, as magnetic, chemical and dynamical processes. The last one implies the presence of interacting planetary mass companions, which could be able to cause the observed gaps. No non-symmetric structures have been reported.

TW Hya was observed on the 3rd May 2016 in P97 (PI: Henning T. K., Segransan D., Quirrenbach A.; Program ID: 097.C-0206(A)) for $\sim 1\text{h}45\text{min}$, achieving a total field rotation of 134.9° . The observation log can be found in Tab. 1. Because many images had negative sums of counts, the normalization step has been removed from the PSF subtraction.

2.3.6 HD97048

HD97048 is a Herbig Ae/Be star located at a distance of 178.9 ± 8.3 pc according to the GAIA archival data and 175.4 ± 23.4 according to the Hipparcos mission. Other studies located HD97048 at even lower distances (~ 150 pc, Alonso-Albi et al., 2009) or confirmed the parallax measurements (175_{-20}^{+26} pc, van Boekel et al., 2005). The WISE catalogue assigns to HD97048 a L' magnitude of 4.5 ± 0.1 . The mass of the central star has been calculated to be $2.5 \pm 0.2 M_\odot$ and its age is estimated to be ~ 2.3 Myr (Lagage et al., 2006).

Several disk substructures like cavities and rings have been resolved with ALMA data (van der Plas et al., 2017; Walsh et al., 2016) and in the near-IR (Maaskant et al., 2013; Ginski et al., 2016). In particular, DPI-SPHERE images of Ginski et al. (2016) show gaps in the dust distribution at $0.25''$, $0.7''$, $1.4''$ and $2.0''$ from the star. The result of the hydrodynamical simulations from Kanagawa et al. (2016) was used to constrain the masses of potential planets formed from the material lacking in the first two gaps. In order to obtain the gap at $0.25''$, a planet of mass $0.3\text{--}2.6 M_\oplus$ is required, while an object with $M_* = 0.1 - 0.7 M_J$ could explain the second gap.

Quanz et al. (2012) imaged the surface layer of the HD97048 circumstellar disk in polarized light in the H and K_s band. They found the disk to have an inclination of $\sim 40^\circ$ ($(34 \pm 5)^\circ$ and $(47 \pm 2)^\circ$ for disk regions with different surface brightnesses, $13\text{--}14$ mag/arcsec² and $14\text{--}15$ mag/arcsec² respectively) and position angle $\sim 80^\circ$ (east to north). Furthermore, according to their observations, the disk becomes bluer at larger separations. The data of many works confirmed the orientation of the disk, described by the inclination angle ($39.9 \pm 1.8)^\circ$ and the position angle ($2.8 \pm 1.6)^\circ$ (Ginski et al., 2016; Lagage et al., 2006; Walsh et al., 2016). The disk extends up to a radius > 600 AU (Doering et al., 2007; Walsh et al., 2016).

HD97048 was observed on the 2nd May 2016 within the NACO-ISPY survey in P97 (PI: Henning T. K., Segransan D., Quirrenbach A.; Program ID: 097.C-0206(A)). Table 1 contains every information about the observation and the analyzed data. For its analysis, the division of every pixel value by the sum of the counts has been maintained, since the distribution of the mean value of the frames peaks around 45 counts and no frame has a negative total amount of counts. During the cosmetic reduction, the first SCIENCE datacube has been discarded, because it could not be read from the pipeline.

2.3.7 HD141569

HD141569 is a B9.5Ve pre-main sequence star located at 116.0 ± 8.0 pc from the Sun according to the Hipparcos measurements and at 111.2 ± 5.1 pc according to the more recent GAIA data. Because the distances from the two missions are very similar, I will use the GAIA data for the further calculations. The WISE catalogue assigns to the star a magnitude of 6.1 ± 0.1 mag at $3.8\mu\text{m}$.

HD141569 was found to be in a triple system with two low mass stellar companions orbiting at $\sim 7.6''$ and $\sim 9''$ (Weinberger et al., 2000). The star has a mass of $1.9 \pm 0.4 M_\odot$, it is accreting at a rate between $\sim 10^{-7}$ and $\sim 10^{-8} M_\odot\text{yr}^{-1}$ (Mendigutía et al., 2017), and for its luminosity holds $\log(L/L_\odot) = 1.49 \pm 0.06$ (Alecian et al., 2013). The estimate of its age by Weinberger et al. (2000) was 5 ± 3 Myr; Alecian et al. (2013) confirmed the star to be $5.7_{-1.4}^{+1.3}$ Myr old, but, however, the most recent investigation of Currie et al. (2016) about the star location on the HR diagram suggested HD141569 to be 7.5 Myr old.

Many authors investigated the orientation of its disk, its composition and its structure. There is a

general agreement about the orientation with a position angle of $(356.3^\circ \pm 0.6)^\circ$ and an inclination of 56° (Mazoyer et al., 2016). It was also found that HD141569A is surrounded by a circumstellar disk, which is transiting from protoplanetary to debris disk phase. Currie et al. (2016) and Mawet et al. (2017) identified structures and rings of dust around HD141569: using L' data from Keck/NIRC2 they investigated the dust population in the disk. More specifically they identified three concentric rings of material at 100 AU, 245 AU and 406 AU. Furthermore, Mawet et al. (2017) identified a possible very faint point source embedded in the innermost disk, at a projected distance of ≈ 38 AU and at a position angle of $(70 \pm 2)^\circ$, with a magnitude in the L' band of $15.8^{+0.75}_{-0.45}$ mag. The detection was very uncertain, with a signal to noise ratio of $\simeq 2$.

HD141569 was observed on the 2nd May 2016 in P97 (PI: Henning T. K., Segransan D., Quirrenbach A.; Program ID: 097.C-0206(A)). Table 1 reports the information about the dataset and the observation. Its data were partially discarded. In particular I deleted the datacube whose parallactic angles made a jump between -180° and 180° . Furthermore, some of the files presented anomalies, meaning that only 10 images per datacube were saved. This could have caused large imprecisions during the last phase of the process, since during the stacking operation different amounts of images and associated angles for the de-rotation were averaged together. Consequently the first 13 downloaded datacubes were discarded, ending up with 103 datacubes, each with 100 different images.

The dark calibration has been performed using calibration files of the night later, the 3rd May 2016, as no dark file was available in the ESO Archive. These files were used for the data reduction of both the coronagraphic and the photometric frames.

Since the histogram of the average values is distributed between positive and negative values and peaks around 0 counts, the normalization was removed from the pipeline.

3 Methods

Aim of this project was to reduce and analyze VLT/NACO data, determine the detection limits and characterize the signals, in the case of a possible planet detection. Many different steps have been necessary and they will be explained in this section. Section 3.1 presents the data reduction prior to the image analysis; Section 3.2 describes the PSF subtraction and the *PynPoint* package; Section 3.3 explains how the detections have been quantified and confirmed; Section 3.4 illustrates how the signals were characterized; Section 3.5 shows the method used to create contrast curves. Finally, Section 3.6 compares different parameters used for the analysis, pointing out the best values used during the work, and compares the different characterization methods, in order to identify the more powerful one in the determination of the signal properties.

3.1 Pipeline and data reduction

In this section, I will explain the steps necessary to reduce and prepare the data for the analysis. A schematic representation of the whole process, based on the existing pipeline developed by Markus Bonse in his Bachelor Thesis, is given in Fig. 1. The first step was to reduce the dimension of the images, since I was interested only in the region close to the central object. This action was also necessary to increase the velocity of the next steps, as the number of pixel at each operation is reduced from 768×776 to 300×300 per image. In the second step, I subtracted the mean of all the dark frames from the SKY and SCIENCE images, in order to correct for non-data signals. The third step was the bad pixel cleaning. The pipeline checked if every pixel had a value deviating more than 5σ from the image mean and substitutes it with the mean of the values of a 9×9 box around that pixel. Bad pixel cleaning was performed on both the SCIENCE and SKY frames.

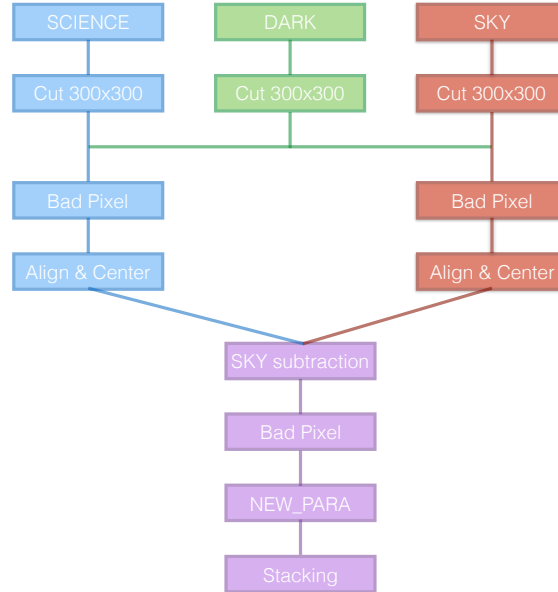


Figure 1: The schematic of the reduction pipeline. The steps regarding the SCIENCE images are in blue, the ones of the DARK frames in green and the ones of the SKY frames in red. Violet has been used for the steps regarding the combination of SCIENCE and SKY frames.

Later, in each frame the star was fitted with a 2D gaussian and the images shifted, so that all the maxima positions corresponded. At the end of this process, all the images were aligned with a precision of $1/100$ of a pixel. Similarly, a second cut of the image dimension centering the maximum of the gaussian of the first image was performed. This allowed to have the desired form for all the files and the star exactly in each center. The following step was the background subtraction. There are different possibilities to subtract the SKY frames to the SCIENCE frames: ‘*next*’, ‘*previous*’ and ‘*both*’ modes. In the ‘*next*’/‘*previous*’ mode, one subtracts to each SCIENCE frame the mean of the next/previous SKY

datacube. With the *both* mode, the average between the means of the previous and next SKY datacubes are subtracted. I used the *both* mode as it is more precise and leads to better results (see Section 3.6.1). After this operation, another bad pixel cleaning on the resulting images has been applied.

As already mentioned, every image is slightly rotated with respect to the previous one, since the instrument derotator on the detector, responsible to follow the sky rotation over the night, was turned off. Two important properties for each datacube are given in the header file: ESO ADA POSANG and ESO ADA POSANG END. They represent the angle of each frame with respect to the north direction. The images had to be derotated by this angles in order to be aligned with north pointing to the top and east pointing to the left.

To calculate the position angle of every single frame, the pipeline divided the range between the values of the two keywords into 100 equal intervals and assigned to each image a different angle. If the angles within the same datacube jumped from -180° to $+180^\circ$, the whole .fits file had to be discarded, since the interpolation would lead to angles evenly distributed every 3.6° on the entire circumference. Starting from the end of this operation, the calculated angles were in the header under the keyword 'NEW_PARA'.

Because the number of images for each object was very large (of order 20 000 images), it was extremely time-consuming to use all of them separately. Therefore, I proceeded to a stacking, in which a given number of images (this parameter will be called *stack*) was averaged together. The 'NEW_PARA' angles were also averaged to a single value. It was therefore important that the stacking number is a divisor of the number of frames within a datacube. However, during this operation one might lose information and precious details for the detection. The choice of the *stack* value will also be discussed in Section 3.6.1. Lastly, one could take only a subset of the frames of the final datacube. This operation could be necessary to confirm a detection, when the entire analysis was repeated with only part of the data (see Section 3.3).

The photometry files underwent a similar pipeline with substantially three main differences. First, the background subtraction occurred subtracting the mean of the count value per pixel in a circle of width 5 pixels at the edge of the 100×100 pixels image. Secondly, no 'NEW_PARA' parameter was needed. Lastly, at the end of the process, images were normalized to the exposure time of the SCIENCE frames, since often photometry images have shorter exposure times to avoid pixel saturation, and were averaged in one single frame. This image has then been used as PSF reference for the simulations of pointlike planets.

3.2 Angular Differential Imaging and PynPoint

Once the data have been calibrated, aligned and the background has been subtracted, one can proceed with the PSF subtraction. In order to remove every residuals, I used *PynPoint* (Amara and Quanz, 2012; Amara et al., 2015), which is a Python package for the analysis of ADI data (Marois et al., 2006). Using Principal Component Analysis (PCA, see Shlens, 2014), planets can be revealed in high contrast imaging data. The package first cuts circularly the images and then adds a circular mask of the desired dimension on the center, suppressing the star light. In this preliminary phase, the package also normalizes every image to its total luminosity, i.e. it divides the value of each pixel by the total amount of counts in the image, in order to have a new frame with total luminosity of 1 count. This step could not be performed on all the datasets because of the systematic presence of images with a negative total amount of counts (see Section 3.6.2). Indeed, a total negative value results in changing the sign of every feature, even a potential point source. As a consequence, when the frames are combined, the positive signal still present in many of them is partially suppressed from the negative one of the images with negative sum of counts. The package then creates a set of orthogonal functions ϕ_i which are used as a basis to reconstruct the PSF of the star. The latter is approximated through a linear combination of the basis functions

$$I(x) = \sum a_i \phi_i(x),$$

where $I(x)$ is the image of the PSF residuals (after the masking), $\phi_i(x)$ are elements of the basis and a_i are the coefficients for each basis function, defined by

$$a_i = \int I(x) \phi_i(x) dx,$$

which is basically the projection of $I(x)$ on the basis element ϕ_i .

Once the basis is constructed, the desired number of PC coefficients can be calculated and subtracted

from every image. This number has to be smartly chosen: during the analysis a too large number would lead to over-subtraction, i.e. the signal of the planets is also modeled and subtracted, while a too small number would not subtract sufficiently the PSF, not revealing the planet.

The last step is the de-rotation of the images left in the cube by the `NEW_PARA'` angle and the calculation of the mean of the stack. At this point, the north in the image already points to the top and east to the left: any potential companion bright enough should be visible.

3.3 Detection

After the PSF subtraction, I looked for companion candidates in the vicinity of the star. Once a signal was detected, it needed to be confirmed repeating the analysis with different combinations of parameters. For example, the candidate signal should be visible for a range of different consecutive PC numbers and not just in one single case. Other varying parameters were the radius of the central mask, which blocked the star light, the dimension of the image, and the amount of stacked images in the datacube. If using different parameters the signal still persisted, I investigated only half of the dataset (the first half or a randomly chosen subset), as it was enough to detect the signal of a physical source.

In order to characterize the detection, the False Probability Fraction (FPF) was calculated using the formula for small IWA suggested by Mawet et al. (2014). In their paper, they showed that, at very small angular separations, the statistical penalty increases because of the lack of a big sample statistics, leading to higher values of False Alarm Probability. To deal with the poor knowledge of the speckle statistics, they suggested to use the robust Student t-distribution and to perform the t-test for high contrast imaging at small IWA, calculating the p-value via

$$p_t(x, n_2 - 1) = \frac{\bar{x}_1 - \bar{x}_2}{s_2 \sqrt{1 - \frac{1}{n_2}}}, \quad (3)$$

which then gives a FPF value of

$$FPF = \int_{\tau}^{+\infty} p_t(x, n_2 - 1) dx. \quad (4)$$

In Eq. 3 and Eq. 4, x_1 is the signal aperture, x_2 is the set of apertures used as sample statistics (apertures of the same radius and at the same distance from the central star as the signal aperture), n_2 is the number of apertures in x_2 , s_2 is the standard deviation of x_2 and τ is the chosen detection threshold.

The FPF value strongly depends on the reference apertures and their size r , which appears in Eq. 3 through the directly dependent n_2 . A smaller aperture radius not only increases the strength of the signal, avoiding the consideration of pixels or pixel fractions dominated by the noise, but also increases the number of reference apertures, leading to a better characterization of the underlying distribution and therefore to a much smaller probability of false positives. The dependency of the aperture radius on the detection limits will be shown in Section 3.6.1.

This method avoids the use of the gaussian concept of σ -detection, which implies a clear gaussian distribution of the reference apertures. Since it cannot be stated that the apertures are normally distributed if they are only a few, it does not make any sense to use the classical S/N definition as a conclusive norm. To summarize, a detection implies a strong signal, which does not depend on the chosen parameter but that can be recovered using different values for the analysis variables. The probability that the retrieved signal is a statistical outlier or an instrumental artifact can be statistically characterized using Eq. 4.

3.4 Signal characterization

In case the FPF value was below the threshold for a chosen confidence level and the detection was confirmed, I applied two different methods to perform astrometric and photometric studies of the signal: the `AstroPhoto` routine, which was developed by Arianna Musso Barucci during her Master Thesis, and the `HesseMatrix` routine, which minimizes the curvature of the surface.

The `AstroPhoto` routine first inserts a fake bright planet at different positions close to the signal, in order to determine its actual position. This operation is necessary because, computing the point source position in the *PynPointed* image, gives a non reliable result, since the analysis, and in particular the de-rotation, could slightly shift the signal. To overcome this problem and to investigate how the analysis

processes it, the bright signal is directly added in the raw rotated images.

This kind of astrometric analysis is more precise if images of larger dimensions are used during each operation; therefore the amount of pixels was increased, dividing each figure element in four or more new ones. The parameter indicating the amount of parts in which every pixel side is divided will be called *subpix*, and was set to be 5 during every analysis, unless specified.

In a second phase, fake negative planets of different magnitudes are inserted in the previously determined position, subtracting flux from the raw images. The code then analyzes the aperture statistics for every case and interpolates the calculated FPF, finding the magnitude value that maximizes it. This means that the planet is subtracted in a way that the new signal aperture has the highest probability to be drawn out from the underlying distribution of the reference apertures.

The values of contrast and angular distance are then combined with the brightness of the star in the L' band and with the calculated distance from the Solar System, in order to obtain the physical projected distance and the apparent and absolute magnitude of the signal.

Errors on the angular distance and on the position angle take into account only the uncertainty due to the finite grid used for the insertion at the given subpixel scale, while the one for the physical distance also considers the uncertainty in the parallax measurement. As it will be shown in Section 3.6.3, the position uncertainties are highly underestimated. The upper and lower errors on the magnitude contrast are calculated interpolating the FPF as a function of the contrast magnitude at the position corresponding to a value of 0.16, calculated from Eq. 4 for a confidence level of 68%.

The HesseMatrix algorithm calculates the sum of the absolute values of the determinants of the hessian matrices within the signal region. The hessian matrix represents the second derivative of a more-dimensional function, and its determinant is a measure for the curvature of the surface described by the function. Considering the sum of the determinants in different positions (10 000 in this work) allows to sample the curvature in an extended region, called Region Of Interest (ROI), of variable size and to compare the surfaces of different post-processed images.

The routine then uses the Nelder Mead algorithm to minimize this value, inserting fake negative planets with the best combination of contrast and position, to make the signal disappear and to make the surface as flat as possible. Since the interpolation tries to reproduce also the small deviations from pixel to pixel, before the curvature analysis the images are convolved with a gaussian kernel with FWHM 1 pixel, in order to flatten their surface and to have comparable results. The threshold for the convergence of the results could be chosen: if the change in each variable between two consecutive iterations is less than the given tolerance, the algorithm has converged and the optimization returns those values for contrast and position. During every analysis the tolerance for the convergence was set to be 0.2.

Errors in the distance and position angle take into account the tolerance given for the converging algorithm and the finite grid due to the *subpix* parameter. Errors in the contrast magnitude consider only the uncertainty due to the tolerance of the optimization.

For both algorithms the errors on the final apparent and absolute magnitudes of the signal also consider the uncertainty in the measurements of the stellar photometry and distance.

The most important advantage of the second method is that the astrometric and photometric studies are performed at the same time, and every error in the photometric analysis, due to unprecise measurements during the astrometric one, is avoided. In the AstroPhoto routine the result does depend on the values of the reference apertures and any slight shift of the signal peak, due for example to a different number of subtracted PC, implies the consideration of a different sample of pixels. Therefore, the final results obtained with the AstroPhoto routine may strongly depend on the amount of principal components one decides to remove, making this method potentially dangerous and unstable.

On the other hand, the minimization of the curvature does not depend on the pixel values of regions without signal and it is more robust against PC variation. A further comparison of the two methods is presented in Section 3.6.3.

After the astrometric and photometric analysis of the planet, I estimated the physical distance between the central star and the planet. For this, the disk inclination and position angle were required. The first represents the tilt between the sky plane and the disk plane, while the second is the angle (north to east) in the sky plane between the line of intersection of the sky plane with the orbital plane and the north direction. In addition, the assumption that the planet is forming and currently laying in the disk was made. First of all the reference system was rotated, so that the disk position angle was 90° . Consequently the position angle of the planet got transformed in $PA_f = PA_i - (PA_{disk} - 90^\circ)$. At this point the inclination was the only parameter which described the disk plane and it was sufficient to de-project the disk to get the physical distance between object and star. To estimate the errors, the

described process was repeated for every possible combination of values. Three values were evaluated for every parameter: par , $par + \delta par$, $par - \delta par$, where par is the value of the parameter and δpar its uncertainty. Since the parameters required for the calculation are five (inclination angle, position angle of the disk, position angle of the planet, radial projected separation and stellar distance), a total of 243 possible combinations were considered. Among all the physical distances obtained for each set of parameters, the maximal and the minimal values were chosen to represent the uncertainty.

From the physical distance from the star, it is possible to derive the orbital period, which is obtained under three assumptions: (1) that the planet is orbiting the star circularly; (2) that it lies in the disk and its orbit follows the disk orientation; and (3) that its mass is considerably small with respect to the one of the central star. The value is obtained using the third Kepler's law,

$$P = \sqrt{\frac{4\pi^2}{GM_*} a^3}. \quad (5)$$

The errors are calculated considering the uncertainties in the mass estimation δM_* and in the physical separation from the star δa through the formula

$$\delta P = \sqrt{\left(\sqrt{\frac{4\pi^2 a^3}{G}} \frac{\sqrt{M_*}}{M_*^2} \delta M_* \right)^2 + \left(\frac{3}{2} \sqrt{\frac{4\pi^2}{GM_*}} \sqrt{a} \delta a \right)^2}, \quad (6)$$

where G is the the universal gravitational constant, M_* the mass of the stellar object and a the radius of the circular orbit.

After the astrometric and photometric analysis of the planet, one can make some assumptions on its mass, e.g. using the evolutionary model proposed by Baraffe et al. (2003), which gives an estimation of the mass of the companion if its age and its luminosity are known. This estimation must be used very carefully, because during the formation most of the light emitted by the object may be due to the accretion from the circumplanetary disk onto the forming planet (see Section 5.3). The uncertainties are equivalent to the evaluation of the COND models of the extreme cases: the brighter older combination for the upper limit and of the fainter younger combination for the lower limit.

3.5 Contrast curves

For all the datasets, detection limits are calculated through a contrast curve. A contrast curve gives the contrast magnitude with respect to the central star that can be reached at any distance from the central object, according to a chosen norm. The norm in this project was chosen to be the FPF value calculated from Eq. 4 for the confidence level (CL) of 99.999% unless specified. The norm is used to determine the conditions necessary to see the planet: if the the FPF value is lower than the threshold necessary to claim a detection within the chosen CL, then the planet is seen; otherwise its signal is not strong enough to be observed.

At the beginning, one has to choose the number of positions to investigate and their distribution within the image. These can be determined by two parameters: the radial step and the angular step. In a first phase the positions on the horizontal line from the center to the right side of the image, with distance from each other equal the radial step, were chosen, taking into consideration also the central mask and the dimension of the inserted rescaled PSF. In a second phase they were rotated by the angular step around the center of the images for the number of times necessary to complete a round. This process gave the positions the algorithm would investigate, distributed on $\frac{360^\circ}{\text{angular step}}$ lines in the radial direction from the center. In order to calculate the final detection limits for each object, I set the angular step to be 20° and the radial setup to be 4 pixels. Those numbers resulted in 162 considered positions.

At each position, the routine inserted a fake planet with an estimated magnitude contrast given by the user, and then calculated the FPF value of its aperture. If the FPF value is larger then the threshold, it inserted a planet 1 mag brighter until the value got smaller than it. As soon as the FPF layed below the threshold, the brightness of the planet was changed again, with a contrast 0.2 mag higher, until the FPF crossed the threshold value. The final maximal magnitude for a detection was given by the linear interpolation of the contrast as a function of the FPF at the position of the threshold. When every position had a magnitude value, a 2D map of the surrounding region of the star could be produced, showing where the analysis achieved lower brightnesses.

Once the 2D map was completed, I averaged azimuthally the values of the positions at the same distance from the center, in order to obtain a radial profile of the reachable contrast. This final operation resulted in a contrast curve, which represented the sensitivity that can be reached with the current techniques and with the used data reduction as a function of the angular separation from the star. These plots indicate the conditions in terms of brightness that a planets is likely to have in order to be seen. The fact that no companion was observed does not mean that no planet is orbiting the star, but puts constraints on the brightness of any potential companion which could not be detected.

Because the analyzed objects often have distances of several hundreds of parsecs, plotting the contrast curves at several arcseconds may not be very useful for the search of planets. However, it quantifies the detection limits I can reach, in order to compare them and the pipeline to the ones of other works.

3.6 Optimization and choice of the analysis variables

In this section I will motivate some parameters chosen during the analysis (Section 3.6.1) and demonstrate the presence of two types of datasets, differing from each other for the presence of images with negative sum of counts (Section 3.6.2), that could have important consequences on the signal detection. Finally, in Section 3.6.3, the two characterization methods described in Section 3.4 will be compared, concluding that the HesseMatrix method is extremely more robust against PC variation and more precise in determining the true planet position.

3.6.1 Background subtraction mode, *stack* parameter and aperture size

In this section, the influence on the detection limits of some of the most important parameters is studied, for example the way the background is subtracted, the number of images averaged together before the analysis and the size of the apertures considered for the FPF study. Figure 2 shows the influence of different background subtraction methods and of the *stack* parameter on the detection limits in the surrounding regions of HD259431. All the curves were generated interpolating the magnitudes of the fake inserted planets necessary for a detection within a 99.99% CL (for which the FPF value corresponds to 5×10^{-5}) at different locations. The positions were radially chosen every 5 pixels and the angular step was set to be 120° .

It is difficult to generate a contrast curve at very small separations for two reasons: first, the residuals of the PSF and the speckles make it difficult to have clear signals; and second, reaching low FPF values is complicated and extremely bright objects have to be inserted. Therefore, in addition to the mask of 4 pixels in radius to block the star light, I started the analysis at a distance of 10 pixels from the center of the image, to avoid the innermost central region.

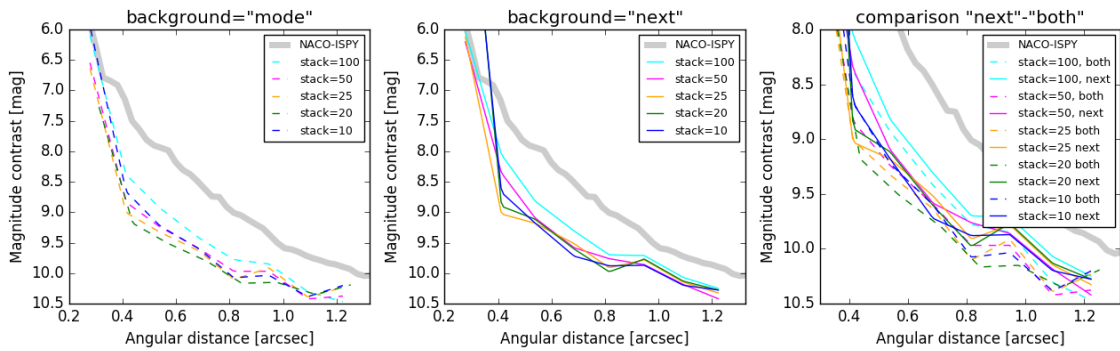


Figure 2: Detection limits for HD259431 for different *stack* numbers. *Left:* The plot shows the contrast curves obtained when subtracting the average image between the previous and the next sky frame. The curve is lower using smaller *stack* numbers, since more details of the original frames are kept and higher magnitudes can be reached. *Center:* The contrast curves when only the next sky frame is subtracted are shown. Again, the analysis is more efficient for lower *stack* numbers. *Right:* Comparison for *stack*= 100, 50, 25, 20, 10 of the two subtraction modes. For all the cases the mode ‘both’ is slightly more powerful and can lead to the detection of fainter planets with respect to the ‘next’ mode.

Figure 2 compares different subtraction methods and different *stack* numbers. All the curves are the result of the subtraction of 25 principal components and during the statistical analysis apertures of radius 2.5 pixels were considered for all of them. Depending on the distance from the star, other amounts of PCs

may better reveal signals, but reaching the highest possible contrast value is beyond the scope of this plot, which wants to compare different *stack* values and background subtraction methods.

The figure shows that, averaging more than 20-25 images each time decreases the precision and efficiency of the analysis. The gain in terms of contrast stacking 10 images is very small and the analysis would be much more time expensive. The increasing precision when using small *stack* numbers will be also discussed in Section 4 and will be essential for the detection of signals.

In addition to the increasing precision for lower *stack* numbers, there is almost everywhere an offset, between the contrast curves obtained subtracting the background differently, which ranges from 0 mag to almost 0.5 mag for the same *stack* number. At every distance from the central star the ‘*both*’ subtraction mode is more efficient in revealing planets than the ‘*next*’ one and reaches lower brightnesses. This implies that it is better to reduce the maximal temporal distance between SKY and SCIENCE at the cost of increasing the distance and the differences in weather conditions between the closest SCIENCE images to the SKY frames and the SKY frames themselves. From now on I will always subtract the background using the mode ‘*both*’.

Another very important parameter for the determination of contrast curves is the aperture radius used to determine the FPF value. A too large radius includes a lot of noise in the aperture, reducing the signal to noise ratio, while a too small radius does not include the whole signal. There is a second consequence of the radius dimension: the amount of reference apertures used for the determination of the underlying distribution and the FPF calculation gets larger. A larger radius implies much fewer background apertures, while a smaller one allows a much more precise characterization of the underlying aperture distribution, leading to smaller FPF values.

Figure 3 shows how the radius of the background apertures influences the reachable contrast. The radius does not affect the presence or detection of a candidate, but it points towards different FPF values, making the detection appear more or less robust. A direct consequence of the different radii, given the same signal, is visible in the contrast curves, since smaller diameters (of order $\frac{\lambda}{D} \approx 0.95'' \approx 3.5$ pixels) allow to reach fainter objects. The contrast curves of Fig. 3 were obtained using the *stack* = 100 datacube of the TW Hya dataset, considering the same position described at the beginning of this section, with a mask of 3 pixels in radius, and subtracting at each step 20 PCs.

The plot clearly shows that the aperture radius is a very important parameter for the determination of contrast curves, and that the best results are obtained for apertures of 1.8-2.0 pixels in radius. The larger gain between the curves obtained with radius = 3.0 pixels and the one obtained with radius = 2.0 pixels is of order of a few magnitudes and is observed at small separations from the central star. In this range, the higher number of apertures has the most powerful impact in defining the underlying distribution, strongly influencing the detection limits.

In summary, for the following analyses I will subtract the background using the mode ‘*both*’ and consider datasets with very small *stack* numbers. Unless specified, I will use for the contrast curve determination an aperture radius of 2.0 pixels.

3.6.2 Statistics on the images

After the cosmetic reduction described in Section 3.1, and before the beginning of the search for planets, the frame mean values in the datacubes were analyzed. Some datasets presented an issue which could have catastrophic consequences on the detection of companions, annihilating any signal in the images. The problem could be identified plotting the histogram of the mean values per frame. Figure 4 shows

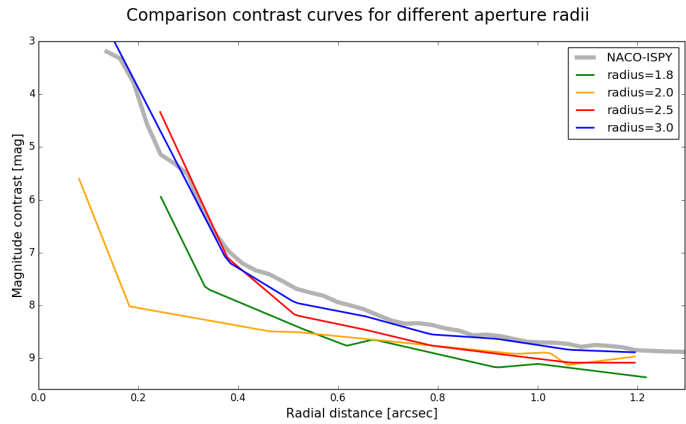


Figure 3: Contrast curves for the TW Hya dataset obtained considering each time apertures of different radii (CL=99.99%). The detection limits from the NACO-ISPY database are plotted in grey for a comparison.

the distribution of the average pixel value of each image for two datasets: TW Hya and HD179218. As one may see, the distribution of the values peaks around 0 for TW Hya and around 60 for HD179218, resulting in 44.8% (8116 of 18100) of the TW Hya frames having negative mean values. The origin of this systematic difference still has to be understood: in principle, one imagines that the presence of the star makes the images brighter and therefore leads to exclusively positive mean values. The presence of images with negative sum of counts implies that the SKY images are often brighter than the SCIENCE ones, and the background subtraction leads to those values. I will analyze this hypothesis in Fig. 5.

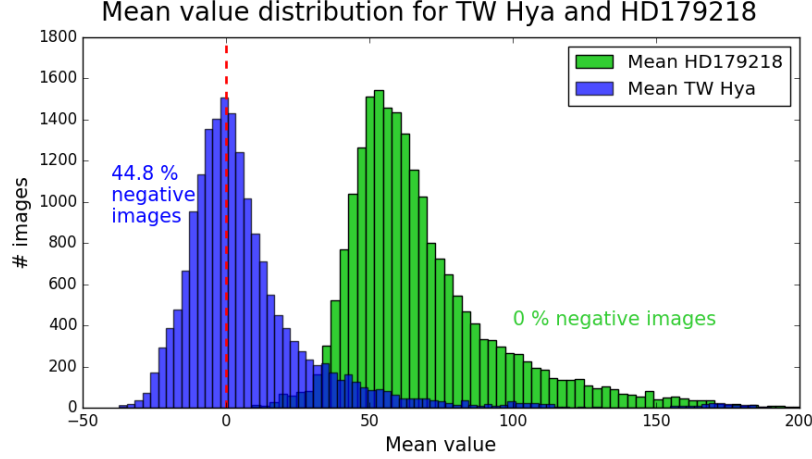


Figure 4: Histogram of the mean values of each image of TW Hya (blue) and HD179218 (green) just before the use of *PynPoint*. The red line separates positive and negative values. Many frames of the TW Hya dataset have negative mean values, which also means that the sum of the values of each pixels lies below zero. This may lead to the suppression of any potential signal. The same does not happen for HD179218, since no frame has a negative mean value. Every signal in the cube is maintained and can be revealed.

During the ADI analysis (see Section 3.2), all the images in the datacube are divided by the sum of the values of all their pixels, to make them as uniform as possible and to reduce the negative effect of bad frames in the detection of potential candidates. Some phenomena, like bad AO working, could cause the star and the AGPM coronagraph not to be perfectly aligned, leading to extremely bright images and, in extreme cases, in saturated pixels. Therefore, the final computation could lead to different results with lower detection limits, in particular in the innermost region, since the mean calculation would be dominated by those pixels. In the case of TW Hya, where the total image amount of counts is negative, this sort of normalization causes every value to be divided by a negative number and each pixel value to change sign. Therefore, when averaging the de-rotated frames during the last step, every potential planet signal in the negative frames annihilates, or at least dims, the one in the ‘positive’ frames. This implies that much brighter planets have to be present in the images in order to overcome the dimming. To solve this problem I investigated the average values of the images. Since the combination of star and AGPM coronagraph should be brighter than just the AGPM alone, and since the SCIENCE images should be brighter than the SKY ones, I expected to get only positive values after the subtraction. However, as shown in Fig. 5, where the values of each TW Hya’s SCIENCE frame and of its SKY frames are shown in the same temporal order as recorded during the observation, this was not always the case. The first plot reports the values of the whole 101×101 pixel image before the background subtraction, when the dark subtraction, the bad pixel cleaning, the alignment and the centering had already been performed. As one may see, many SCIENCE images have values which lay below the average of the previous and the next SKY frames, implying that they are actually fainter. The second panel investigates the center (16×16 pixels) of the images, where most of the light comes from the star and the AGPM coronagraph. As expected, the images including the star are much brighter and have larger mean values than the SKY frames. The third plot shows the 101×101 pixel image with the central 16×16 pixel square set to zero. In the region without the star, many SCIENCE frames are in average fainter than the SKY frames, causing the presence of negative images.

To overcome this problem, during the analysis of the datasets where the described systematic occurs, no normalization step was performed and the PSF was subtracted without any further operation. These datasets are TW Hya, HD34282, HD101412 and HD141569.

Average temporal evolution of TW Hya dataset

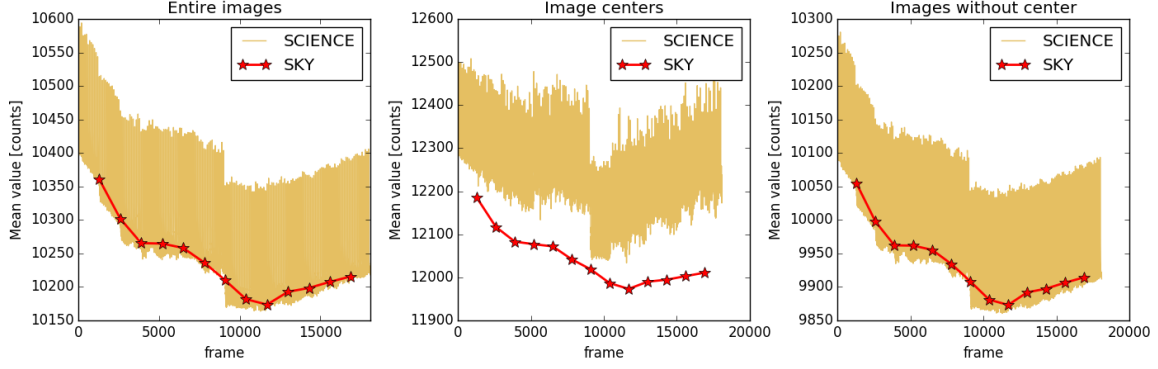


Figure 5: The plots show the temporal ordered mean value per image in the SCIENCE (orange) and SKY (red) frames of the TW Hya dataset. In the left one the values of every entire 101x101 pixels image are shown and clearly many SCIENCE frames are fainter than the nearest SKY ones. The second plot shows the values of the very central region of the image (16x16). In this case the presence of the star strongly increases the brightness of the images and there is no overlap between the two lines. Finally, the third plot shows the mean of the entire images, when the central region previously analyzed has been set to zero. Clearly the SKY images are often brighter than the SCIENCE frames, and the background subtraction is responsible for the distribution to peak around zero and to have 44.8% of elements with negative mean value. The jump that can be seen in the plots is due to a break in the observation.

3.6.3 Comparison of Characterization Methods

The absence of a planet in the surroundings of HD97048 (see Section 4.6.1) allows the investigation of the characterization methods, which cannot be performed on datasets with candidates, because the calculated FPF value at each step of the AstroPhoto algorithm would be distorted by the presence of the second signal.

In order to investigate the efficacy in characterizing the signals, a fake positive planet was inserted in the $stack = 100$ and $stack = 50$ datacubes of HD97048, with a magnitude contrast of 6.2 mag with respect to the central star at position [51,42]. Its position corresponded to a distance from the central star of $0.232''$ at the position angle of 183.4° . Location and contrast were chosen such that the signal was in the innermost image region and had a brightness comparable to those observed in the data.

For this analysis, a mask of 3 pixels in radius and $subpix = 5$ were used. The tolerance during the optimization of the HesseMatrix routine was set to 0.2 and the size of the ROI to 6 pixels. Within it, determinants in 100 evenly spaced points were summed. The aperture radius for the FPF analysis was fixed to 2.5 pixels.

I varied the number of subtracted PCs and looked at the results given by the two routines. The left panel of Fig. 6 reports the position where the planet should be, according to the AstroPhoto algorithm (blue) and to the HesseMatrix algorithm (red), after the analysis with the $stack = 100$ (circles) and the $stack = 50$ (squares) datacubes. The big central yellow star represents the actual position where the planet was inserted. The plot clearly shows that the distributions of the positions recovered by the two algorithms are very different. On one hand the positions given by the AstroPhoto routine are spread over a wide region with dimensions 4×5 pixels, with positions separated by 5 pixels after the variation of the number of subtracted PCs. On the other hand, the positions recovered by the HesseMatrix algorithm are much closer to the exact point where the planet was inserted and they are all located within a region of 0.6×1.0 pixels around the exact signal position. This behavior holds for both the analyzed datacubes. The right panel shows the magnitude contrasts, distances and position angles found by the two methods (AstroPhoto in blue, HesseMatrix in red) using the two datacubes ($stack = 100$ with circles, $stack = 50$ with squares) as a function of the amount of subtracted PC. The thick black line shows the correct value of the inserted planet. The mean value obtained considering the HesseMatrix estimations was 6.34 mag, while the one obtained using the AstroPhoto routine was 6.41 mag. Both methods tend to overestimate the contrast of the planet, set to be 6.2 mag, and they seem to be independent from the number of PC in the contrast estimation. Furthermore, no clear difference in the spread of the two distributions was visible, and both algorithms recovered contrast magnitudes up to 0.4 – 0.6 mag larger.

A different behavior is observed when looking at the distance from the center of the image (central plot of the right panel), where the values recovered by the AstroPhoto routine increase with the number of subtracted PCs. The reason could be that, when subtracting different numbers of components, the peak positions of the signal and of the inserted fake planets are always in different locations, and the shift

gets visible in the plot. Furthermore, it is not enough to consider only the errors due to the finite grid and the uncertainties are underestimated. On the contrary, distances obtained with the HesseMatrix algorithm for different amounts of PCs are consistent with each other and robust against PC variation. There seems to be no trend, and the mean of the obtained distances ($0.229''$) is very similar to the correct position, which is at $0.232''$.

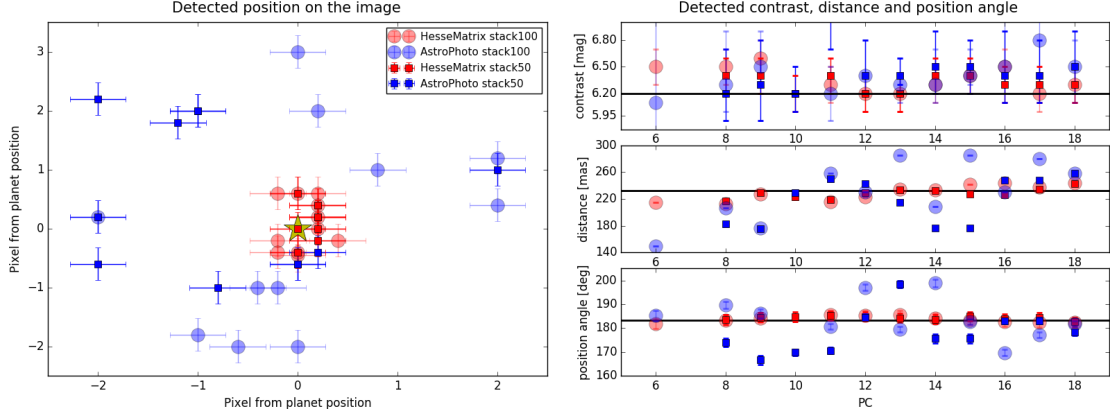


Figure 6: *Left:* position recovered by the AstroPhoto (blue) and the HesseMatrix (red) routines using the *stack* = 100 (circles) and the *stack* = 50 (squares) datacubes of the object HD97048 for different amounts of subtracted PCs. *Right:* magnitude contrast, distance and position angle found with the two methods as a function of the amount of subtracted PC. Markers and colors have the same meaning of the previous plot. The thick black lines represent the correct values at which the planet has been inserted.

A similar analysis can be done for the position angle. Once again the results obtained with the HesseMatrix routine for different numbers of PCs layed around a horizontal line, at the same value of the original position angle of the planet. For comparison, the mean of the recovered position angles was 183.9° , while the original value was 183.4° . A similar horizontal line could not be seen for measurements obtained by the AstroPhoto routine: the distribution was much wider, with some results differing of 13.7° and 15.5° from the original one. Also for the position angles, the uncertainty estimation of the AstroPhoto did not consider the large scatter of the values observable in the plot and the errors were largely underestimated. Furthermore, it is impossible to forecast for which number of PCs the analysis returns the correct results.

In summary, there are not important differences in the magnitude contrast inferred by the two algorithms and the uncertainty evaluation of the HesseMatrix routine underestimates the errors. However, the analysis concludes that astrometric results are much more precise and reliable using the HesseMatrix algorithm than the AstroPhoto routine, independently from the number of subtracted PCs. For this reason, I will use the HesseMatrix routine to characterize the signals through the manuscript.

4 Results

4.1 HD259431

4.1.1 Presence of a planet

The post-processed images of HD259431 show the presence of two point sources which will be identified as planet candidates HD259431b and HD259431c.

HD259431b is a companion candidate very close to the center of the image, showed in Fig. 7 for the $stack = 2$ datacube, radius of the mask = 4 pix and 6 subtracted PCs. In order to verify that the detection of the candidate HD259431b is not an artifact of the analysis or a PSF residual, I varied different parameters to investigate its robustness. More specifically, I varied the number of stacked images (100, 50, 25, 10, 5), the size of the central mask (2, 4, 7 pixels in radius), the size of the images (101, 201 pixels), the number of principal components (from 3 to 25), and the starting dataset, randomly selecting for the analysis only half of the frames. The search confirmed the detection, since for all the analyzed situations the signal was well distinguishable for at least a range of 20 PCs in the residuals. This was not the case when the central mask was 0.07, since a large part of the signal was covered by the mask. Using an aperture radius of 2.5 pixels, for 4-6 PCs, the FPF value dropped below the value corresponding to a CL of 99.999%. For those cases the SNR reached values of 30-35.

In conclusion, the analysis confirmed the detection of a very bright companion candidate to HD259431.

The companion characterization according to its position and magnitude contrast presented some challenges. To investigate the candidate the AstroPhoto routine was first used. For $stack = 100$, a central mask of radius 4 pixels and images of 95×95 pixels, the signal best disappeared when inserting a fake negative planet with a contrast magnitude of $5.6^{+0.4}_{-0.8}$ mag with respect to the central star at distance of $(0.140 \pm 0.003)''$ and at a position angle of $(60.9 \pm 1.1)^\circ$. Because of its strength, removing the signal properly and obtaining a clean residual image was very difficult.

To overcome the uncertainty and to properly characterize the signal, I applied the HesseMatrix routine considering determinants within a 6×6 pixel area around it. The $stack = 10$ datacube with a central mask of radius 4 pixels was used. The code suggested the presence of a signal at a distance of $(0.182 \pm 0.006)''$ and at a position angle of $(53.5 \pm 1.9)^\circ$. The estimated magnitude contrast was 5.2 ± 0.2 mag, implying that the apparent magnitude of the potential companion was 9.2 ± 0.4 mag. The recovered astrometric values are very similar to the ones found by Thomas et al. (2007), supporting the idea that HD259431b is a true companion.

The spatial separation and absolute magnitude strongly depend on the distance measurement chosen for the system characterization. All the values for both the distances from the Hipparcos and from the GAIA missions are reported in Tab. 2.

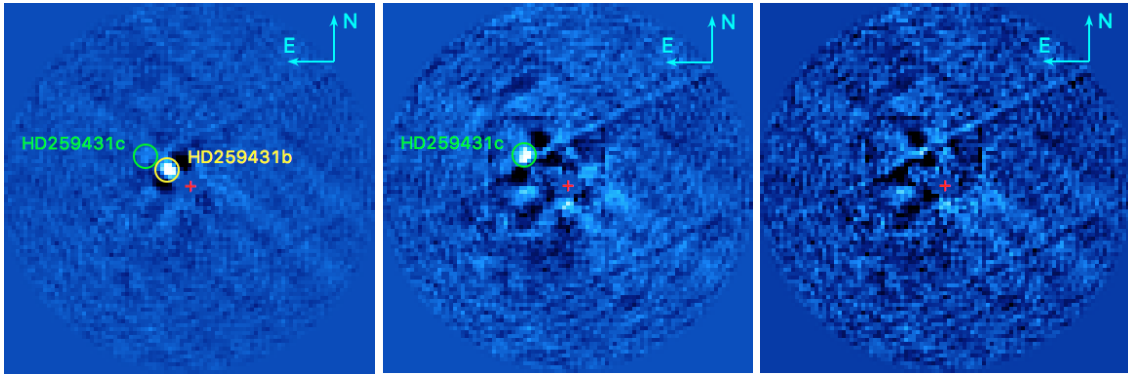


Figure 7: *Left:* original image of the surrounding of HD259431 after the PSF subtraction with 6 principal components, using the $stack = 10$ datacube and a mask with radius 4 pixels. The companion lays close to the star in the image. The oversubtracted regions on the two sides of the signal are clearly visible. *Center:* residual image after the subtraction of a signal with contrast 5.2 mag at the distance of $0.182''$ and position angle of 53.5° . Some residuals of the signal subtraction are visible in the form of a square of 30×30 pixels, but no residuals are left at the signal position. The subtraction revealed a second possible candidate, HD259431c. *Right:* residual image when also the second candidate companion is removed, inserting a negative point source with contrast 7.7 mag with respect to the central star at a distance of $0.355''$ and position angle of 57.6° . In all the images the red cross represents the position of the central masked star.

A more careful look at the residual image on the central plot of Fig. 7 revealed the possibility of a further companion which was hidden from the strong signal of HD259431b. The oversubtracted regions on both sides of the source are well distinguishable. To verify the presence of a physical point source in that position, I subtracted the bright signal of HD259431b in the raw non-stacked data. Subsequently I performed again the *PynPoint* analysis varying the central mask size (4 and 7 pixels in radius), *stack* (1, 2, 5, 10) and subtracted PCs (from 5 to 44 in step of 3). I also investigated a randomly chosen subset of the *stack* = 2 datacube. As the signal was present in all the cases, it is likely to come from a physical source. As further confirmation of the interest of this signal, denominated HD259431c, the FPF of the signal reached values of up to 8.9×10^{-8} or lower in all the analyzed parameter combinations, with a S/N ratio higher than 20 for an aperture radius of 2.0 pixels.

The characterization of HD259431c led to an object located at a distance of $(0.355 \pm 0.006)''$ from the center, with an angle of $(57.6 \pm 1.0)^\circ$ from the direction of the north. Its brightness in the L' band has been estimated to be 11.7 ± 0.4 mag, since its contrast with respect to the central star is 7.7 ± 0.2 mag. This estimates have been inferred using the HesseMatrix algorithm on the *stack* = 10 datacube, with *subpix*=5, range of interest of 8×8 pixels, a central mask of 4 pixels in radius and the subtraction of 6 PCs.

Table 2: Astrometric and photometric properties of the candidates HD259431b and HD259431c. The values of angular projected separation and magnitude contrast have been calculated from the data. For the others additional sources and archival data have been used.

| Object | Property | Hipparcos | GAIA |
|-----------|-----------------------------------|-------------------------|---------------------------|
| HD259431 | Apparent Brightness (mag) | 4.0 ± 0.2 | 4.0 ± 0.2 |
| | Distance (pc) | 289.9 ± 118.5 | 610.5 ± 108 |
| | Absolute Brightness (mag) | -3.3 ± 0.9 | -4.9 ± 0.5 |
| HD259431b | Apparent Brightness (mag) | 9.2 ± 0.4 | 9.2 ± 0.4 |
| | Absolute Brightness (mag) | 1.9 ± 1.0 | 0.3 ± 0.6 |
| | Angular Projected Separation (as) | 0.182 ± 0.006 | 0.182 ± 0.006 |
| | Projected Separation (AU) | 52.8 ± 21.6 | 111.1 ± 20.1 |
| | Position Angle ($^\circ$) | 53.5 ± 1.9 | 53.5 ± 1.9 |
| | Physical Separation (AU) | $60.8^{+30.0}_{-26.9}$ | $128.0^{+31.9}_{-28.9}$ |
| | Orbital Period (yr) | 178^{+134}_{-120} | 545.6^{+213}_{-195} |
| | Mass (M_J) | ~ 820 | — |
| | Apparent Brightness (mag) | 11.7 ± 0.4 | 11.7 ± 0.4 |
| HD259431c | Absolute Brightness (mag) | 4.4 ± 1.0 | 2.8 ± 0.6 |
| | Angular Projected Separation (as) | 0.355 ± 0.006 | 0.355 ± 0.006 |
| | Projected Separation (AU) | 102.9 ± 42.1 | 216.7 ± 38.8 |
| | Position Angle ($^\circ$) | 57.6 ± 1.0 | 57.6 ± 1.0 |
| | Physical Separation (AU) | $114.5^{+51.7}_{-48.8}$ | $241.1^{+51.6}_{-48.9}$ |
| | Orbital Period (yr) | 462^{+317}_{-300} | 1411^{+480}_{-458} |
| | Mass (M_J) | $104.5^{+98.4}_{-41.2}$ | $377.5^{+274.9}_{-168.4}$ |
| | Apparent Brightness (mag) | 11.7 ± 0.4 | 11.7 ± 0.4 |

In Tab. 2 one can see the important influence of distance estimation on some parameters, for example on the absolute magnitude and on the physical projected separation from star to signal. In fact, considering the GAIA data, HD259431c has an absolute magnitude of 2.8 ± 0.6 mag and it is 216.7 ± 38.8 AU far away from the star in the sky projection. However, if one assumes the Hipparcos data to be correct, the absolute magnitude is 4.4 ± 1.0 mag and the separation 102.9 ± 42.1 AU. According to the distance assumption, the candidate is 1.6 mag brighter and its distance from the central star is more than double.

The physical distance and the orbital period calculated using Eq. 5 have much larger errors if it is considered that the position angle of the disk was highly uncertain. Errors on those values take into account only the uncertainty in the companion angular distance, in its position angle, and in the stellar distance, neglecting the uncertainties in the disk orientation, i.e. in its position angle and inclination. The mass is obtained interpolating the COND models from Baraffe et al. (2003), assuming the system to be exactly 1 Myr old. Errors refer to the values obtained interpolating the models at the position of the absolute magnitude when upper/lower errors are added/subtracted. The different values of the Gaia and the Hipparcos parallaxes translate in a difference of more than 250 M_J for the candidate HD259431c. No mass estimation could be done for the candidate HD259431b when considering the GAIA distance, since the COND models could not be interpolated at such low magnitudes. In the case of the Hipparcos measurements the value of the magnitude, considering the lower error, exceeded the interpolation range of the COND models and therefore only a rough estimation without errorbars is given.

4.1.2 Detection limits

To calculate the detection limits of the $stack=20$ datacube of HD259431, a total of 162 positions were considered, with the subtraction of 25 principal components at each image generation. Before the algorithm started, the two signals were completely removed from the dataset.

The result is shown in Fig. 8: the 2D map indicates where the algorithm is more efficient in finding planets (red regions) and where it is more difficult to detect them (yellow regions). In the outer region of the image planets up to 3.5 mag fainter can be observed. In the image the two found companion candidates are shown with black stars. In the south western region with respect to the central star, limits are slightly worse.

The contrast curve in the bottom panel of Fig. 8 is the interpolation of all the azimuthally averaged contrast values from the map. Again, black stars show the positions of the previously described companions and their contrast magnitude. It can be seen that, subtracting 25 PCs, FPF values below the 99.999% CL for both sources would not have been reached. This amount of subtracted components was chosen after a quick optimization, in which 3 different values were investigated to decide for which one the curve had to be produced. Indeed, it allows to reach higher magnitudes in regions of the image other than the innermost one. Starting from $0.35''$ the pipeline presented in Section 3 is able to reach limits 1 mag fainter than the ones reached by the NACO-ISPY consortium.

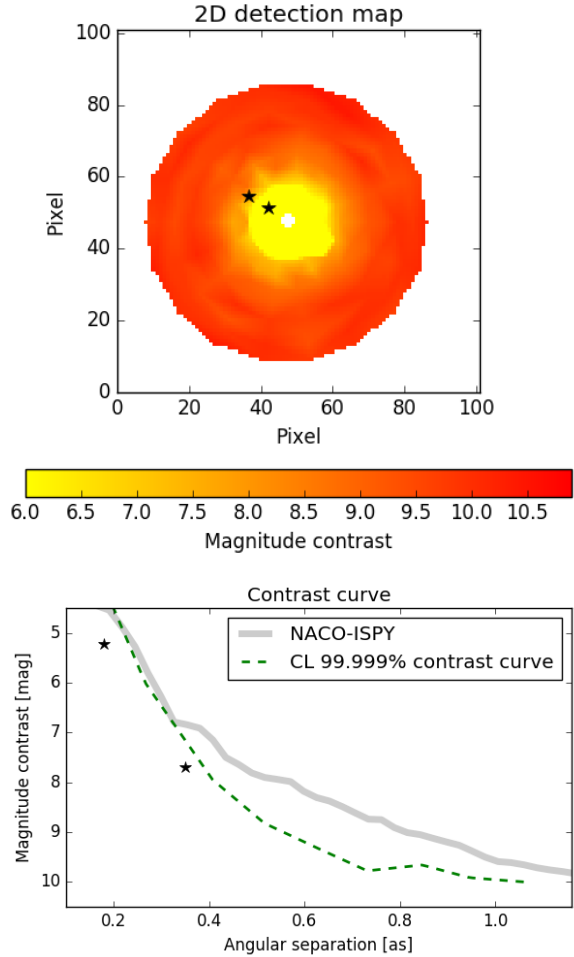


Figure 8: *Top:* 2D detection map of the surroundings of HD259431. Hotter colors represent lower magnitude contrast. *Bottom:* detected contrast curve after the consideration of 162 positions. As one may see the gain with respect to the result of the NACO-ISPY consortium is very important.

4.2 HD34282

4.2.1 Presence of a planet

The search for planets embedded in HD34282 disk revealed a strong signal in the central region, south from the star. Figure 9 is obtained using the entire dataset, applying a mask of radius 4 pixels in a 101x101 pixels image and subtracting 36 PCs. The north points to the top and the east to the left. Using an aperture radius of 1.8 pixels ($\approx \frac{\lambda}{D}$), the best FPF value that can be reached is 0.00024, which corresponds to a CL of 99.95%. In this case the S/N ratio is 13.3.

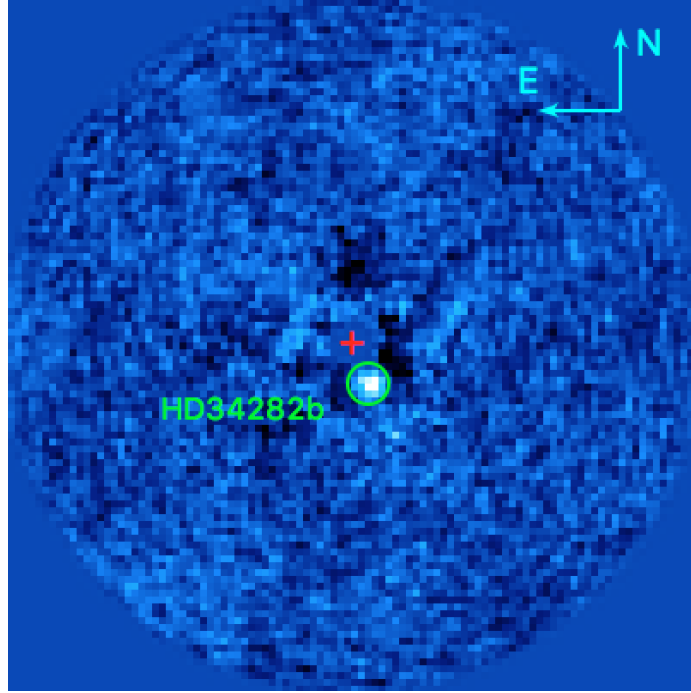


Figure 9: Final *PynPointed* image of HD34282. A clear signal close to the center is clearly visible. In this case $stack = 1$, $PC = 36$, central mask radius = 4 pix were used.

Despite the fact that the FPF value is not low enough to statistically guarantee a detection within the 99.999% CL, the signal is very strong and persistent, and different tests have been conducted in order to verify its robustness. It turned out that the detected source is clearly observable for different *stack* numbers (1, 2, 5, 10) combined with different central masks (2 and 4 pixels in radius) and the subtraction of different amounts of PCs (29-39). Lastly, half of the $stack = 2$ datacube has been randomly selected and analyzed. In this case the signal is present and strong for both the mask values and for the same range of PCs. The signal peak layed a few pixels further out from the donut produced by the AGPM subtraction.

Following Section 3.6.3, I performed the optimization of the HesseMatrix routine in order to minimize the curvature of the image surface in the source region. During the creation of the residual images, 35 PCs were subtracted each time from the $stack = 5$ datacube, and the stellar light was suppressed with a mask of 2 pixels in radius. Fake planets were inserted using *subpix* = 5, which means that every pixel was divided into 25 subpixels. Considering the surface occupied by the signal and its vicinity to the mask, a ROI of 6x6 pixels was investigated.

The HesseMatrix algorithm estimated the planet to be at the position $[D, PA] = [(0.143 \pm 0.008)'', (200.3 \pm 3.1)^\circ]$ and its magnitude contrast to be 6.2 ± 0.2 mag. In Fig. 10 a negative planet of this magnitude at the same position has been inserted. It can be seen that the original signal has completely disappeared, indicating that the position and the brightness calculated by the algorithm correspond to the correct candidate values. These results were combined with the apparent magnitude of the star (6.6 ± 0.1 mag at $3.8 \mu m$) and with its distance for both the parallax estimations from the GAIA and the Hipparcos missions. The combination led to the apparent and absolute brightness of the object and its physical projected distance. The values are reported in Tab. 3.

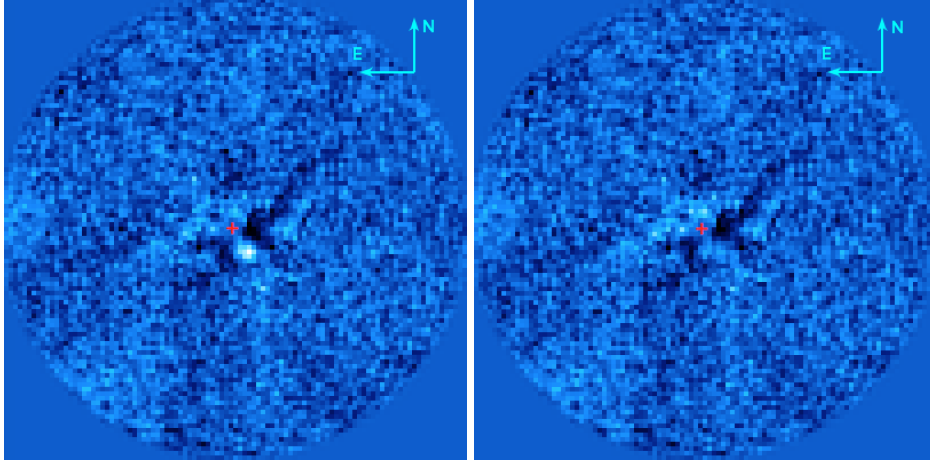


Figure 10: On the left the original image of the companion of HD34282. On the right the image after the insertion of a negative planet with luminosity 12.7 mag, 0.143 as far away from the center in the direction 200.3° with respect to the north.

An estimation of the object mass using the COND models from Baraffe et al. (2003) indicated the possibility that the candidate found has a mass of $45^{+38}_{-20} M_J$ for the absolute magnitude of 6.7 ± 0.6 mag, and of $170^{+59}_{-51} M_J$ for 5.3 ± 0.3 mag. For this determination the age from Merín et al. (2004) was assumed.

Table 3: Properties of HD34282 and of its candidate companion for the study performed with the HesseMatrix algorithm. Both the distance measurements from GAIA and from Hipparcos have been considered.

| Object | Property | Hipparcos | GAIA |
|----------|-----------------------------------|------------------------|-------------------------|
| Star | Apparent Brightness (mag) | 6.6 ± 0.1 | 6.6 ± 0.1 |
| | Distance (pc) | 163.9 ± 43.8 | 325.1 ± 30.9 |
| | Absolute Brightness (mag) | 0.5 ± 0.6 | -0.9 ± 0.2 |
| HD34282b | Apparent Brightness (mag) | 12.8 ± 0.2 | 12.8 ± 0.2 |
| | Absolute Brightness (mag) | 6.7 ± 0.6 | 5.3 ± 0.3 |
| | Mass (M_J) | 48^{+38}_{-20} | 170^{+59}_{-51} |
| | Angular Projected Separation (as) | 0.143 ± 0.008 | 0.143 ± 0.008 |
| | Projected Separation (AU) | 23.4 ± 6.4 | 46.5 ± 5.1 |
| | Position Angle ($^\circ$) | 200.3 ± 3.1 | 200.3 ± 3.1 |
| | Physical Separation (AU) | $23.6^{+9.3}_{-7.5}$ | $46.8^{+9.6}_{-7.2}$ |
| | Orbital Period (yr) | $91.4^{+54.2}_{-43.3}$ | $255.3^{+79.0}_{-59.6}$ |

To estimate the physical distance between the central star and the planet, the disk parameters from Piétu et al. (2003) were used. The method described in section 3.4 de-projects the disk and reveals the physical separation between planet and star, which is in this case $23.6^{+9.3}_{-7.5}$ AU and $46.8^{+9.6}_{-7.2}$ AU according to the stellar distances 163.9 ± 43.8 pc and 325.1 ± 30.9 pc, respectively. The difference between the projected and the de-projected separation is very small, indicating that the planet is very close to the intersection between sky plane at the star distance and orbital plane. Furthermore, the fact that the position angle of planet and disk differ from $\sim 180^\circ$ strongly support the hypothesis that the planet is embedded in the disk.

4.2.2 Detection limits

The detection limits of HD34282 have been calculated using the $stack = 20$ datacube and using a mask of 4 pixels in radius. The limits are shown in Fig. 11. The innermost region was compromised by the

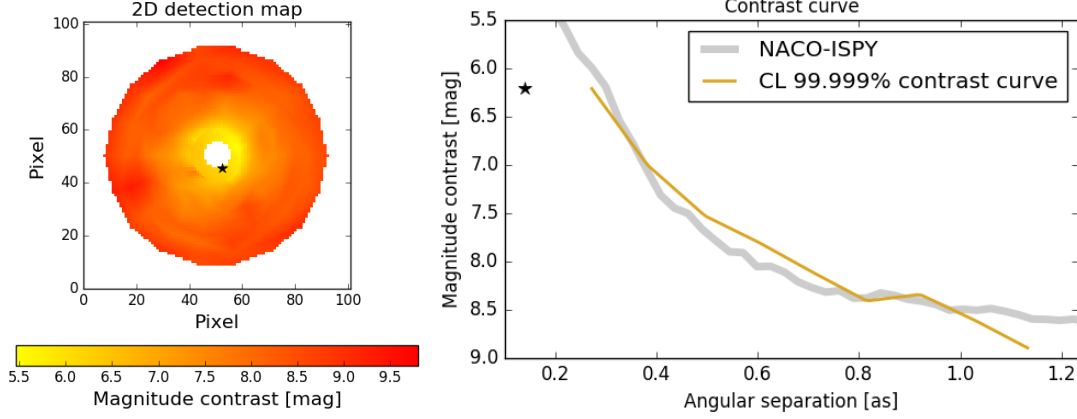


Figure 11: *Left:* two-dimensional map of the surrounding of HD34282, showing the brightness in the L' band that a planet should have at each position to be observed. *Right:* contrast curve showing the radial profile of the mean brightness required from a planet to be observed at a given distance. In both figures the black star represents candidate HD34282b.

presence of the strong signal, and therefore only limits at larger separations have been calculated. Both panels of the figure show that limits have a difference of ~ 3.5 mag between the innermost and the outermost region. For this dataset, there is no important difference between the contrast limits reached by this work and the ones obtained by the NACO-IPSY consortium. Considering the GAIA distance, at $0.4''$ the thermal emission of $\sim 88 M_J$ object should be visible, while the value recovered at $0.8''$ corresponds to a mass of $\sim 26 M_J$.

4.3 HD101412

4.3.1 Presence of a planet

The *PynPointed* images of HD101412 show two very strong signals. Candidate HD101412b is located in the south eastern part of the image, clearly distinguishable from any PSF residual. Candidate HD101412c is visible southern from the central star, in the innermost part of the image.

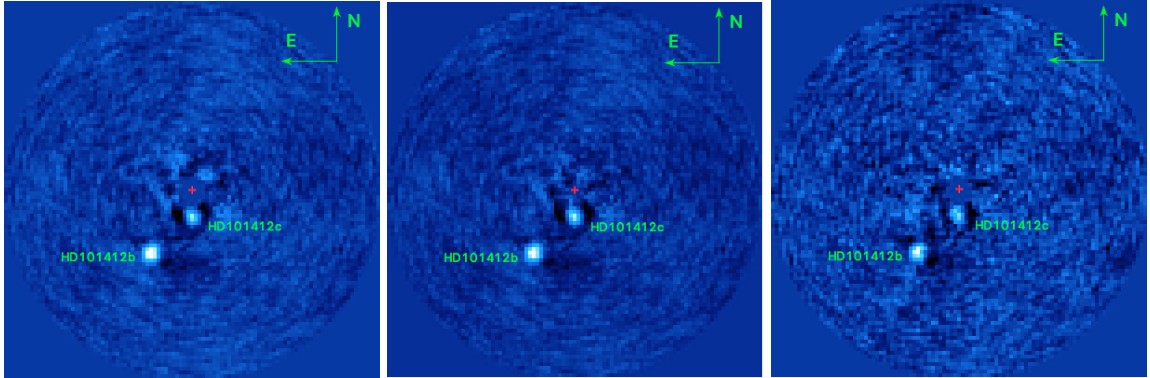


Figure 12: Two signals are present in the surroundings of HD101412, represented by a red cross. *Left:* result of the entire datacube with central mask of 4 pixels in radius after the subtraction of 17 PCs. *Center:* residual image obtained applying a mask of 2 pixels in radius and removing 15 PCs. *Right:* post processed image when considering only the first half of the $stack = 2$ datacube. In this case a mask of radius = 4 pix has been used and only 13 components were subtracted.

Both signals have been investigated with different tests. Two values for the radius of the central mask (2 and 4 pixels) were used on datacubes obtained after having stacked 5 and 2 images, as well as on the entire datacube. In every case the signals were strong and visible over a large range of principal components, 5-50 PCs for HD101412b and 5-28 PCs for HD101412c .

Successively, a randomly selected subset of the $stack=2$ datacube has been chosen, containing half of the total frames. Even when only part of the dataset was considered, the two signals were recognizable for different amounts of subtracted principal components. Finally, I repeated the whole analysis with only the first half of the .fits files: for both the mask sizes in the $stack=2$ datacube the sources were well visible. It has to be noticed that the innermost candidate is laying a few pixels away from the peak of the donut resulting from the AGPM coronagraph.

The left and central panels of Fig. 12 show the signals after the subtraction of 17 and 15 principal components when the entire datacube is used for both the mask values, 4 pixels in radius (left) and 2 pixels in radius (center). The right panel shows the image when only the first half of the $stack=2$ datacube was used to feed the *PynPoint* package and 13 principal components were subtracted. In this last case a

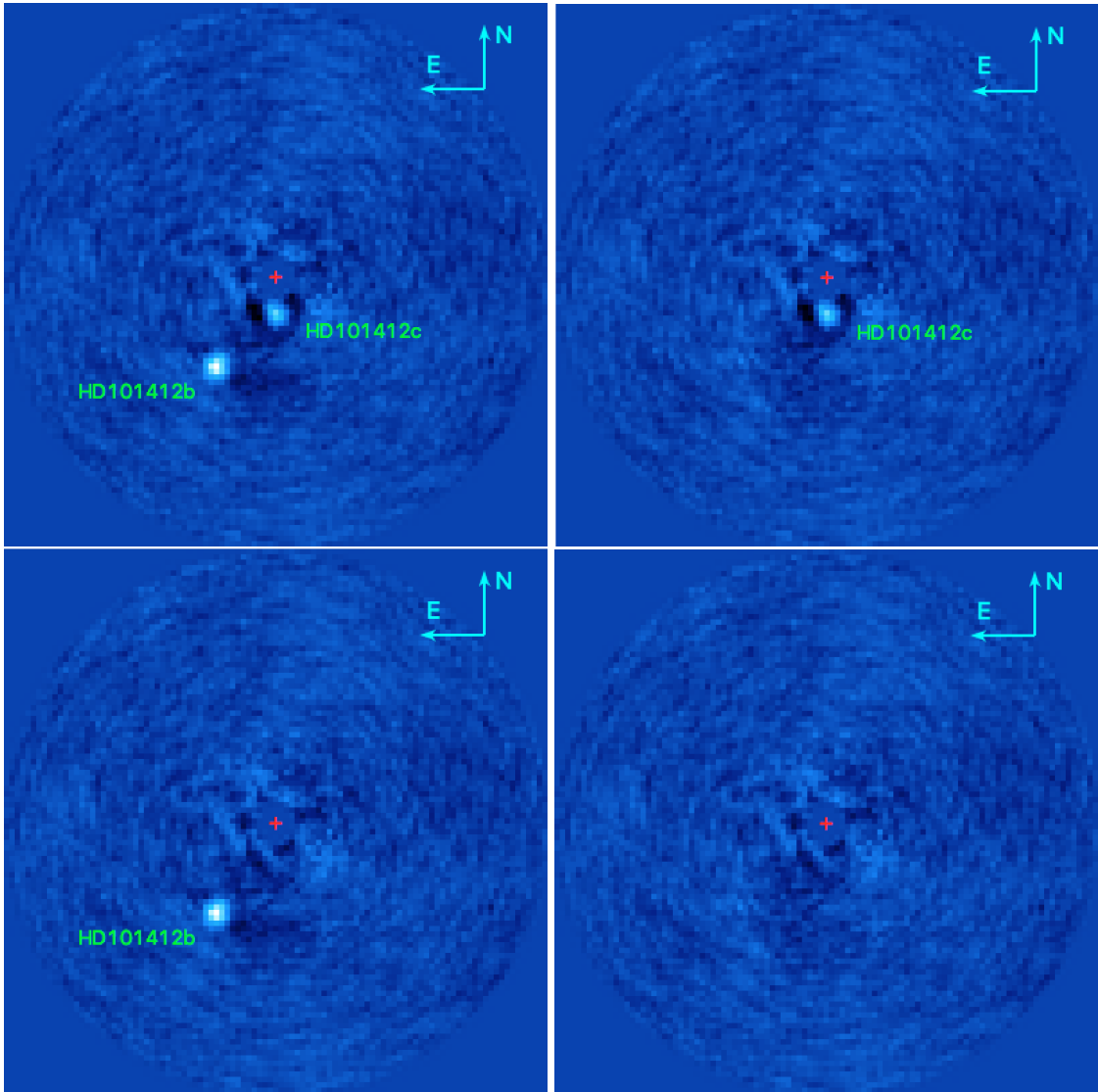


Figure 13: All the plots show the result of the *PynPoint* process when the entire datacube was used with a central mask of radius=4 pix and 15 PCs were subtracted. The red cross represents the location of the central star. *Top left:* original residual image, where both the signals are visible. *Top right:* HD101412b has been removed inserting a negative fake planet with magnitude 13.7 mag at the distance of 0.563'' and at the position angle of 147.2°. *Bottom left:* the signal of the innermost companion candidate, HD101412c, has been removed after the injection of a signal 13.3 mag bright, at 0.190'' in the direction 178.8° with respect to the direction of north. *Bottom right:* Residual image after both the signals have been subtracted inserting the artificial planets. No residuals are visible.

Table 4: Properties of the central stars HD101412 and of the two companion candidates HD101412b and HD101412c, considering a disk with $i = (30 \pm 6)^\circ$.

| Object | Property | GAIA | Maaskant et al. (2015) |
|-----------|-----------------------------------|---------------------------|------------------------|
| HD101412 | Apparent mag [mag] | 5.8 ± 0.1 | 5.8 ± 0.1 |
| | Absolute magnitude [mag] | -2.5 ± 0.3 | 0.4 ± 0.3 |
| | Distance [pc] | 440.5 ± 56.3 | 118 ± 15 |
| HD101412b | Apparent magnitude [mag] | 13.7 ± 0.3 | 13.7 ± 0.3 |
| | Absolute magnitude [mag] | 5.4 ± 0.4 | 8.3 ± 0.4 |
| | Mass [M_J] | $58.4^{+22.7}_{-11.2}$ | $7.8^{+5.8}_{-2.3}$ |
| | Projected angular separation [as] | 0.563 ± 0.007 | 0.563 ± 0.007 |
| | projected spatial separation [AU] | 248.0 ± 31.8 | 66.5 ± 8.5 |
| | Position angle [$^\circ$] | 147.2 ± 0.8 | 147.2 ± 0.8 |
| | Physical distance [AU] | $275^{+74.4}_{-62.2}$ | $73.9^{+19.9}_{-16.7}$ |
| | Period [yr] | $2\,655^{+937}_{-1\,107}$ | 368^{+130}_{-153} |
| HD101412c | Apparent magnitude [mag] | 13.3 ± 0.3 | 13.3 ± 0.3 |
| | Absolute magnitude [mag] | 5.1 ± 0.4 | 8.0 ± 0.4 |
| | Mass [M_J] | $73.6^{+28.0}_{-22.2}$ | $9.7^{+7.3}_{-2.8}$ |
| | Projected angular separation [as] | 0.190 ± 0.007 | 0.190 ± 0.007 |
| | Projected spatial separation [AU] | 83.7 ± 11.1 | 22.4 ± 3.0 |
| | Position angle [$^\circ$] | 178.8 ± 2.3 | 178.8 ± 2.3 |
| | Physical distance [AU] | $96.6^{+24.5}_{-26.6}$ | $25.9^{+6.5}_{-7.1}$ |
| | Period [yr] | 551^{+217}_{-234} | $76.4^{+32.3}_{-29.8}$ |

mask of 4 pixels in radius was applied.

The FPF values for the images presented in Fig. 12 of candidate HD101412b were, in the order from left to right, 7.8×10^{-16} , 1.1×10^{-15} and 3.6×10^{-12} , while the S/N ratios were respectively 41.3, 41.0 and 24.3. Since HD101412c is much closer to the central star, its FPF values were lower; on one side this is because of the much reduced number of reference apertures (Mawet et al., 2014), on the other side because in the central region there were still some PSF residuals, which made more difficult to sample only the background and broadened the underlying distribution. The FPF values were 0.00098, 7.2×10^{-6} and 0.0012, while the S/N ratios were 11.5, 17.5 and 11.0.

Table 4 reports the information recovered using the HesseMatrix algorithm on the HD101412 data for two distances: the result from the GAIA parallax and 118 pc (Maaskant et al., 2015). In the last case an error of 15 pc was arbitrarily assigned. The two sources (HD101412b and HD101412c) have been found at a distance of $(0.563 \pm 0.007)''$ and $(0.190 \pm 0.007)''$ respectively, with a position angle of $(147.2 \pm 0.8)^\circ$ and $(178.8 \pm 2.3)^\circ$. The contrasts that have been estimated are 7.9 ± 0.2 mag for HD101412b and 7.6 ± 0.2 mag for HD101412c. The result of the subtractions of the signals is shown in Fig. 13: the upper left image shows the original residual; the upper right and lower left images show the surrounding of HD101412, whose position is marked with a red plus, after the removal of HD101412b and of HD101412c respectively. Finally, the lower right image shows the result of the removal of both signals.

I estimated the mass of the companion candidates using the COND models from Baraffe et al. (2003) and reported it in Tab. 4. The steps described in Section 3.4 have been used and the age from Folsom et al. (2012) was assumed. I changed the lower error to be 0.2 instead of 0.7, because the COND models were not able to interpolate ages lower than 1 Myr.

If one considered the age from Fairlamb et al. (2015), and a distance of 440 pc the estimated mass values would have been even larger: $\sim 148 M_J$ and $\sim 186 M_J$ for HD101412b and HD101412c respectively. Assuming the distance from Maaskant et al. (2015) of 118 pc, the masses would have been $7.9^{+4.7}_{-1.8} M_J$ and $9.7^{+5.8}_{-2.3} M_J$ respectively, assuming they were planetary non accreting companions. These values are

of extreme interest, since masses $< 10 M_J$ strongly support the planetary scenario.

For the calculation of the physical separation between the star and its companions, I considered both the disk orientations from van der Plas et al. (2008) and from van der Plas et al. (2015). In a first phase I considered the inclination value proposed by van der Plas et al. (2008), $i = (30 \pm 6)^\circ$. Since no position angle was suggested, I adopted the value of 90° . The uncertainties on the physical separation expressed their maximal and minimal values when 17 different position angles between 10° and 170° were considered, one every 10° , spanning the whole range of possible outcomes when considering other PAs. For the values on the orbital period reported in Tab. 4 the mass of the central star calculated by Folsom et al. (2012) was chosen. The values are reported in Tab. 4. If the smaller distance is confirmed, two companions at $a < 100$ AU could be detected around HD101412, which makes this Herbig Ae/Be extremely interesting for follow-up observations.

In a second phase I considered the inclination angle $i = 80^\circ$, which implied a very tilted disk resulting in an extreme increase of the separation value: the image projection was not able to show the huge separations between star and companions. Errors do not include the uncertainty in the inclination angle, which would have led to huge errorbars, since the disk would have been almost edge on.

The results adopting the GAIA distance were 311_{-91}^{+104} AU for HD101412c and 1351_{-234}^{+238} AU for HD101412b. The vicinity of course got reflected on the orbital periods which are ~ 3188 yr and $\sim 28\,808$ yr respectively. Considering the case where the distance of HD101412 is much closer to the Solar System, as found by Maaskant et al. (2015), the de-projected distances between the star and the companion candidates appear to be $362.2_{-62.6}^{+63.6}$ AU for HD101412b and $83.5_{-24.3}^{+27.9}$ AU for HD101412c. Those values led to orbital periods of the order of ~ 3997 yr and ~ 442 yr, respectively.

4.3.2 Detection limits

The presence of the source called HD101412b is visible not only in the post-processed image (see Fig. 12), but also in the final contrast curve and in the detection map. Figure 14 shows the two-dimensional detection map of HD101412. A clear ring at a distance of ~ 20 pixels from the center is visible and highlighted by the dotted black circle. At that distance the algorithm had to insert brighter planets (represented in yellow) in order to reach FPF values below the threshold given by the 99.999% CL. HD101412b broadened the underlying distribution, increasing the probability of a False detection for any other signal at the same distance. This phenomenon can be used to investigate specific regions of circumstellar disks, as done in the case of TW Hya (see Section 4.5.1). The map has been obtained analyzing 63 positions of the $stack = 20$ datacube, applying a mask of 4 pixels in radius and subtracting at each step 20 PCs.

It has to be noted that if the disk inclination given in van der Plas et al. (2015) was correct, most of the locations investigated and showed in the map would be meaningless, since in the projection they would correspond to positions outside the boundaries of the disk or at very large distances from the central star.

Figure 15 shows two curves which differ for the used dataset: the green curve considers the original dataset, with the two companion candidates hidden in the frames, while the violet curve considers the same dataset after the removal of both the signals. The latter curve has been taken from the azimuthal average of the values used to plot Fig. 14. For the violet curve, 162 positions have been analyzed and their maximal magnitude values at every distance from the center averaged in order to create the contrast curve.

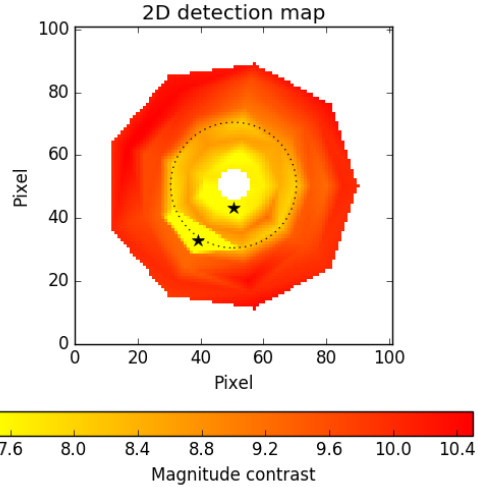


Figure 14: 2-dimensional detection map of the surrounding of HD101412. The black stars represent the two companion candidates described in the previous section. The dotted circle indicates the position of the ring-shaped structure of the detection limit due to the presence of HD101412b.

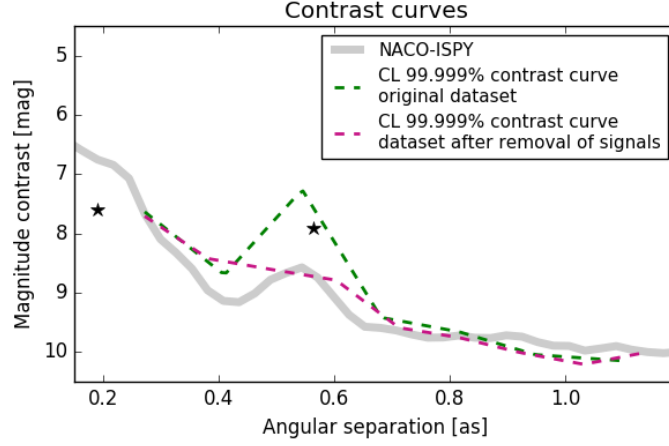


Figure 15: Contrast curve of the surrounding of HD101412 when the original dataset (green dashed line) and the one without the signals (violet dashed curve) have been investigated. The grey line represents the limits recovered by the NACO-ISPY consortium, while black stars represent the values of distances and contrasts of the two detected signals.

From Fig. 15, two conclusions can be drawn: first of all, there is strong evidence that the bump in the green curve is due to the presence of HD101412b, since the curves are different when the dataset without point sources is used. Furthermore, the magnitude of the planet in the L' band at separations larger than $0.8''$ needs to be at most 16.8 mag to be seen. This limit is very similar to the one recovered by the NACO-ISPY consortium and correspond to a mass of $\sim 1.3 M_J$ assuming the system to be 118 pc away, and a mass of $\sim 6.4 M_J$ assuming a distance of 440 pc.

4.4 HD179218

4.4.1 Planet detection

The surroundings of HD179218 were accurately analyzed, since at least two possible sources (HD179218b and HD179218c) were detected. Many tests have been done to confirm the detections, but it is still not clear if they are actually associated to physical sources or if they are PSF residuals, extended disk emissions or even artifacts of the analysis process.

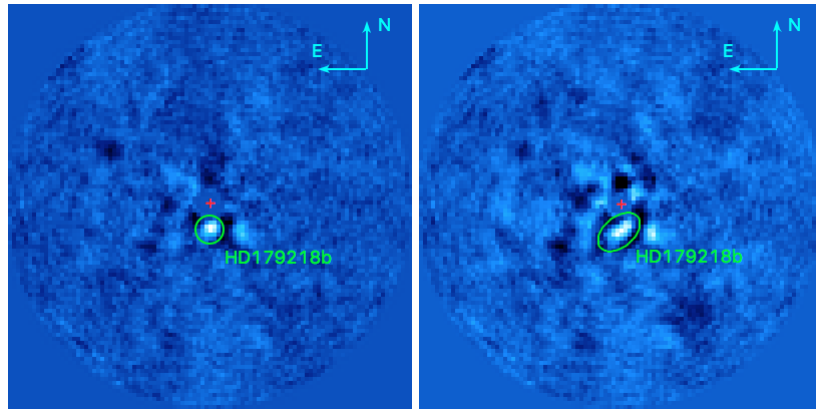


Figure 16: *Left:* residual image using the $stack = 10$, datacube when a mask of 4 pixels in radius is applied in the center and 19 PSF components have been removed. A potential point source can be distinguished south from the star. *Right:* final image when the whole dataset is used and a mask of radius 3 pixels is applied before the subtraction of 21 PCs. In this case, the source is unlikely classified as a point source, but seems rather to be due to an elongated source.

HD179218b was detected in the $stack = 10$ datacube after the removal of 9-31 PC, in the southern region with respect to the star. The signal is strong, but, depending on the number of subtracted components, either it seems to be produced by a point source, as in the left panel of Fig. 16, or to be extended and to have a curved shape, as in the right panel of the Fig. 16.

I checked if the signal was present in other situations, and it turned out that it can be recovered in the images obtained with $stack = 1, 2, 5, 10$, mask radius = 3, 5 pixels, PC 9-30. Even if the source is always there, three facts support the idea that it does not come from a physical signal due to a planet: (1) it does not seem to be due to a point source; (2) it is possible, since often its shape is elongated, that HD179218b is actually a post-process disk emission, as many residuals from the disk are visible in the images close to the center; and (3) the signal seems to be located at different positions. The last point can be observed comparing the left panel of Fig. 16 with the left panel of Fig. 17, where the green circle is placed at exactly the same position in the image, but the signal clearly covers two different areas.

The FPF has been calculated in the situations described before. The lower value has been recovered thanks to the subtraction of 17 PCs to the $stack = 5$ datacube, applying a mask of 3 pixels in radius, and resulted in a value of 0.00019, to which corresponded a signal to noise ratio of 7.1. For most of the other situations, the FPF values were of order $\sim 10^{-2}$. Obtaining a lower False Probability Fraction is difficult because the regions at the same separation from the star are contaminated by disk and PSF residuals, and the signal is not always stronger, as it can be seen in the left panel of Fig. 17.

I tried to estimate the distance of the signal from the central star and its contrast with the HesseMatrix

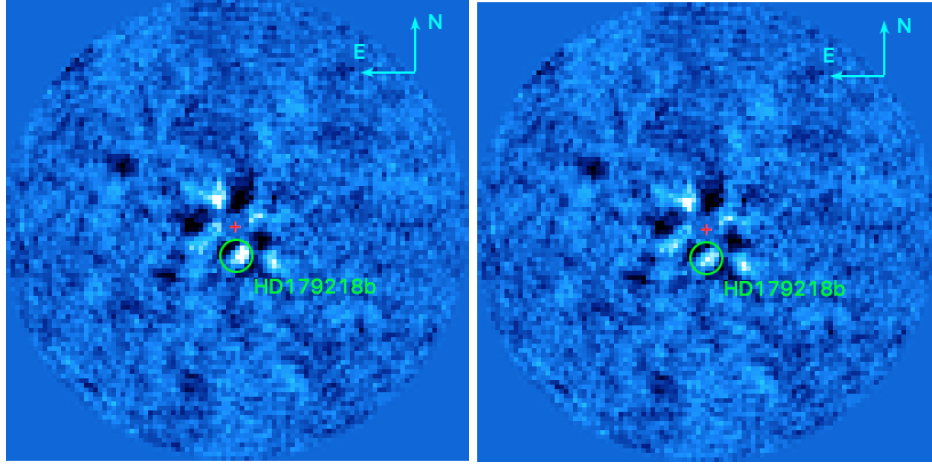


Figure 17: *Left:* original image used for the HesseMatrix algorithm, created using the $stack = 10$ datacube, with a mask of 3 pixels in radius and subtracting 21 PCs. The green circle represents the same area highlighted in Fig. 16; in this situation the source is not in its center, but it appears to be shifted in the north western direction with respect to the previous position. *Right:* Residual image after the HesseMatrix optimization. The ROI has the flatter possible surface, but the signal has not been completely subtracted.

algorithm, but, as it can be seen in Fig. 17, the result still contained residuals and the signal was not completely subtracted. It is likely that the algorithm could not properly remove the signal because it was not due to a clean point source, and therefore its subtraction could not produce a flat surface.

The optimization algorithm found the source to be located at a distance of $(0.129 \pm 0.006)''$, creating an angle of $(189.5 \pm 2.7)^\circ$ with the north direction. The contrast in the L' band was estimated to be 7.5 ± 0.2 mag, but, as it can be seen in Fig. 17, it is not enough to properly and completely subtract the signal. For the investigation, the $stack = 10$ datacube was used, with $subpix = 5$, ROI side = 8 pixels, mask radius = 3 pixels and PC = 21.

The points at the distance recovered by the HesseMatrix algorithm laid on the donut produced by the subtraction of the background, when also the AGPM is subtracted, producing a hole in the very center of the still rotated images. The fact that the recovered source layed on it made difficult to claim that HD179218b is a signal due to a spatially separated point source and not to a residual of the star light.

The *PynPointed* images of HD179218 showed another signal in the south western region with respect to the center, as shown in Fig. 18. The source could be detected in many datacubes ($stack = 1, 2, 5, 10$) using different values for the mask size (radius of 3, 5 pixels) and a wide range of consecutive principal components (45 – 55). I also looked at the results obtained with only half of the starting dataset, in the case $stack = 2$. The signal is still faint, but it can be seen in a very similar range of consecutive components ($\sim 43 - 55$ PCs).

After the tests I conducted, I concluded that HD179218c could be a planet, even if its detection is statistically uncertain. Indeed, the FPF values were of order $10^{-3} - 10^{-2}$ using an aperture radius of 2.0 pixels, and to them corresponded a signal to noise ratio of ~ 6.5 . The values correspond only to a CL of $\sim 99.5\%$, but the appearance of the bright spot in many situations encouraged a further consideration of the signal. The fact the the FPF values were still quite high is mainly due to the weakness of the signal, which is never strong enough to reach small FPF values.

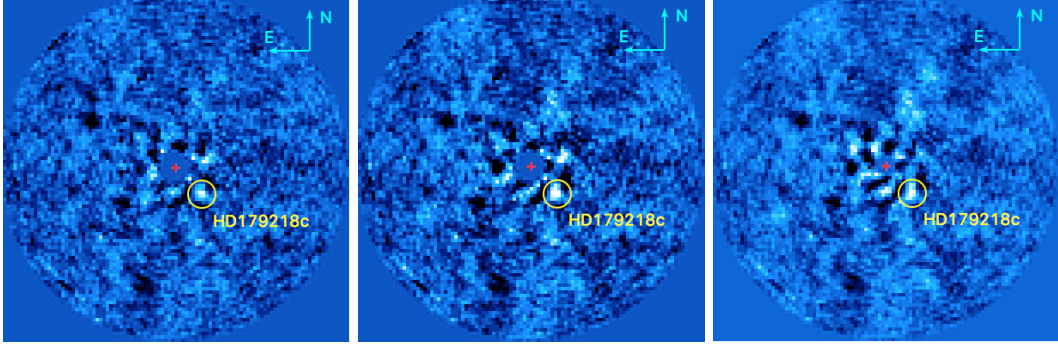


Figure 18: Three images reporting the environment around HD179218 are shown. *Left:* the result of the process of the $stack = 5$ dataset with a central mask of 5 pixels in radius after the subtraction of 37 PC is imaged. *Center:* similar image with different parameters. In this specific case they are $\{stack, \text{central mask}, PC\} = \{2, 5, 42\}$. *Right:* the signal is present also using the whole dataset, with $\{mask, PC\} = \{3, 44\}$.

I proceeded with the characterization of the source. The AstroPhoto routine has been used on the $stack = 5$ dataset, using $subpix = 10$, a mask with a radius of 3 pixels and 47 components of the PSF were subtracted. The FPF reaches its maximum of 0.474 when a fake negative planet is inserted with magnitude contrast of $8.6^{+0.4}_{-0.7}$ mag, at $0.237 \pm 0.003''$ from the center and with an angle of $221.7 \pm 0.7^\circ$ from the north. Looking at the images, it seems that the signal has been slightly oversubtracted. This is because maximizing the FPF of the signal aperture makes it as similar as possible to the other apertures at the same distance. If those have negative values, the algorithm also looks for a subtraction leading to a similar value. As a consequence, the real magnitude contrast could be slightly higher.

Successively, I also performed the analysis of HD179218c with the HesseMatrix algorithm, removing the signal with the same conditions as for the AstroPhoto analysis, except for the $subpix$ parameter which was set to be 5. The routine identified a signal with a contrast magnitude of 9.9 ± 0.2 mag, at $(0.275 \pm 0.008)''$ from the star with a position angle of $(216.0 \pm 1.6)^\circ$. It seems that the signal has not been subtracted at its best, and some residuals remained in the post-processed frames. It has therefore to be kept in mind that the brightness of the object could be larger than the one estimated from the

Table 5: Properties of HD179218 and of its candidate companion for the study performed with the HesseMatrix algorithm. The GAIA parallax measurements have been assumed.

| Object | Property | GAIA |
|-----------|-----------------------------------|---------------------------|
| HD179218 | Apparent Brightness (mag) | 4.5 ± 0.1 |
| | Distance (pc) | 293.1 ± 30.1 |
| | Absolute Brightness (mag) | -2.8 ± 0.2 |
| HD179218b | Apparent Brightness (mag) | 14.4 ± 0.3 |
| | Absolute Brightness (mag) | 7.1 ± 0.3 |
| | Mass (M_J) | $18.3^{+12.1}_{-4.7}$ |
| | Angular Projected Separation (as) | 0.275 ± 0.008 |
| | Projected Separation (AU) | 80.6 ± 8.7 |
| | Position Angle ($^\circ$) | 216.0 ± 1.6 |
| | Physical Separation (AU) | $85.3^{+18.9}_{-14.7}$ |
| | Orbital Period (yr) | $413.6^{+142.6}_{-117.8}$ |

minimization of the curvature. The distribution functions of the parameters did not really overlap, and I decided to consider for the next analysis the values obtained from the second algorithm.

Since the distances measured by the Hipparcos and the GAIA mission are similar and almost agreed, I considered only the GAIA value. It should be remembered that, according to the Hipparcos data, all the values are slightly smaller, since the object is supposed to be closer. Table 5 shows the parameter values assuming the disk orientation given in Fedele et al. (2008), the mass of the central star from Alecian et al. (2013) and the photometric and astrometric value from the HesseMatrix algorithm. The age was assumed to be $1.1^{+0.44}_{-0.1}$ Myr because the COND models were not able to interpolate at values lower than 1 Myr, but for lower ages the lower mass error could be even larger, leading to lighter planets.

4.4.2 Detection Limits

Finally, I investigated the detection limits of HD179218 considering the $stack = 25$ datacube and the removal of 22 principal components at each image generation. The pipeline is able to detect planets with brightnesses in the L' band of ~ 14.5 mag at separations larger than $0.6''$. Both the signals described in the previous section are drawn with a black star. On the left panel of Fig. 19 they are located at the position they have been observed on the sky plane, while on the right panel their contrast can be compared to the CL 99.999% detection limits at that separation from the star.

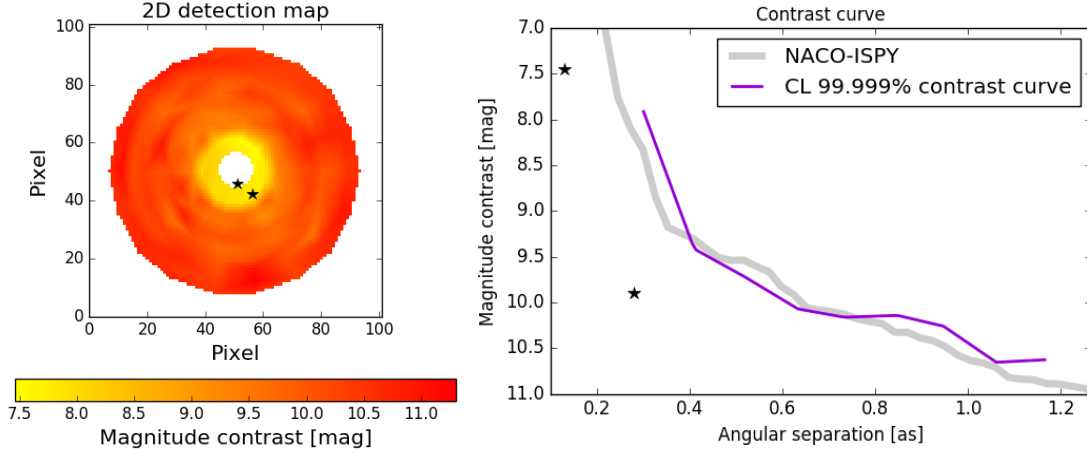


Figure 19: *Left:* 2D sensitivity map of the surroundings of HD179218. Hotter colors represent lower magnitude contrast. *Right:* detected contrast curve after the consideration of 162 positions. As one may see the reached limits are very similar to the one obtained by the NACO-IPSY consortium. In both panels stars represent the position and the contrast of the previously discussed signals.

4.5 TW Hydrae

4.5.1 Detection limits

The search for planets around TW Hya did not highlight any signal in the data. The $stack = 1, 2, 5, 10$ datacubes have been examined for two sizes of central mask, 2 and 4 pixels in radius, and a wide range of PCs, from 5 to 60 in step of three. In none of the cases a particular bright point source was visible and I therefore proceeded with the investigation of the detection limits.

The map and the curve have been produced considering 162 positions: the angular step has been set to 20° and the radial step to 4 pixels. 20 PCs have been subtracted from the $stack = 20$ datacube, with a central mask of 4 pixels in radius. The left side of Fig. 20 shows the detection limits within a Confidence Level of 99.999% of the surrounding region of TW Hya. In the outer region of the image, planets 5 magnitudes fainter can be observed, reaching the limit of ~ 16 mag. The circumstellar disk of TW Hya is almost pole on, since the inclination angle is $(7 \pm 1)^\circ$ (Qi et al., 2004). Therefore the map shows the actual detection limits on the whole disk. If it was edge on, most of the image locations analyzed by the algorithm would not have investigated disk regions and would have been uninteresting, since planets are

expected to form from the circumstellar material. On the map the positions of the gaps at 22, 37 and 43 AU recovered by the observations of Andrews et al. (2016) are also shown, assuming that the disk is perfectly pole on. Those regions of the *Pynpointed* images were accurately investigated during the search for planets, but no companion signal has been detected.

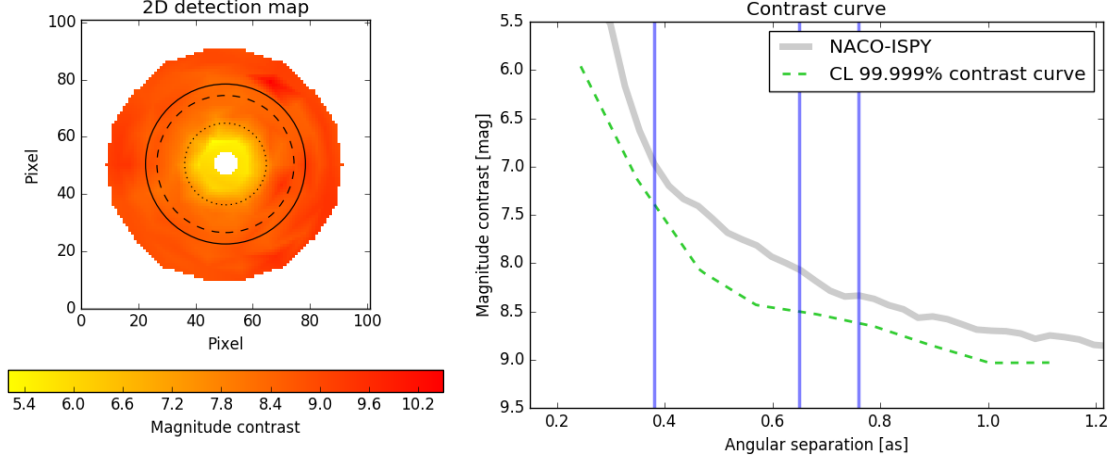


Figure 20: *Left:* two-dimensional map of the detection limits of TW Hya. Brighter colors (yellow) stand for lower detection limits, since brighter planets had to be inserted to be detected. Darker colors (red) characterize regions where fainter planets can be observed and the detection limits are higher. The circles represent the gaps in the $870\ \mu\text{m}$ luminosity profile at 22 AU (dotted line), 37 AU (dashed line), 43 AU (solid line), assuming the disk is completely face on. *Right:* contrast curve (dashed green line) of TW Hya subtracting 20 principal components compared with the detection limits obtained from the NACO-IPSY database. The blue vertical lines show the positions of the gaps previously plotted with the black circles.

The right plot of Fig. 20 shows the contrast curve and the blue lines highlight the ring substructures of the TW Hya disk. The presence of any non removed physical signal could potentially be visible as a bump in the contrast curve (see Section 4.3.2). A bright signal broadens the underlying aperture distribution increasing the FPF value at any position other than the signal one. As a consequence, to reach a value lower than the FPF threshold at the same distance of a point source, one has to insert brighter planets, and the azimuthally averaged contrast curve shows a bump. The absence of kicks confirms the absence of companions, in particular at the gap radii. The right plot of Fig. 20 shows the contrast curve and the blue lines highlight the ring substructure positions of the TW Hya disk. The presence of every non removed physical signal could potentially be visible as a bump in the contrast curve (see Section 4.3.2). A bright signal broadens the underlying aperture distribution increasing the FPF value at any position other than the signal one. As a consequence, to reach a value lower than the FPF threshold at the same distance of a point source, one has to insert brighter planets, and the azimuthally averaged contrast curve shows a bump. The absence of kicks confirms the absence of companions, in particular at the gap radii.

The curve is not able to reach the region with very small angular separation from the center, because very bright planets need to be inserted, causing the PSF subtraction to be dominated by them and the signals to get immediately subtracted. Therefore very bright objects can not be detected close to the center. To solve the problem, one could subtract fewer PCs at each step, but then other regions of the

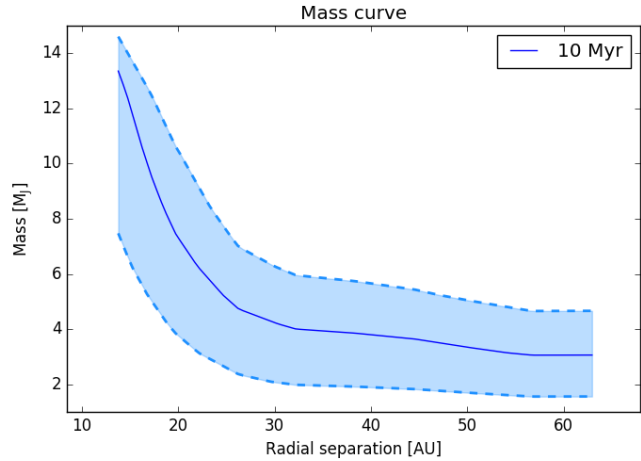


Figure 21: The detection limits in terms of contrast magnitude have been translated as mass values according to the OCND model (solid dark blue line) for an age of 10 Myr. The colored area represents the uncertainty for the errors in the age measurement given by Barrado Y Navascués (2006).

image would be influenced and would have higher detection limits.

Figure 21 shows the mass value associated to the previously described contrast limits. For the calculation the distance measured by the Hipparcos mission has been chosen and the age of 10^{+10}_{-7} Myr from Barrado Y Navascués (2006) was assumed. From ~ 30 AU, the plot rejects the presence of a planet heavier than $4 M_J$, while at smaller separations (~ 15 AU) only planets up to $14 M_J$ could potentially orbit TW Hya according to the COND model. Considering that forming planets may be accreting from the circumplanetary disk, these values could be even lower.

4.6 HD97048

4.6.1 Detection Limits

HD97048 data have been investigated using different settings: for every *stack* number in the set $\{5, 10, 25, 50, 100\}$, I applied three masks of different radii of 3, 5 and 10 pixels to the 101×101 pixels dataset of 27300 images. I then focused on the mean residuals of the subtraction of a varying amount of components between 3 and 30 and between 30 and 80 in step of 5. No signal appeared clearly and persistently in different situations at the same position and, given all the information listed Section 2.3.6, it became important to calculate the detection limits to understand the objects that can be excluded to orbit HD97048 and the ones that could have been missed.

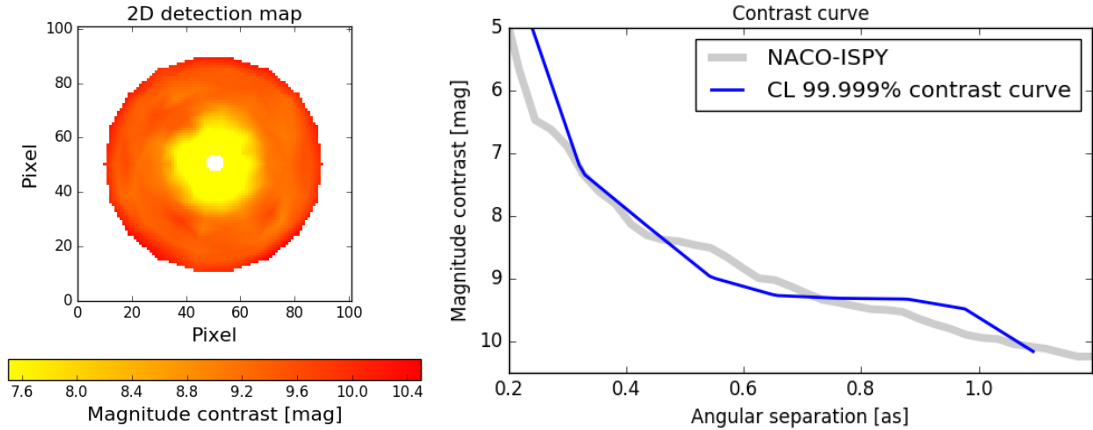


Figure 22: Two dimensional map and final contrast curve of HD97048, when considering 162 positions around the central star. The map shows the detection limits in the case 35 PC have been subtracted.

Figure 22 shows the detection limits of HD97048 when 162 positions were considered to investigate the *stack*=25 datacube. When the radial distance is $0.5''$, a contrast of ~ 9 mag can be reached, while at separations larger than $1.0''$ even a contrast higher than 10 mag can be achieved. The COND models from Baraffe et al. (2003) can be used to translate the reachable contrast into a mass, resulting in a value of $\sim 20 M_J$ and $\sim 10 M_J$, respectively.

The contrast limits are very comparable to the ones from the NACO-ISPY consortium at all separations, since the largest offset in the range $0.3'' - 1.1''$ is at most 0.4 mag. Considering different numbers of subtracted components could slightly lower the curve, but the difference would be minimal and would not considerably change the limits one can reach.

4.7 HD141569

4.7.1 Detection Limits

I ran *PynPoint* on the HD141569 data using different starting datacubes ($stack = 100, 50, 25, 10, 5, 2$) and different mask sizes (radius=2, 4 pixels) for a varying number of PCs (3–50 in step of three): no strong and robust signal in the neighborhood of the star was detected for an interval of consecutive PCs in the range from 3 to 50. Particular attention was paid at the position where Mawet et al. (2017) found a potential faint source with a very low signal to noise ratio ($D \approx 38$ AU, position angle $\approx 70^\circ$). In none of the residual images a feature or even a faint suspected point source has been observed.

I investigated the sensitivity achieved to clarify the presence of any possible unseen companion. As usual, 162 positions were selected and, in each one, a planet was inserted to see what is the required magnitude to obtain a detection within a CL of 99.999%. A central mask with radius 5 pixels was applied during every image processing of the $stack = 20$ datacube.

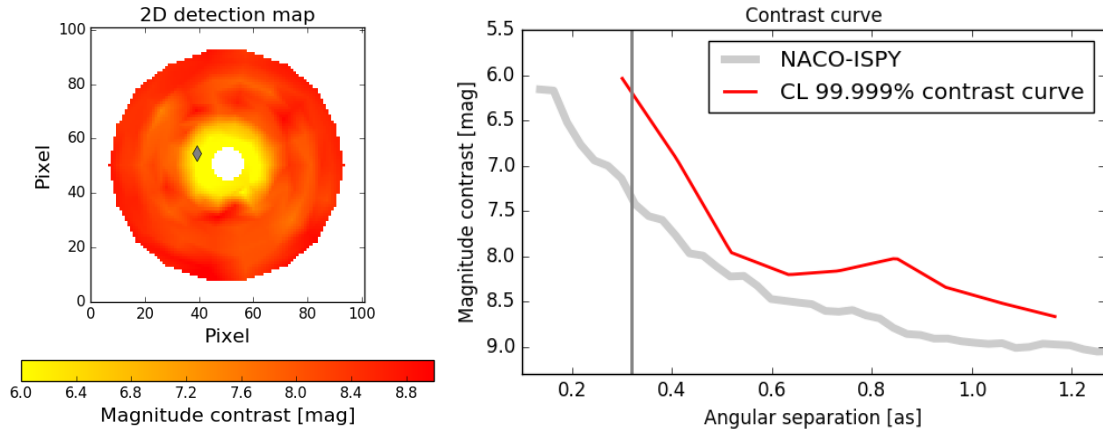


Figure 23: Sensitivity limits achieved during the analysis of HD141569 for a CL of 99.999%. The grey diamond on both panels shows the position and magnitude at which Mawet et al. (2017) detected a faint and uncertain source.

Looking at the contrast map on the left panel of Fig. 23, one could expect a point source at $\sim 0.8''$, because of the ring-shaped structure around the center, where brighter planets need to be inserted to reach a FPF lower than 5.0×10^{-6} . A bump of the azimuthal average at the same distance can be observed also on the right panel, meaning that in average artificial planets 1 mag brighter have to be inserted in order to be seen. This component is not due to a point source, but to the systematic presence in the final images of four bright spots at the four angles, which consequently caused the generation of the ringed structure and of the kick. Those speckles could be found also in the raw data and could not be avoided. The plots highlight the position of the very faint point source reported by Mawet et al. (2017) with a grey diamond. No signature of the presence of a planet is visible at that position.

5 Discussion

In this work I analyzed data of seven Herbig Ae/Be stars and found 6 companion candidates. In this section I will explain the results obtained and discuss them in relation to the planet formation mechanism. In Section 5.1 I will comment the results and suggest specific follow-up observations for some of the objects; in Section 5.2 I will summarize the results and compare them with the ones of other studies; finally, in Section 5.3 I will introduce the accretion from a circumplanetary disk to explain the very large brightnesses of the recovered signals, using HD34282b as an example.

5.1 Individual objects

5.1.1 HD259431

Two companion candidates have been found around HD259431: HD259431b and HD259431c. The signal of HD259431c can be the consequence of: (1) a residual of the HD259431b subtraction, (2) a companion point source previously hidden by the bright signal or (3) even a background object. Further studies should observe the same object again, in order to verify if candidate HD259431c is still present in the image and if its proper motion corresponds to the one of HD259431, to the one of HD259431b, or to none of them. A different motion would imply that it is a background object. If the signal is due to a fixed background star, after a given period of time the relative distance and the relative position of the two signals (star and companion candidate) are expected to be different, because of the proper motion of HD259431. In order to distinguish every background object, I estimated the time required to be able to observe a shift of 2 pixels. The angular velocities of HD259431 with respect to the background sky in the two directions are

$$\begin{aligned}\mu_{RA}^G &= -2.38 \pm 0.09 \text{ mas/yr} & \mu_{DEC}^G &= -3.02 \pm 0.07 \text{ mas/yr} \\ \mu_{RA}^H &= -3.33 \pm 1.24 \text{ mas/yr} & \mu_{DEC}^H &= -3.23 \pm 1.00 \text{ mas/yr},\end{aligned}$$

where G stands for GAIA and H for Hipparcos. Assuming that the two companion candidates are both background objects and therefore do not follow the proper motion of HD259431, these velocities imply

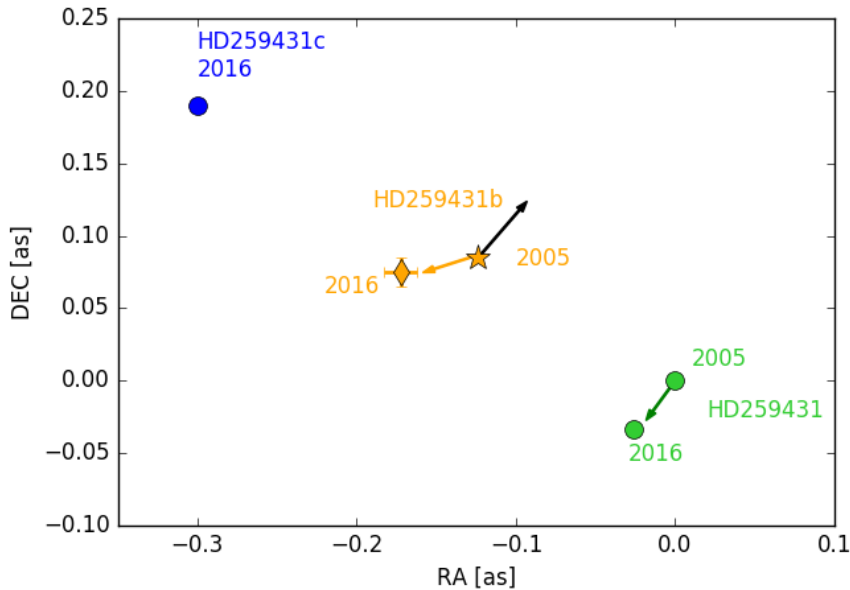


Figure 24: Proper motion of HD259431 and its companion candidates. The relative positions of the star after 11 years according to the GAIA proper motion are shown in green. The positions of the companion HD259431b relative to each observation are plotted in orange. The black arrow represents the expected direction of the relative motion, assuming the source to be a background star. The blue circle represents HD259431c, the second candidate companion detected only in the 2016 data.

that, in order to be able to observe a shift of 2 pixels (~ 54.38 mas) in the companion positions, the observation should be repeated after 11.7 yr according to the Hipparcos measurements and after 14.1 yr according to the GAIA ones.

Figure 24 illustrates the proper motion of the central star and compares the relative position of the nearest candidate. The green circles show the path followed by the star from 2005, when Thomas et al. (2007) observed it, to 2016, when it was observed during the ISPY survey, according to its proper motion from the GAIA archive. The orange star represents the companion measurement by Thomas et al. (2007) relative to HD259431. The orange diamond represents the relative position recovered in 2015, considering the shift of the star due to its proper motion. If HD259431b were a fixed background star, its motion between the observations should have followed approximately the direction of the black arrow. This is clearly not the case, since the second detection has approximately followed the direction of the star and its proper motion, thus that the source is a companion.

Assuming the Hipparcos orbital period given in Tab. 2, the angular velocity of the orbital motion of HD259431b can be evaluated and a rough estimation of the projected position of the companion at the time of the first observation can be made. The calculation justified the difference between the directions of the green and the orange arrows of Fig. 24, concluding that it can be explained through the orbital motion of HD259431b. More precise information about the disk orientation are required for a more precise calculation, but it is possible that the difference in the position angle and in the distance measure between the work of Thomas et al. (2007) and this Master Thesis are due to the orbital motion of the companion HD259431b ($0.15''$ and $(0.182 \pm 0.006)''$, 55.6° and $(53.5 \pm 1.9)^\circ$). According to the available data, there is strong support to the hypothesis of HD259431b to be a companion of HD259431. Its brightness in the L' band suggests it to be a stellar object, but it should be kept in mind that accretion processes from circumplanetary disks might make the formation of giant planets extremely bright. I will analyze this possibility in Section 5.3.

In summary, two companion candidates to HD259431 have been detected. Further analyses are required to confirm unequivocally the common proper motion, but according to the detection of Thomas et al. (2007) it seems that HD259431b is a true - probably stellar - companion to HD259431.

HD259431c detection needs a confirmation, since it could be an artifact due to the subtraction of HD259431b. According to the chosen disk orientation, HD259431c could be considered a planet only in case the Hipparcos distance gets confirmed, otherwise it would lay too faraway from the central star.

Another possibility to consider is the case when the proper motion study confirms that the signal comes from a physical source: HD259431c could be a companion of HD259431b, which would imply that the separation from its orbital center is much smaller, ~ 54 AU and ~ 113 AU according to the Hipparcos and GAIA distances respectively. In case the triple system scenario gets confirmed, only the study of the orbital motion of HD259431c will conclude if it is a planet and which object it is orbiting around. The wide range of possible explanations of the system HD259431 accentuates the necessity of follow-up observations, not only to confirm the presence of three sources, but also to allow a first SED approximation, gaining information about temperature and color of the objects.

5.1.2 HD34282

In the vicinity of the Herbig Ae/be star HD34282, a companion candidate was found. The properties of HD34282b are dominated by the huge distance uncertainty of the star from the Earth. Distances proposed by Hipparcos and GAIA differ by a factor ~ 2 . This discrepancy got reflected on the physical separation between star and companion; on the COND masses, which differ by a factor ~ 3 ; and on the period, which is up to 2.5 times larger when considering the GAIA distance. The case of HD34282b emphasizes that accurate distance measures are essential to properly characterize planets. In the next years, GAIA estimates will be more reliable thanks to the future data releases.

The proper motion of HD34282, according to the GAIA and Hipparcos missions, is given by

$$\begin{aligned} \mu_{RA}^H &= 2.30 \pm 1.31 \text{ mas/yr} & \mu_{DEC}^H &= 3.90 \pm 1.17 \text{ mas/yr} \\ \mu_{RA}^G &= 0.14 \pm 0.09 \text{ mas/yr} & \mu_{DEC}^G &= -0.93 \pm 0.08 \text{ mas/yr.} \end{aligned}$$

Using these values, I calculated when a second observation should be made in order to clarify if HD34282b is a background star, i.e. when a shift of at least 2 pixels will be measurable. Considering GAIA values for the proper motion of HD34282, one has to wait 57.8 yr to observe a difference of $0.054''$ in the relative distance and position. Hipparcos data suggest a wait of order of 12.0 years. After this period, the signal will be hidden from the star, or it could be located in a very different position with respect to the central

star. Indeed, the orbital motion, assuming the periods calculated in Section 4.2.1, causes the signal to make an angular shift of 47.2° and 81.5° for the two missions respectively.

The strong possibility that HD34282b is a true companion suggests to consider an immediate and independent follow-up observation in another band. This would be able to confirm the presence of a point source, excluding instrumental artifacts, and to first roughly characterize its SED, bringing information about temperature and emitting surface. A second observation could lead to the spectral classification of HD34282 as a planet. As it will be discussed in Section 5.3, Zhu (2015) pointed out that the SEDs of planets surrounded by accreting circumplanetary disks fall less steeply than the ones of stellar objects and brown dwarfs, resulting in redder colors. A multi-band observation of HD34282 could allow to estimate the SED shape and to exclude that HD34282b is a stellar object, supporting the planetary scenario. This picture could be confirmed only if there is evidence that the two objects have common proper motion.

Gaps are often thought to be tracers of ongoing or past planet formation processes, in which the forming planet accretes the material while orbiting the star, leaving a material lack behind. It is of particular interest the fact that, in the protoplanetary disk of HD34282, Khalafinejad et al. (2016) observed a dust density gap at 92 AU. For their study, they considered a distance of 348 pc and, adopting this distance, the separation of the companion found in this thesis is ~ 50 AU. The distances do not correspond, but planets are expected to migrate in the disks of their host star, and therefore the lack of a planet at the exact position of the gap is still an interesting fact that should be kept in mind.

In summary, the results obtained in Section 4.2.1 and the combination of signal and density gap support the hypothesis of a true companion and suggests immediate further observations.

5.1.3 HD101412

In the neighborhood of HD101412 two companion candidates have been found. However, uncertainties on the distance and on the disk orientation strongly influence their analysis. For this reason, two different disk orientations were analyzed, one from van der Plas et al. (2015) and one from van der Plas et al. (2008). The first orientation ($i = 80^\circ$) implies the disk to be almost edge on, leading to the conclusion that HD101412b does not lay in the planetary range. Indeed, its separation would be ~ 362 AU, using the closest distance from Maaskant et al. (2013). On the contrary, HD101412c, could still be classified as a planet, since its separation from the central host star is estimated to be ~ 83 AU. Using the GAIA parallax, even larger values are obtained and neither HD101412b nor HD101412c would be classified as planets, since their separations would be much larger (~ 1350 AU and ~ 310 AU respectively).

Using the second orientation suggested in van der Plas et al. (2008), the planets are placed much closer to the central star, even if the disk position angle is not known. As the disk is not edge on anymore, the separation given in the image provides a rough idea of the actual separation of the companion. Again, depending from the distance of the central star, the companion candidates would be classified differently. At a distance of 440 pc, HD101412b would not be classified as a planet, as its distance would exceed the limit of 100 AU, but at lower distances it would. If this disk orientation gets confirmed, HD101412c would be identified as a planet.

As for the disk orientation, two completely different estimations for the age of the central star have been assumed. Since every possible companion would have formed either simultaneously or after the formation of the star, I adopted the age given in Folsom et al. (2012). The upper limits using the age of Fairlamb et al. (2015) are given in Section 4.3.1. The masses estimated by the COND models are very promising when looking for orbiting planets, since they lay in the range $7.8 - 73.6 M_J$. Similar masses were estimated using the COND models from single band L' measurements by Reggiani et al. (2014) and Quanz et al. (2013). If the planets are accreting material from their circumplanetary disk, they might appear much more luminous, and hot start models, which do not take into account this process, would overestimate their masses.

Because of the strong possibility that at least one of the two candidates is a true companion of HD101412, I calculated the time interval that one has to wait to re-observe the system and identify a background object due to the different proper motion. According to the GAIA measurements, HD101412 moves in the two directions on the sky plane with the following velocities:

$$\mu_{RA} = 23.58 \pm 0.45 \text{ mas/yr}, \quad \mu_{DEC} = -24.98 \pm 0.42 \text{ mas/yr}.$$

If the two signals are due to background objects, in 1.6 years they should be located in a position relative to the central star shifted by at least 2 pixels. Since the object was observed in March 2017, a future

follow-up observation should be planned around October 2018. Softwares like the one used for Fig. 3 of Quanz et al. (2015) are able to consider the orbital motion of the Earth around the Sun and the proper motion of the star given its position on the sky and should be used to plan more accurately the re-observation of HD101412.

In conclusion, a follow-up observation of the Herbig Ae/Be star HD101412 is suggested as soon as possible after October 2018, in order to probe the companion scenario for HD101412b and HD101412c. If confirmed, HD101412 could be the first ever directly observed forming planetary system and could be used to study multiple planet formation and the interaction between planets and disks. Furthermore, it will allow to investigate if the demonstrated presence of a strong stellar magnetic field favors the formation of planetary mass objects in the circumstellar disk. In order to conduct these studies, more information about the precise orientation and composition of the disk are required, as well as a rigorous and definite distance measurement.

5.1.4 HD179218

Two signals were detected in the neighborhood of HD179218, but only one has been considered to be a true candidate, since HD179218b position and shape were not convincing to claim a detection of a candidate point source (see Section 4.4). HD179218c is spatially separated from the central star, but the source of the signal is very faint, making it difficult to exclude it to be one of the disk residuals contaminating the images (see Fig. 18).

Because of the match between the Hipparcos and the GAIA distances, the characterization of the signal has been easier than for other sources discussed in this thesis, and only the GAIA value was considered as it gives the larger parameter results and it is therefore more conservative. The calculation led to a mass of $\sim 18.3 M_J$ and a physical separation from the star of ~ 85.3 AU (see Tab. 5). Those values would classify HD179218c as a probably forming planet. Indeed, even if the mass of the candidates, according to the COND model, would exceed the limit of $\sim 13 M_J$ given by the deuterium burning limit, an accreting protoplanet could have had a considerably lower mass and could have produced the same amount of radiation. Therefore, if the point source were confirmed to be gravitationally bound to HD179218, it would have all the requirements to be classified as a planet.

The proper motion of HD179218 with respect to the fixed background is given by

$$\mu_{RA} = 25.47 \pm 0.05 \text{ mas/yr}, \quad \mu_{DEC} = -30.47 \pm 0.04 \text{ mas/yr}.$$

Since the star is moving fast on the sky plane, in 1.4 yr it is expected to have moved by a distance larger than 2 pixels in the image in the direction of the signal. Therefore it will be possible to investigate the relative position of star and candidate companion, if still visible, after October 2017 (the ISPY observation was carried out in May 2016). Given the period from Tab. 5, in this short time window it is unlikely to observe a large orbital motion. If the point source will still be at the same separation and at the same position angle as recovered from the 2016 data, the common proper motion with HD179218 would be confirmed. A non detection observation may imply that the signal detected in our data is an instrumental artifact. Alternatively, it could be a background object, which may be hidden behind the central star at the time of the follow-up.

In summary, the quick motion of HD179218 allows a re-observation very soon to lead to a definitive statement regarding the possibility of HD179218c to be an orbiting companion of HD179218. In this case, it will most likely be classified as a planet.

5.1.5 TW Hydrae, HD97048 and HD141569

In the surroundings of TW Hydrae, HD97048, and HD141569, no candidate has been found.

In the case of TW Hya, despite many important disk substructures have been detected, no candidate was revealed by the VLT/NACO data in the L' band. The presence of non accreting planets heavier than $\sim 8 M_J$ in the gap at 22 AU may be excluded, while at the distances of the other gaps, at 37 AU and 43 AU, the data reject the possibility that planets of mass $\sim 4 M_J$ are orbiting the central star. This puts important constraints on the possibility that TW Hya hosts giant forming planets in its disk, expected to be accreting and therefore bright enough to be detected by the pipeline.

In the HD97048 neighborhood, the non detection in the L' band of this work is consistent with the small planetary masses hypothesized by Ginski et al. (2016) ($0.3 - 2.6 M_{\oplus}$ at $0.25''$ and $0.1 - 0.7 M_J$ at $0.7''$)

from the dimension of the gaps observed in the disk. The scenario, in which the multitude of gaps and rings observed in the disk are due to the interaction between disk and planets, will be confirmed or discredited once the next generation of surveys will be able to reach the contrast needed to detect much smaller and fainter planets.

The detection limits of HD141569 calculated during this Master Thesis were compared to the ones obtained by Currie et al. (2016) and by Mawet et al. (2017). At an angular separation of $0.4''$ and $0.8''$, planets with masses of $\sim 12.2 M_J$ and $\sim 6.5 M_J$ respectively should be detected according to the contrast shown in Fig. 23, while, at the same distance, Mawet et al. (2017) was able to see $\sim 15 M_J$ and $6 M_J$ respectively, and Currie et al. (2016) $8 M_J$ and $2 M_J$. For every calculation, the age of 5 Myr has been assumed. The obtained results are comparable to the ones obtained by Mawet et al. (2017), even if at small separations it seems that fainter planets may be observed from the ISPY data. On the contrary, the pipeline used by Currie et al. (2016) seems to be more efficient in detecting fainter objects. It has to be kept in mind that, depending on the metric one decides to use to define the detection of a signal, the reached limits could be very different.

To conclude, no signal was detected around HD141569, not even at the position in which Mawet et al. (2017) suggested the possibility of a faint source. The detection limits were comparable to the ones already presented in the literature.

5.2 Comparison between protoplanetary candidates

I compared the properties of the found protoplanet candidates with the ones presented in Kraus and Ireland (2012), Reggiani et al. (2014), Quanz et al. (2015). As already pointed out multiple times, the distance uncertainty made difficult to exactly characterize the planets and large uncertainty needed to be considered. Fig. 25 compares the separation and the absolute magnitude of the candidates. The blue circles represent the existing protoplanet candidates orbiting LkCa15 (Kraus and Ireland, 2012), HD100546 (Quanz et al., 2013, 2015) and HD169142 (Reggiani et al., 2014; Biller et al., 2014). The filled colored areas represent the possible position in the separation-brightness diagram for every candidate presented in Section 4. The limits of the surfaces covered by each candidate are given by the values obtained each time with the Hipparcos and the GAIA data. HD179218c is located in a very definite region of the plot, because the difference between Hipparcos and GAIA results were small. On the contrary, the possible distances of HD259431 differ by a factor ~ 3 between the measurements, influencing the absolute magnitude and the physical separation.

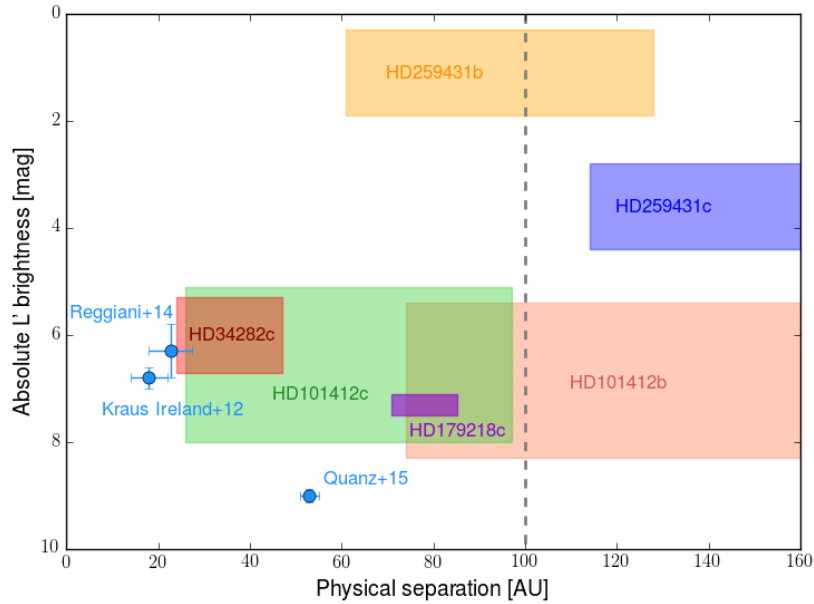


Figure 25: Separation against brightness of the known protoplanets from Kraus and Ireland (2012), Reggiani et al. (2014) and Quanz et al. (2015), represented with blue circles, and of the candidates presented in this work.

HD101412b and HD101412c have been plotted assuming the disk to be oriented as presented in van der Plas et al. (2008). HD259431c separation is shown with respect to the central star, even if other possible scenarios were given in section 5.1.1. The grey line displays the separation of 100 AU, used to distinguish planets from planetary mass companions on a wide orbit.

There is strong evidence that three objects found in this work are planets, while two other objects show debated separations and require a further investigation of the host star properties. If confirmed, this Master Thesis might have doubled the number of known protoplanets, bringing the sample to be composed by 6 elements.

In particular, HD34282b lays in a very promising position and its separation and brightness are very comparable to the ones previously found. The observation of disk density gaps further supports the possibility that the circumstellar environment of HD34282 is hosting a young forming planet.

5.3 Mass estimation from evolutionary models

The analysis on the seven datasets of the young objects from the NACO-ISPYPY survey revealed the presence of 6 point sources within the closest $0.563''$ from the central star. The data allowed the direct quantification of the contrast magnitude in the L' band, of the projected angular distance, and of the position angle. To further characterize the signals, more information not directly accessible from the data are required. In particular the L' brightness of the central star is needed in order to estimate the candidate apparent magnitude. Furthermore, the stellar distance is required to calculate its absolute brightness and to make useful photometric comparisons among the objects identified in this work and those previously discovered.

The photometric information allow, thanks to evolutionary models like COND and DUSTY, to infer the mass of the object, assuming a hot start and assuming that the whole radiation spectrum is due to thermal emission during the contraction.

Under these assumptions, the presented objects have masses that vary in the range $7.8 - 370 M_J$, excluding the most likely stellar object HD259431b. The extreme width of the range is given by the huge uncertainty between the distance measures. According to the mass values, the objects can be classified at most as brown dwarfs, and not as planets, except for cases in which the star is assumed to be very close to Earth. Brown dwarfs differ by planets by being object heavier than $\sim 13 M_J$, massive enough to reach the temperatures necessary to burn deuterium in their cores.

Kraus and Ireland (2012), Reggiani et al. (2014) and Quanz et al. (2015) obtained similar results for the protoplanet candidates around HD100546, LkCa15, and HD169142, and thanks to multiwavelength observations they argued and concluded that the planet is accreting material from a protoplanetary disk. Different simulations also showed that, after the opening of a gap in the disk, gaseous material from the outer and the inner disk flows into the gap. The combination of this process with the angular momentum conservation and transport creates automatically a circumplanetary disk of material infalling into the planet (Fouchet and Mayer, 2008; Ayliffe and Bate, 2009).

The accretion rate of the planet from its CPD determines its mass at the end of the formation process. Considering the presence of a CPD reduces dramatically the mass of the planet, because most of the light is a consequence of the accretion, and maintains the system consistent with the data. As an example I will show the case of HD34282b and the model presented in Zhu (2015), according to which the SED of the CPD only depends on two parameters: the disk inner radius R_{in} and the product of planetary mass and disk accretion rate $M_p \dot{M}$.

The upper plot of Fig. 26 shows the simulated brightnesses of an accreting circumplanetary disk as a function of the parameter $M_p \dot{M}$ (Zhu, 2015). The colors represent the inner radius of the disk (1, 1.5, 2, 4 R_J). There is a correlation between inner radius and brightness: the smaller the inner radius, the higher the brightness in the L' band. In fact, the innermost material moves faster, is hotter and consequently emits more radiation compared to material at larger radii. Furthermore, increasing the product of planet mass and accretion mass rate, the emission and the disk brightness increase, as more material falls into the object and release gravitational energy. The coral horizontal lines represent the brightnesses of HD34282b, when calculated assuming the Hipparcos ($L'=6.7 \pm 0.6$ mag) and the GAIA measurements ($L'=5.3 \pm 0.3$ mag). The panel shows for every value of $M \dot{M}$ the fraction of the brightness of HD34282 which is due to the disk emission.

The second panel of Fig. 26 shows the remaining brightness of HD34282b, which cannot be explained as accretion emission, as a function of the product of mass and accretion rate. It plots the thermal emission of the shrinking planet at every value of $M \dot{M}$, assuming that the luminosity is due either to the accretion

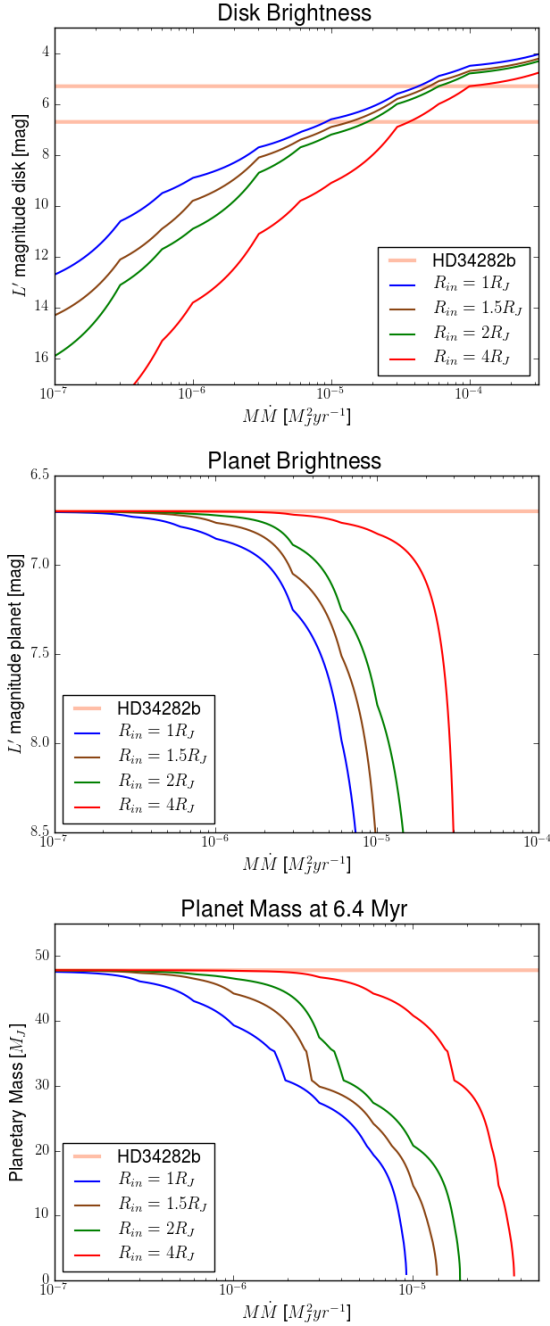


Figure 26: *Top:* brightness due to the accretion process of the disk onto the planet for different inner disk radii. The coral lines represent the retrieved absolute magnitudes using the distance measurements from GAIA and Hipparcos. *Middle:* The remaining light is due to thermal radiation of the planet. Summing the lines shown in the middle and in the upper plot gives the constant magnitude measured from the data (in this case only the Hipparcos value is plotted). *Bottom:* a mass value according to the COND models has been assigned to the thermal energy released from the central plot. The coral line shows the value expected if all the luminosity comes from the contraction of the object.

or to the thermal emission of the planet contraction. If the accretion rate is very low ($\sim 10^{-7} - 10^{-6} M_J^2 \text{ yr}^{-1}$), most of the light is due to the thermal emission, while at higher $\dot{M}M$ ($\sim 10^{-5} M_J^2 \text{ yr}^{-1}$), an important fraction is due to the circumplanetary disk. For this plot the Hipparcos distance has been assumed. The bottom plot of Fig. 26 shows the COND masses calculated from the thermal radiation from the central plot. As pointed out in Section 4.2.1, when a zero contribution from an accreting disk is assumed, the object is expected to have a mass of $\sim 48 M_J$, while taking into account the disk contribution considerably decreases the mass of the planet. Depending on the inner radius of the accretion disk and on the $\dot{M}M$ parameter, very different mass values are obtained. In particular, masses below the limit of $13 M_J$ can be achieved considering the formation of the circumplanetary disk.

According to Zhu (2015), a $1 M_J$ planet accreting at a rate of $\sim 6 \times 10^{-5} M_J/\text{yr}$ is expected to be as bright as a late M-type brown dwarf. This should have, without considering any contribution from the central protoplanet, a L' brightness of 5.2 mag ($R_{in} = R_J$), comparable to the brighter case of HD34282b. Much lower accretion rates are required to explain the values obtained for nearer stars.

It should be emphasized that according to the model from Zhu (2015), a very high accretion rate ($\sim 10^{-5} - 10^{-6} M_\odot/\text{yr}$) onto a $1 M_J$ planet is able to explain the extremely high luminosity of HD259431b. Similarly, every other magnitude values of companion candidates presented in Section 4 can be explained with CPDs accreting at different rates onto the planet. For this reason, in addition to the common proper motion confirmation, the confirmation of a SED shape consistent with a CPD is required to support this scenario. Multiwavelength observations, especially at longer wavelengths, should be able to construct SEDs of CPDs and to constrain the many free parameters.

6 Conclusions

I have presented the results of the analysis of seven young stars (six Herbig Ae/Be stars and one TTauri star), showing the presence of six possible companions. One of the most interesting consequences of this work regards the statistical properties of the planetary demography: according to many studies (e.g. Brandt et al., 2014) the occurrence rate of giant planets is very low. For example, the frequency of gas giant planets ($5 - 13 M_J$) orbiting BA stars at orbital separation in the range 30-300 AU, according to Bowler (2016), is $2.8^{+3.7}_{-2.3}\%$. This occurrence rate is in disagreement with the results presented in this thesis, since among six type B and type A stars, a total of six companion candidates have been identified. One is most likely to be a stellar companion or a brown dwarf, because of its high intensity, while the others have possible planetary masses, considering the accretion from CPDs. The results can be interpreted so that: (1) most of the presented candidates are stellar background objects or instrumental artifacts; (2) the current statistical estimation underestimates the true frequency of gas giant planets; (3) since the detected objects are orbiting young stars, a migration mechanism may drastically change the planet orbit at later ages, bringing it to smaller separations and therefore not to be detected. This last scenario would explain both the occurrence rates found in the literature and the results of this thesis.

If the reported signals have common proper motion with the central star, the presence of a young protoplanet accreting from a circumplanetary disk seems to be the best way to explain the available data, especially the large amount of IR radiation. This implies that the sample of forming planets gets at least doubled, giving to the community many new laboratories to study the interaction between planets and disks, the influence of magnetic fields, the multiplicity and the interaction of forming planets, and the formation mechanism itself. In particular, the availability of multi-band data of a large sample of planets will help to empirically calibrate the current models for improving simulations and theories.

To further investigate the known planet population and its distribution, more precise information on disk orientations and compositions, as well as more reliable data to estimate the stellar properties and in particular distances, are required. The first might be obtained thanks to observations at long wavelengths (e.g. with ALMA), while the second will hopefully be clarified by future GAIA data releases. Furthermore, deeper and larger surveys, multiwavelength observations, and continually improving technologies, will give in the next years a much more exhaustive picture of the giant planet population and the formation process of gaseous planets. The next generation of telescopes will allow the investigation of smaller planetary mass ranges at much smaller separations from the star, bringing new insights in the planet formation and evolution.

7 Acknowledgments

I want to thank my supervisor Sascha Quanz for his availability and his answers to my infinite questions. Many thanks to my “colleagues” of the J floor for the funny moments and sometimes for the serious ones. Thanks to Lia and Matteo for the corrections and the hints during the final phase of this thesis. A huge thanks to my family, especially my mom, for all her encouragement and trust, not only in the past few months, but all over the last 5 years, and even before. Finally, all of my thanks to Sara for her patience over the period of this thesis, her valuable comments and her support.

References

- Alecian, E., Wade, G. A., Catala, C., Grunhut, J. H., Landstreet, J. D., Bagnulo, S., Böhm, T., Folsom, C. P., Marsden, S., and Waite, I. (2013). A high-resolution spectropolarimetric survey of Herbig Ae/Be stars - I. Observations and measurements. *Monthly Notice of the Royal Astronomical Society*, 429:1001–1026.
- Alonso-Albi, T., Fuente, A., Bachiller, R., Neri, R., Planesas, P., Testi, L., Berné, O., and Joblin, C. (2009). Circumstellar disks around Herbig Be stars. *A&A*, 497:117–136.
- Amara, A. and Quanz, S. P. (2012). PYNPOINT: an image processing package for finding exoplanets. *Monthly Notice of the Royal Astronomical Society*, 427:948–955.
- Amara, A., Quanz, S. P., and Akeret, J. (2015). PynPoint code for exoplanet imaging. *Astronomy and Computing*, 10:107–115.
- Andrews, S. M., Wilner, D. J., Zhu, Z., Birnstiel, T., Carpenter, J. M., Pérez, L. M., Bai, X.-N., Öberg, K. I., Hughes, A. M., Isella, A., and Ricci, L. (2016). Ringed Substructure and a Gap at 1 au in the Nearest Protoplanetary Disk. *The Astrophysical Journal Letters*, 820:L40.
- Arenou, F., Luri, X., Babusiaux, C., Fabricius, C., Helmi, A., Robin, A. C., Vallenari, A., Blanco-Cuaresma, S., Cantat-Gaudin, T., Findeisen, K., Reylé, C., Ruiz-Dern, L., Sordo, R., Turon, C., Walton, N. A., Shih, I.-C., Antiche, E., Barache, C., Barros, M., Breddels, M., Carrasco, J. M., Costigan, G., Diakité, S., Eyer, L., Figueras, F., Galluccio, L., Heu, J., Jordi, C., Krone-Martins, A., Lallement, R., Lambert, S., Leclerc, N., Marrese, P. M., Moitinho, A., Mor, R., Romero-Gómez, M., Sartoretti, P., Soria, S., Soubiran, C., Souchay, J., Veljanoski, J., Ziaepour, H., Giuffrida, G., Pancino, E., and Bragaglia, A. (2017). Gaia Data Release 1. Catalogue validation. *A&A*, 599:A50.
- Ayliffe, B. A. and Bate, M. R. (2009). Circumplanetary disc properties obtained from radiation hydrodynamical simulations of gas accretion by protoplanets. *Monthly Notice of the Royal Astronomical Society*, 397:657–665.
- Bally, J., Testi, L., Sargent, A., and Carlstrom, J. (1998). Disk Mass Limits and Lifetimes of Externally Irradiated Young Stellar Objects Embedded in the Orion Nebula. *The Astronomical Journal*, 116:854–859.
- Baraffe, I., Chabrier, G., Barman, T. S., Allard, F., and Hauschildt, P. H. (2003). Evolutionary models for cool brown dwarfs and extrasolar giant planets. The case of HD 209458. *A&A*, 402:701–712.
- Barrado Y Navascués, D. (2006). On the age of the TW Hydrae association and 2M1207334-393254. *A&A*, 459:511–518.
- Bergin, E. A., Cleves, L. I., Gorti, U., Zhang, K., Blake, G. A., Green, J. D., Andrews, S. M., Evans, II, N. J., Henning, T., Öberg, K., Pontoppidan, K., Qi, C., Salyk, C., and van Dishoeck, E. F. (2013). An old disk still capable of forming a planetary system. *Nature*, 493:644–646.
- Biller, B. A., Males, J., Rodigas, T., Morzinski, K., Close, L. M., Juhász, A., Follette, K. B., Lacour, S., Benisty, M., Sicilia-Aguilar, A., Hinz, P. M., Weinberger, A., Henning, T., Pott, J.-U., Bonnefoy, M., and Köhler, R. (2014). An Enigmatic Point-like Feature within the HD 169142 Transitional Disk. *The Astrophysical Journal Letters*, 792:L22.
- Boss, A. P. (1997). Giant planet formation by gravitational instability. *Science*, 276:1836–1839.
- Bouret, J.-C., Martin, C., Deleuil, M., Simon, T., and Catala, C. (2003). Far UV spectroscopy of the circumstellar environment of the Herbig Be stars HD 259431 and HD 250550. *A&A*, 410:175–188.
- Bowler, B. P. (2016). Imaging Extrasolar Giant Planets. *Publications of the Astronomical Society of the Pacific*, 128(10):102001.
- Brandt, T. D., McElwain, M. W., Turner, E. L., Mede, K., Spiegel, D. S., Kuzuhara, M., Schlieder, J. E., Wisniewski, J. P., Abe, L., Biller, B., Brandner, W., Carson, J., Currie, T., Egner, S., Feldt, M., Golota, T., Goto, M., Grady, C. A., Guyon, O., Hashimoto, J., Hayano, Y., Hayashi, M., Hayashi, S., Henning, T., Hodapp, K. W., Inutsuka, S., Ishii, M., Iye, M., Janson, M., Kandori, R., Knapp, G. R., Kudo, T., Kusakabe, N., Kwon, J., Matsuo, T., Miyama, S., Morino, J.-I., Moro-Martín,

- A., Nishimura, T., Pyo, T.-S., Serabyn, E., Suto, H., Suzuki, R., Takami, M., Takato, N., Terada, H., Thalmann, C., Tomono, D., Watanabe, M., Yamada, T., Takami, H., Usuda, T., and Tamura, M. (2014). A Statistical Analysis of SEEDS and Other High-contrast Exoplanet Surveys: Massive Planets or Low-mass Brown Dwarfs? *ApJ*, 794:159.
- Briceño, C., Vivas, A. K., Calvet, N., Hartmann, L., Pacheco, R., Herrera, D., Romero, L., Berlind, P., Sánchez, G., Snyder, J. A., and Andrews, P. (2001). The CIDA-QUEST Large-Scale Survey of Orion OB1: Evidence for Rapid Disk Dissipation in a Dispersed Stellar Population. *Science*, 291:93–97.
- Burrows, A., Hubeny, I., Budaj, J., and Hubbard, W. B. (2007). Possible Solutions to the Radius Anomalies of Transiting Giant Planets. *ApJ*, 661:502–514.
- Chauvin, G., Lagrange, A.-M., Dumas, C., Zuckerman, B., Mouillet, D., Song, I., Beuzit, J.-L., and Lowrance, P. (2004). A giant planet candidate near a young brown dwarf. Direct VLT/NACO observations using IR wavefront sensing. *A&A*, 425:L29–L32.
- Currie, T., Grady, C. A., Cloutier, R., Konishi, M., Stassun, K., Debes, J., van der Marel, N., Muto, T., Jayawardhana, R., and Ratzka, T. (2016). The Matryoshka Disk: Keck/NIRC2 Discovery of a Solar-system-scale, Radially Segregated Residual Protoplanetary Disk around HD 141569A. *The Astrophysical Journal Letters*, 819:L26.
- D’Alessio, P., Calvet, N., and Hartmann, L. (2001). Accretion Disks around Young Objects. III. Grain Growth. *ApJ*, 553:321–334.
- Dent, W. R. F., Greaves, J. S., and Coulson, I. M. (2005). CO emission from discs around isolated HAeBe and Vega-excess stars. *Monthly Notice of the Royal Astronomical Society*, 359:663–676.
- Doering, R. L., Meixner, M., Holfeltz, S. T., Krist, J. E., Ardila, D. R., Kamp, I., Clampin, M. C., and Lubow, S. H. (2007). HD 97048’s Circumstellar Environment as Revealed by a Hubble Space Telescope ACS Coronagraphic Study of Disk Candidate Stars. *The Astronomical Journal*, 133:2122–2131.
- Españolat, C., Calvet, N., D’Alessio, P., Hernández, J., Qi, C., Hartmann, L., Furlan, E., and Watson, D. M. (2007). On the Diversity of the Taurus Transitional Disks: UX Tauri A and LkCa 15. *ApJL*, 670:L135–L138.
- Fairlamb, J. R., Oudmaijer, R. D., Mendigutía, I., Ilee, J. D., and van den Ancker, M. E. (2015). A spectroscopic survey of Herbig Ae/Be stars with X-shooter - I. Stellar parameters and accretion rates. *Monthly Notice of the Royal Astronomical Society*, 453:976–1001.
- Fedele, D., van den Ancker, M. E., Acke, B., van der Plas, G., van Boekel, R., Wittkowski, M., Henning, T., Bouwman, J., Meeus, G., and Rafanelli, P. (2008). The structure of the protoplanetary disk surrounding three young intermediate mass stars. II. Spatially resolved dust and gas distribution. *A&A*, 491:809–820.
- Folsom, C. P., Bagnulo, S., Wade, G. A., Alecian, E., Landstreet, J. D., Marsden, S. C., and Waite, I. A. (2012). Chemical abundances of magnetic and non-magnetic Herbig Ae/Be stars. *Monthly Notice of the Royal Astronomical Society*, 422:2072–2101.
- Fouchet, L., Gonzalez, J.-F., and Maddison, S. T. (2010). Planet gaps in the dust layer of 3D protoplanetary disks. I. Hydrodynamical simulations of T Tauri disks. *A&A*, 518:A16.
- Fouchet, L. and Mayer, L. (2008). Migration and growth of giant planets in self-gravitating disks with varied thermodynamics. *ArXiv e-prints*.
- Ginski, C., Stolker, T., Pinilla, P., Dominik, C., Boccaletti, A., de Boer, J., Benisty, M., Biller, B., Feldt, M., Garufi, A., Keller, C. U., Kenworthy, M., Maire, A. L., Ménard, F., Mesa, D., Milli, J., Min, M., Pinte, C., Quanz, S. P., van Boekel, R., Bonnefoy, M., Chauvin, G., Desidera, S., Gratton, R., Girard, J. H. V., Keppler, M., Kopytova, T., Lagrange, A.-M., Langlois, M., Rouan, D., and Vigan, A. (2016). Direct detection of scattered light gaps in the transitional disk around HD 97048 with VLT/SPHERE. *A&A*, 595:A112.
- Hubrig, S., Schöller, M., Savanov, I., González, J. F., Cowley, C. R., Schütz, O., Arlt, R., and Rüdiger, G. (2010). The exceptional Herbig Ae star HD 101412: The first detection of resolved magnetically split lines and the presence of chemical spots in a Herbig star. *Astronomische Nachrichten*, 331:361.

- Ilee, J. D., Fairlamb, J., Oudmaijer, R. D., Mendigutía, I., van den Ancker, M. E., Kraus, S., and Wheelwright, H. E. (2014). Investigating the inner discs of Herbig Ae/Be stars with CO bandhead and Br γ emission. *Monthly Notice of the Royal Astronomical Society*, 445:3723–3736.
- Juhász, A., Bouwman, J., Henning, T., Acke, B., van den Ancker, M. E., Meeus, G., Dominik, C., Min, M., Tielens, A. G. G. M., and Waters, L. B. F. M. (2010). Dust Evolution in Protoplanetary Disks Around Herbig Ae/Be Stars—the Spitzer View. *ApJ*, 721:431–455.
- Kanagawa, K. D., Muto, T., Tanaka, H., Tanigawa, T., Takeuchi, T., Tsukagoshi, T., and Momose, M. (2016). Mass constraint for a planet in a protoplanetary disk from the gap width. *PASJ*, 68:43.
- Khalafinejad, S., Maaskant, K. M., Mariñas, N., and Tielens, A. G. G. M. (2016). Large dust gaps in the transitional disks of HD 100453 and HD 34282. Connecting the gap size to the spectral energy distribution and mid-infrared imaging. *A&A*, 587:A62.
- Kharchenko, N. V., Piskunov, A. E., Röser, S., Schilbach, E., and Scholz, R.-D. (2005). Astrophysical parameters of Galactic open clusters. *A&A*, 438:1163–1173.
- Kraus, A. L. and Ireland, M. J. (2012). LkCa 15: A Young Exoplanet Caught at Formation? *The Astrophysical Journal*, 745:5.
- Kraus, S., Preibisch, T., and Ohnaka, K. (2008a). Detection of an Inner Gaseous Component in a Herbig Be Star Accretion Disk: Near- and Mid-Infrared Spectrointerferometry and Radiative Transfer modeling of MWC 147. *ApJ*, 676:490–508.
- Kraus, S., Preibisch, T., and Ohnaka, K. (2008b). Detection of an Inner Gaseous Component in a Herbig Be Star Accretion Disk: Near- and Mid-Infrared Spectrointerferometry and Radiative Transfer modeling of MWC 147. *ApJ*, 676:490–508.
- Lafrenière, D., Jayawardhana, R., and van Kerkwijk, M. H. (2008). Direct Imaging and Spectroscopy of a Planetary-Mass Candidate Companion to a Young Solar Analog. *ApJL*, 689:L153.
- Lagage, P.-O., Doucet, C., Pantin, E., Habart, E., Duchêne, G., Ménard, F., Pinte, C., Charnoz, S., and Pel, J.-W. (2006). Anatomy of a Flaring Proto-Planetary Disk Around a Young Intermediate-Mass Star. *Science*, 314:621–623.
- Lindgren, L., Lammers, U., Bastian, U., Hernández, J., Klioner, S., Hobbs, D., Bombrun, A., Michalik, D., Ramos-Lerate, M., Butkevich, A., Comoretto, G., Joliet, E., Holl, B., Hutton, A., Parsons, P., Steidelmüller, H., Abbas, U., Altmann, M., Andrei, A., Anton, S., Bach, N., Barache, C., Becciani, U., Berthier, J., Bianchi, L., Biermann, M., Bouquillon, S., Bourda, G., Brüsemeister, T., Bucciarelli, B., Busonero, D., Carlucci, T., Castañeda, J., Charlot, P., Clotet, M., Crosta, M., Davidson, M., de Felice, F., Drimmel, R., Fabricius, C., Fienga, A., Figueras, F., Fraile, E., Gai, M., Garralda, N., Geyer, R., González-Vidal, J. J., Guerra, R., Hambly, N. C., Hauser, M., Jordan, S., Lattanzi, M. G., Lenhardt, H., Liao, S., Löffler, W., McMillan, P. J., Mignard, F., Mora, A., Morbidelli, R., Portell, J., Riva, A., Sarasso, M., Serraller, I., Siddiqui, H., Smart, R., Spagna, A., Stampa, U., Steele, I., Taris, F., Torra, J., van Reeve, W., Vecchiato, A., Zschocke, S., de Bruijne, J., Gracia, G., Raison, F., Lister, T., Marchant, J., Messineo, R., Soffel, M., Osorio, J., de Torres, A., and O’Mullane, W. (2016). Gaia Data Release 1. Astrometry: one billion positions, two million proper motions and parallaxes. *A&A*, 595:A4.
- Maaskant, K. M., de Vries, B. L., Min, M., Waters, L. B. F. M., Dominik, C., Molster, F., and Tielens, A. G. G. M. (2015). Location and sizes of forsterite grains in protoplanetary disks. Interpretation from the Herschel DIGIT programme. *A&A*, 574:A140.
- Maaskant, K. M., Honda, M., Waters, L. B. F. M., Tielens, A. G. G. M., Dominik, C., Min, M., Verhoeff, A., Meeus, G., and van den Ancker, M. E. (2013). Identifying gaps in flaring Herbig Ae/Be disks using spatially resolved mid-infrared imaging. Are all group I disks transitional? *A&A*, 555:A64.
- Marley, M. S., Fortney, J. J., Hubickyj, O., Bodenheimer, P., and Lissauer, J. J. (2007). On the Luminosity of Young Jupiters. *ApJ*, 655:541–549.
- Marois, C., Lafrenière, D., Doyon, R., Macintosh, B., and Nadeau, D. (2006). Angular Differential Imaging: A Powerful High-Contrast Imaging Technique. *ApJ*, 641:556–564.

- Marois, C., Macintosh, B., Barman, T., Zuckerman, B., Song, I., Patience, J., Lafrenière, D., and Doyon, R. (2008). Direct Imaging of Multiple Planets Orbiting the Star HR 8799. *Science*, 322:1348.
- Mawet, D., Absil, O., Delacroix, C., Girard, J. H., Milli, J., O’Neal, J., Baudoz, P., Boccaletti, A., Bourget, P., Christiaens, V., Forsberg, P., Gonté, F., Habraken, S., Hanot, C., Karlsson, M., Kasper, M., Lizon, J.-L., Muzic, K., Olivier, R., Peña, E., Slusarenko, N., Tacconi-Garman, L. E., and Surdej, J. (2013). L-band AGPM vector vortex coronagraph’s first light on VLT/NACO. Discovery of a late-type companion at two beamwidths from an F0V star. *A&A*, 552:L13.
- Mawet, D., Choquet, É., Absil, O., Huby, E., Bottom, M., Serabyn, E., Femenia, B., Lebreton, J., Matthews, K., Gomez Gonzalez, C. A., Wertz, O., Carlomagno, B., Christiaens, V., Defrère, D., Delacroix, C., Forsberg, P., Habraken, S., Jolivet, A., Karlsson, M., Milli, J., Pinte, C., Piron, P., Reggiani, M., Surdej, J., and Vargas Catalan, E. (2017). Characterization of the Inner Disk around HD 141569 A from Keck/NIRC2 L-Band Vortex Coronagraphy. *The Astronomical Journal*, 153:44.
- Mawet, D., Milli, J., Wahhaj, Z., Pelat, D., Absil, O., Delacroix, C., Boccaletti, A., Kasper, M., Kenworthy, M., Marois, C., Mennesson, B., and Pueyo, L. (2014). Fundamental Limitations of High Contrast Imaging Set by Small Sample Statistics. *ApJ*, 792:97.
- Mayor, M. and Queloz, D. (1995). A Jupiter-mass companion to a solar-type star. *Nature*, 378:355–359.
- Mazoyer, J., Boccaletti, A., Choquet, É., Perrin, M. D., Pueyo, L., Augereau, J.-C., Lagrange, A.-M., Debes, J., and Wolff, S. G. (2016). A Symmetric Inner Cavity in the HD 141569A Circumstellar Disk. *ApJ*, 818:150.
- Mendigutía, I., Oudmaijer, R. D., Mourard, D., and Muzerolle, J. (2017). The compact H α emitting regions of the Herbig Ae/Be stars HD 179218 and HD 141569 from CHARA spectro-interferometry. *Monthly Notice of the Royal Astronomical Society*, 464:1984–1989.
- Menu, J., van Boekel, R., Henning, T., Leinert, C., Waelkens, C., and Waters, L. B. F. M. (2015). The structure of disks around intermediate-mass young stars from mid-infrared interferometry. Evidence for a population of group II disks with gaps. *A&A*, 581:A107.
- Merín, B., Montesinos, B., Eiroa, C., Solano, E., Mora, A., D’Alessio, P., Calvet, N., Oudmaijer, R. D., de Winter, D., Davies, J. K., Harris, A. W., Collier Cameron, A., Deeg, H. J., Ferlet, R., Garzón, F., Grady, C. A., Horne, K., Miranda, L. F., Palacios, J., Penny, A., Quirrenbach, A., Rauer, H., Schneider, J., and Wesselius, P. R. (2004). Study of the properties and spectral energy distributions of the Herbig AeBe stars HD 34282 and HD 141569. *A&A*, 419:301–318.
- Mora, A., Merín, B., Solano, E., Montesinos, B., de Winter, D., Eiroa, C., Ferlet, R., Grady, C. A., Davies, J. K., Miranda, L. F., Oudmaijer, R. D., Palacios, J., Quirrenbach, A., Harris, A. W., Rauer, H., Collier Cameron, A., Deeg, H. J., Garzón, F., Penny, A., Schneider, J., Tsapras, Y., and Wesselius, P. R. (2001). EXPORT: Spectral classification and projected rotational velocities of Vega-type and pre-main sequence stars. *A&A*, 378:116–131.
- Palla, F. and Stahler, S. W. (1993). The Pre-Main-Sequence Evolution of Intermediate-Mass Stars. *The Astrophysical Journal*, 418:414.
- Piétu, V., Dutrey, A., and Kahane, C. (2003). A Keplerian disk around the Herbig Ae star HD 34282. *A&A*, 398:565–569.
- Pollack, J. B., Hubickyj, O., Bodenheimer, P., Lissauer, J. J., Podolak, M., and Greenzweig, Y. (1996). Formation of the Giant Planets by Concurrent Accretion of Solids and Gas. *Icarus*, 124:62–85.
- Qi, C., Ho, P. T. P., Wilner, D. J., Takakuwa, S., Hirano, N., Ohashi, N., Bourke, T. L., Zhang, Q., Blake, G. A., Hogerheijde, M., Saito, M., Choi, M., and Yang, J. (2004). Imaging the Disk around TW Hydrae with the Submillimeter Array. *ApJ*, 616:L11–L14.
- Qi, C., Öberg, K. I., Wilner, D. J., D’Alessio, P., Bergin, E., Andrews, S. M., Blake, G. A., Hogerheijde, M. R., and van Dishoeck, E. F. (2013). Imaging of the CO Snow Line in a Solar Nebula Analog. *Science*, 341:630–632.

- Quanz, S. P., Amara, A., Meyer, M. R., Girard, J. H., Kenworthy, M. A., and Kasper, M. (2015). Confirmation and Characterization of the Protoplanet HD 100546 b—Direct Evidence for Gas Giant Planet Formation at 50 AU. *ApJ*, 807:64.
- Quanz, S. P., Amara, A., Meyer, M. R., Kenworthy, M. A., Kasper, M., and Girard, J. H. (2013). A Young Protoplanet Candidate Embedded in the Circumstellar Disk of HD 100546. *The Astrophysical Journal Letters*, 766:L1.
- Quanz, S. P., Birkmann, S. M., Apai, D., Wolf, S., and Henning, T. (2012). Resolving the inner regions of the HD 97048 circumstellar disk with VLT/NACO polarimetric differential imaging. *A&A*, 538:A92.
- Reggiani, M., Quanz, S. P., Meyer, M. R., Pueyo, L., Absil, O., Amara, A., Anglada, G., Avenhaus, H., Girard, J. H., Carrasco Gonzalez, C., Graham, J., Mawet, D., Meru, F., Milli, J., Osorio, M., Wolff, S., and Torrelles, J.-M. (2014). Discovery of a Companion Candidate in the HD 169142 Transition Disk and the Possibility of Multiple Planet Formation. *The Astrophysical Journal Letters*, 792:L23.
- Sallum, S., Follette, K. B., Eisner, J. A., Close, L. M., Hinz, P., Kratter, K., Males, J., Skemer, A., Macintosh, B., Tuthill, P., Bailey, V., Defrère, D., Morzinski, K., Rodigas, T., Spalding, E., Vaz, A., and Weinberger, A. J. (2015). Accreting protoplanets in the LkCa 15 transition disk. *Nature*, 527:342–344.
- Seok, J. Y. and Li, A. (2017). Polycyclic Aromatic Hydrocarbons in Protoplanetary Disks around Herbig Ae/Be and T Tauri Stars. *ApJ*, 835:291.
- Shlens, J. (2014). A Tutorial on Principal Component Analysis. *ArXiv e-prints*.
- Spiegel, D. S. and Burrows, A. (2012). Spectral and Photometric Diagnostics of Giant Planet Formation Scenarios. *ApJ*, 745:174.
- Thomas, S. J., van der Blik, N. S., Rodgers, B., Doppmann, G., and Bouvier, J. (2007). Multiplicity of Herbig Ae/Be Stars. In Hartkopf, W. I., Harmanec, P., and Guinan, E. F., editors, *Tests in Contemporary Astrophysics*, volume 240 of *IAU Symposium*, pages 250–253.
- Uyama, T., Hashimoto, J., Kuzuhara, M., Mayama, S., Akiyama, E., Currie, T., Livingston, J., Kudo, T., Kusakabe, N., Abe, L., Brandner, W., Brandt, T. D., Carson, J. C., Egner, S., Feldt, M., Goto, M., Grady, C. A., Guyon, O., Hayano, Y., Hayashi, M., Hayashi, S. S., Henning, T., Hodapp, K. W., Ishii, M., Iye, M., Janson, M., Kandori, R., Knapp, G. R., Kwon, J., Matsuo, T., Mcelwain, M. W., Miyama, S., Morino, J.-I., Moro-Martin, A., Nishimura, T., Pyo, T.-S., Serabyn, E., Suenaga, T., Suto, H., Suzuki, R., Takahashi, Y. H., Takami, M., Takato, N., Terada, H., Thalmann, C., Turner, E. L., Watanabe, M., Wisniewski, J., Yamada, T., Takami, H., Usuda, T., and Tamura, M. (2017). The SEEDS High-Contrast Imaging Survey of Exoplanets Around Young Stellar Objects. *AJ*, 153:106.
- van Boekel, R., Min, M., Waters, L. B. F. M., de Koter, A., Dominik, C., van den Ancker, M. E., and Bouwman, J. (2005). A 10 μ m spectroscopic survey of Herbig Ae star disks: Grain growth and crystallization. *A&A*, 437:189–208.
- van der Plas, G., van den Ancker, M. E., Fedele, D., Acke, B., Dominik, C., Waters, L. B. F. M., and Bouwman, J. (2008). The structure of protoplanetary disks surrounding three young intermediate mass stars. I. Resolving the disk rotation in the [OI] 6300 Å line. *A&A*, 485:487–495.
- van der Plas, G., van den Ancker, M. E., Waters, L. B. F. M., and Dominik, C. (2015). The structure of disks around Herbig Ae/Be stars as traced by CO ro-vibrational emission. *A&A*, 574:A75.
- van der Plas, G., Wright, C. M., Ménard, F., Casassus, S., Canovas, H., Pinte, C., Maddison, S. T., Maaskant, K., Avenhaus, H., Cieza, L., Perez, S., and Ubach, C. (2017). Cavity and other radial substructures in the disk around HD 97048. *A&A*, 597:A32.
- van Leeuwen, F. (2007). Validation of the new Hipparcos reduction. *A&A*, 474:653–664.
- Walsh, C., Juhász, A., Meeus, G., Dent, W. R. F., Maud, L. T., Aikawa, Y., Millar, T. J., and Nomura, H. (2016). ALMA Reveals the Anatomy of the mm-sized Dust and Molecular Gas in the HD 97048 Disk. *ApJ*, 831:200.

- Weinberger, A. J., Anglada-Escudé, G., and Boss, A. P. (2013). Distance and Kinematics of the TW Hydrae Association from Parallaxes. *ApJ*, 762:118.
- Weinberger, A. J., Rich, R. M., Becklin, E. E., Zuckerman, B., and Matthews, K. (2000). Stellar Companions and the Age of HD 141569 and Its Circumstellar Disk. *The Astrophysical Journal*, 544:937–943.
- Wheelwright, H. E., Vink, J. S., Oudmaijer, R. D., and Drew, J. E. (2011). On the alignment between the circumstellar disks and orbital planes of Herbig Ae/Be binary systems. *A&A*, 532:A28.
- Wright, E. L., Eisenhardt, P. R. M., Mainzer, A. K., Ressler, M. E., Cutri, R. M., Jarrett, T., Kirkpatrick, J. D., Padgett, D., McMillan, R. S., Skrutskie, M., Stanford, S. A., Cohen, M., Walker, R. G., Mather, J. C., Leisawitz, D., Gautier, III, T. N., McLean, I., Benford, D., Lonsdale, C. J., Blain, A., Mendez, B., Irace, W. R., Duval, V., Liu, F., Royer, D., Heinrichsen, I., Howard, J., Shannon, M., Kendall, M., Walsh, A. L., Larsen, M., Cardon, J. G., Schick, S., Schwalm, M., Abid, M., Fabinsky, B., Naes, L., and Tsai, C.-W. (2010). The Wide-field Infrared Survey Explorer (WISE): Mission Description and Initial On-orbit Performance. *The Astronomical Journal*, 140:1868–1881.
- Zhu, Z. (2015). Accreting Circumplanetary Disks: Observational Signatures. *ApJ*, 799:16.



Eidgenössische Technische Hochschule Zürich
Swiss Federal Institute of Technology Zurich

Declaration of originality

The signed declaration of originality is a component of every semester paper, Bachelor's thesis, Master's thesis and any other degree paper undertaken during the course of studies, including the respective electronic versions.

Lecturers may also require a declaration of originality for other written papers compiled for their courses.

I hereby confirm that I am the sole author of the written work here enclosed and that I have compiled it in my own words. Parts excepted are corrections of form and content by the supervisor.

Title of work (in block letters):

VLN/NACO Direct Detection and Characterization of Six Companion Candidates in the Circumstellar Disks of Young Stars

Authored by (in block letters):

For papers written by groups the names of all authors are required.

Name(s):

Cugno

First name(s):

Gabriele

With my signature I confirm that

- I have committed none of the forms of plagiarism described in the '[Citation etiquette](#)' information sheet.
- I have documented all methods, data and processes truthfully.
- I have not manipulated any data.
- I have mentioned all persons who were significant facilitators of the work.

I am aware that the work may be screened electronically for plagiarism.

Place, date

Zürich, 10.05.2017

Signature(s)

For papers written by groups the names of all authors are required. Their signatures collectively guarantee the entire content of the written paper.